CENTRO INTERNACIONAL DE ESTUDOS
DE DOUTORAMENTO E AVANZADOS
DA USC (CIEDUS)

TESIS DE DOCTORADO

SINGLE-NUCLEON KNOCKOUT AND TOTAL REACTION CROSS SECTIONS IN MEDIUM-MASS NEUTRON-RICH NUCLEI

Javier Díaz Cortés

ESCUELA DE DOCTORADO INTERNACIONAL

PROGRAMA DE DOCTORADO EN FÍSICA NUCLEAR Y DE PARTÍCULAS

SANTIAGO DE COMPOSTELA

2018

DECLARACIÓN DEL AUTOR DE LA TESIS

Single-nucleon knockout and total reaction cross sections in medium-mass neutron-rich nuclei

D./Dña. Javier Díaz Cortés

Presento mi tesis, siguiendo el procedimiento adecuado al Reglamento, y declaro que:

1) *La tesis abarca los resultados de la elaboración de mi trabajo.*
2) *En su caso, en la tesis se hace referencia a las colaboraciones que tuvo este trabajo.*
3) *La tesis es la versión definitiva presentada para su defensa y coincide con la versión enviada en formato electrónico.*
4) *Confirmo que la tesis no incurre en ningún tipo de plagio de otros autores ni de trabajos presentados por mí para la obtención de otros títulos.*

En Santiago de Compostela, 12 de Noviembre de 2018

Fdo

AUTORIZACIÓN DEL DIRECTOR / TUTOR DE LA TESIS

Single-nucleon knockout and total reaction cross sections in medium-mass neutron-rich nuclei

D./Dña. José Fernando Benlliure Anaya

INFORMA/N:

Que la presente tesis, corresponde con el trabajo realizado por D/Dña. ***Javier Díaz Cortés****, bajo mi dirección, y autorizo su presentación, considerando que reúne los requisitos exigidos en el Reglamento de Estudios de Doctorado de la USC, y que como director de ésta no incurre en las causas de abstención establecidas en Ley 40/2015.*

En Santiago de Compostela, 12 de Noviembre de 2018

Fdo

Acknowledgments

Firstly, I would like to express my sincere gratitude to my supervisor, Jose Fernando Benlliure Anaya, who gave me the opportunity to discover the fascinating world of nuclear physics. Without his guidance, motivation and support, this work would have not been possible.

I would also like to thank the rest of my colleagues of the GENP group, with a special mention to Dolores Cortina Gil and Jose Luis Rodríguez Sánchez, without their incomparable help in the daily work this PhD would not be finished.

A mis padres, a los que les debo tanto, este trabajo no habría sido posible sin vosotros. Gracias por todos los años the apoyo incondicional y ayuda, por todo lo que me habéis enseñado. Si hoy estoy aquí escribiendo estas líneas es gracias a vosotros. A mi hermana, que siempre es capaz de sacarme una sonrisa, gracias por todos los inolvidables momentos que hemos pasado. A mi novia, Nelly, por apoyarme día a día a lo largo de todo este tiempo, por tener siempre una sonrisa en los momentos mas difíciles, gracias de corazón.

Finalmente, a mis amigos y compañeros, que comenzamos la carrera de física hace ya 9 años y que hemos recorrido el largo camino para llegar hasta aquí. Todos los momentos que hemos vivido a lo largo de todo este tiempo los llevaré siempre conmigo.

USC
UNIVERSIDADE
DE SANTIAGO
DE COMPOSTELA

Contents

Introduction

The nuclear shell model is based on the idea that nucleons are allowed to move independently in orbitals with certain quantum numbers under the constrains of an average potential generated by the interaction with all the other nucleons. This picture of the nuclei was good enough to explain why some isotopes with particular numbers of neutrons and protons showed stronger binding compared with their neighbours. This "magic" behavior of nuclei is exposed through comparatively large excitation energies of their first excited 2^+ state and high one- and two-nucleon separation energies.

Only a few nuclei with double-magic behavior for both neutrons and protons have been experimentally observed so far. Among them, ^{132}Sn, with 50 protons and 82 neutrons, is the only medium-mass very-neutron-rich double-magic nuclei experimentally produced and studied. Thus, this nuclei and its surrounding neighbours offer unique opportunities for a better understanding of the evolution of nuclear structure far beyond the valley of β stability.

In addition, many of the nuclei in this region are involved in the astrophysical rapid neutron-capture process for stellar nucleosynthesis, responsible for the production of heavy elements in the Universe. The theoretical models used for the understanding of this process use as inputs many nuclear properties such as masses or lifetimes. Despite their interest, many of these nuclei are not yet accessible for experiments and their properties are derived from calculations using as inputs the properties of known neighbouring nuclei.

The possibility to access the region of the chart of nuclides around ^{132}Sn became available with the development of radioactive ion beams. This new technology unblocked the possibility of study the structure of nuclei that lie close to the limits of the nuclear existence. As we move away from the valley of β stability to the neutron drip line, the binding energy of the last added neutrons gradually drops until a certain number where the system becomes unbound. This point where the neutron-to-proton ratio makes the system to immediately decay via neutron-emission offers a wide variety of possibilities to study the characteristics of nuclear matter at the limits of the isospin asymmetry. Here, the large neutron excess and low binding energies can lead

to dramatic changes in the bulk and structural properties of those nuclei.

Indeed, it was discovered that the effect of the low binding energies when approaching the drip lines can make the wave function of one or two neutrons to extend far beyond the standard nuclear size, creating exotic structures such as halo nuclei [1, 2] or neutron skins [3].

Among different strategies, single-nucleon knockout reactions have become a powerful spectroscopic tool to investigate the structure of exotic neutron- and proton-rich nuclei. The combined information obtained from the partial cross sections to the different final states of the knockout fragment and its momentum distribution provides direct information on the nucleon's occupancies of orbitals close to the Fermi level. In addition, the overall shell model structure information and all the underlying mechanisms contributing to the ejection of a nucleon in high-energy collisions can be investigated through inclusive measurements.

However, the results obtained in single-nucleon knockout experiments seem to show an universal trend. The first electron scattering *(e,e' p)* experiments [4] evidenced a reduction of the single-particle occupancies of states close to the Fermi level with respect to the predictions of the independent particle model (IPM). Since then, several experiments measuring single-nucleon knockout cross sections obtained a similar result. The theoretical models including shell-model calculations of the single-particle strength of the different states overpredict the measured values. A strong correlation between the reduction of the single-particle occupancies predicted by the shell model and the neutron-proton asymmetry of the nucleus was suggested in Ref.[5]. However, recent results on single-nucleon knockout [6] and transfer [7, 8, 9] reactions show that the quenching of the single-particle occupancies of states is a universal property of the nucleus.

Recent results on high-energy electron-scattering experiments [10] showed that short-range correlations between nucleons may play an important role in these reactions. Short-range correlated nucleon pairs have a large-relative momentum ($k_{rel} > k_f$) and low center-of-mass momentum ($k_{tot} < k_f$) where k_f is the Fermi momentum of the system. Whenever a high-momentum nucleon is removed in a collision, the correlated nucleon in the pair is automatically removed from the nucleus [11]. This effect would make the survival probability of the nucleon knockout fragment to decrease, having an important impact in the measured cross section. The relative fraction of high-momentum to low-momentum nucleons was investigated in Ref.[12] showing that the probability of finding correlated nucleons is larger for the minority specie (i.e. protons in neutron rich nuclei) of a given nucleus an grows with the neutron excess.

In addition, complementary information can be obtained measuring their

total reaction probability, which become observable with total reaction cross sections measurements. These measurements encompass every interaction between projectile and target, and provide excellent benchmark for the different reaction models. Moreover, they provide an indirect measurement of the size of the nucleus and can be used to investigate bulk properties of nuclei. Exotic structures such as the ones observed for light nuclei could be manifested as changes in the systematic evolution of this observable when approaching the drip lines.

The work presented in this dissertation focuses on the study of nuclei around ^{132}Sn through both reaction mechanisms, single-nucleon knockout and total reaction probability. The experiment was performed with the FRS fragment separator in the GSI facility between November and December 2006. Two different reaction mechanisms, combining the fragmentation of ^{132}Xe and fission of ^{238}U at relativistic energies using inverse kinematics allowed the production and investigation of a wide variety of medium-mass neutron-rich nuclei. A two-step reaction scheme, where the FRS was used as two-independent magnetic spectrometer enabled the study of the interaction of these nuclei with a thick target, measuring total reaction and single-nucleon removal cross sections.

The systematic evolution of both magnitudes was studied from the neutron-defficient to the very neutron-rich side of the chart of nuclides for elements around Z=50 including measurements on isotopes beyond the double magic nuclei ^{132}Sn, a perfect environment to test the evolution of the shell structure beyond the double-shell closure.

Chapter 1 of this dissertation is dedicated to describe the one-nucleon knockout reaction mechanism, the main investigated channel of this work. Starting with a brief description of the different contributions to the reaction's residues, it is followed by an overview of the theoretical model used to study the obtained single-nucleon knockout and total reaction cross sections. Then, a review of the recent experimental and theoretical results and the present limitations of our understanding of this reaction is described with some detail. Finally, the effect of short-range correlations is investigated with the recent experimental results recently published.

Chapter 2 offers a detailed description of the experimental apparatus used to obtain the results of this work. A very brief summary of the main characteristics of the GSI experimental facility and of the FRS fragment separator is presented. Then, the reaction mechanism used to produce long isotopic chains in the intermediate-mass region is described as well as the detection equipment deployed during the experiment. Details on some of the key-aspects of the offline analysis are given to offer a better understanding of the methodology followed in this work.

Chapter 3 focuses on the more than 50 total reaction cross sections measured in this work. It starts with a small introduction to the measurement and some of the experimental highlights related to this topic. Then, a very detailed description of the followed process to obtain these measurements is presented as well as the different associated sources of uncertainty. Finally, the results are presented and are described under the Glauber's theory.

Chapter 4 presents the one-nucleon removal reactions measured in this work. Both reaction channels, proton- and neutron-removal were investigated under the Glauber's theory for a wide variety of isotopes around ^{132}Sn. A detailed description of the measurement and the different corrections applied to the final value is given in the first pages. Then, the results are described with an improved intra-nuclear cascade model coupled to a de-excitation code based on particle-hole excitations. The role of final state interactions, inelastic NN collisions and Coulomb and nuclear excitations is evaluated. Finally, a detailed discussion on the role that short-range correlations play in single-nucleon knockout reactions is presented with the conclusions of this work.

Chapter 1

Reactions with relativistic radioactive ion beams

1.1 Introduction

High-energy heavy-ions collisions studied in inverse kinematics introduced new experimental possibilities for the investigation of the nuclear properties close to the limits of the nuclear existence. The inverse kinematics technique is based on the bombardment of a light target with heavy projectiles. Thanks to their high momentum, all the nuclear fragments that originate from the projectile escape from the target. In addition, as the outgoing fragments are emitted in the forward direction, a small angular detection coverage is sufficient to measure all the reaction fragments. Due to this, the reaction fragments can be identified in-flight in mass and atomic number with a high-resolution magnetic spectrometer.

This dissertation is focused on the study of single-nucleon knockout reactions in this experimental regime. However, we also investigate total reaction cross sections as they provide an excellent benchmark of the reaction models used to describe the nucleus-nucleus interaction. In addition, total reaction cross sections provide a direct measurement of the size of the nucleus and they are a useful tool to study structural changes in exotic nuclei.

This chapter focuses on the description of single nucleon knockout reactions. A brief description of the Glauber's theory provides the general theoretical framework for the description of total reaction and single-nucleon knockout cross sections. Finally, a description of the present achievements and challenges in the investigation of the single-nucleon knockout reactions is given, with a discussion of the role that short-range correlations may play in this reaction mechanism.

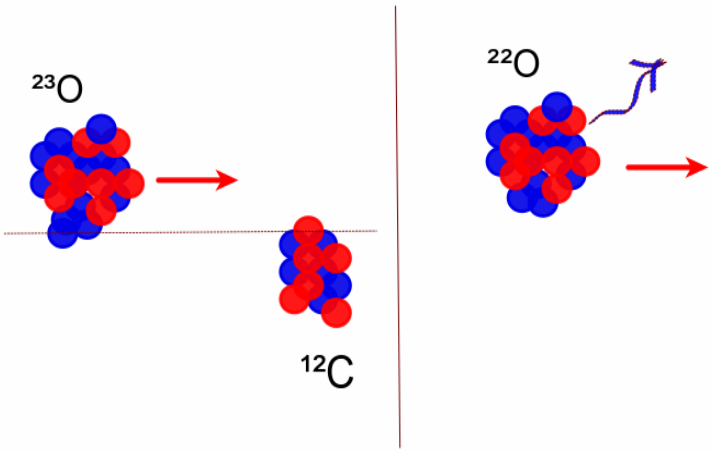

Figure 1.1: *Schematic representation of a one-neutron removal reaction from an unstable ^{23}O projectile by a stable carbon target.*

1.2 Single-nucleon knockout reactions

Heavy-ion collisions resulting in the removal of one of the nucleons from the projectile have been widely used over the years to investigate the structure of the atomic nucleus. Since the first electron (e, e' p) and quasi-free nucleon scattering (p, 2p) experiments performed with stable nuclei [13], the development of radioactive ion beams [14, 15] introduced new experimental possibilities to study the structure of the atomic nucleus far from stability. Among others, single-nucleon knockout reactions have become an extensively used tool to investigate the single-particle structure.

In a nucleon knockout reaction investigated in inverse kinematics a single nucleon is removed from a fast moving projectile in a high-energy collision with a target. Typically, as the collision results to be very peripheral, the nucleon is ejected from the projectile and the A-1 residual fragment continues on his path almost unaffected by the collision. At the same time, the ejected nucleon is scattered to large angles due to the relatively large momentum transfer and thus, it is not always experimentally observed. This can be schematically seen in figure 5.1.

This reaction has been widely used to investigate structural properties of short-lived species over the last decades, being the main observables the cross section and the longitudinal momentum distribution of the reaction residues. Whenever a nucleon is removed from the projectile, a hole is created in the previously occupied orbital and different excited states of the daughter

nucleus are populated depending on the properties of the hole-state. Gamma-ray spectroscopy in coincidence with the A-1 fragment is typically used for tagging the final state of the recoil fragment and the partial cross sections to the different final states can be measured. In addition, inclusive cross section measurements, being the sum over all the exclusive cross sections to the populated bound states of the A-1 nucleus can also be measured and they carry the information of the different underlying mechanisms that contribute to the nucleon-removal channel.

Therefore, inclusive cross sections measurements for the nucleon-removal process provide direct observation of the survival probability of the A-1 heavy residue produced in the reaction. This probability is directly related to the competition between the excitation energy produced due to particle-hole excitations and the particle-emission threshold of the daughter nucleus. However, this simple picture is not complete due to the different mechanisms that can contribute to the one-nucleon removal channel and alter the final value of the measured cross section. Typically, apart from the already described knockout process two different contributions might be of relative importance.

- **Initial state interactions (collective excitations)**

  The excitation of collective nuclear modes [16] may also contribute to the one-nucleon removal cross sections. Electromagnetic excitations such as the giant dipole resonance (GDR), defined as a collective vibration of neutrons against protons, are commonly found over the particle-emission threshold. Therefore, the excitation of the GDR may lead to the emission of a neutron, contributing to the one-neutron removal cross section. However, it is known that for light-Z targets the reaction is dominated by the nuclear interaction and this mechanism plays a minor role in the measured single-nucleon removal cross section.

  Nevertheless, electromagnetic excitations are not the only resonances that can be excited in high-energy nuclear collisions. The excitation of the giant quadrupole resonance (GQR), understood as a surface oscillation of nucleons, isovector or isoscalar depending if protons an neutrons are oscillating opposite or in phase to each other, might also be an important contribution to the one-neutron removal channel. Measurements on the excitation energy spectrum of this resonance show that for medium-mass nuclei it is found over the particle-emission threshold [17] and, as a consequence, it also contributes to the one-neutron removal channel.

  A precise calculation of both contributions is performed in this work, details on the fraction of the one-neutron removal cross section coming

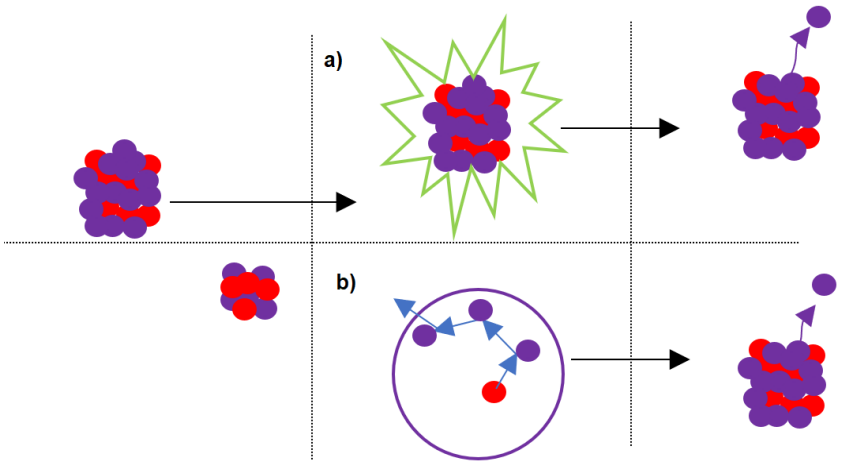

Figure 1.2: *Schematic representation of initial and final state interactions in a nucleus-nucleus collision. The first panel represent a standard nucleus-nucleus collision, then the upper panels shows a situation where no nucleons are knock-out in the collision but a collective nuclear mode is excited; As a consequence, a neutron is ejected. The second situation reflects a case where a nucleon is knock-out in the collision but on its way out, it scatters with several nucleons; Consequently, not only the original knocked-out nucleon is removed but a second one is ejected*

from the excitation of collective nuclear modes are provided in the following chapters.

- **Final state interactions**

  Whenever a nucleon is removed from a fast moving projectile in a nuclear collision it has a non-zero probability to scatter with other nucleons in its way out. Such an effect will also contribute to increase the overall excitation energy of the A-1 residue.

  This increase of the excitation energy will reduce the survival probability of the A-1 residue, affecting directly to the final value of the A-1 production cross section. This effect is also considered in this work and the details are discussed in the following chapters.

Apart from the cross section, the longitudinal momentum distribution of the A-1 residue represents another important experimental observable. In the framework of the sudden approximation described below [18], the momentum transfered to the heavy residue must be equal to the momentum of the removed nucleon $\vec{k}_n$ before the collision.

$$\vec{k}_n = \frac{A-1}{A}\vec{k}_A - \vec{k}_{A-1} \tag{1.1}$$

Thus, the momentum distribution of the projectile-like fragment carries the information of the orbital angular momentum l of the removed nucleon. This, combined with the measured partial cross sections to the different final states provides information on the relative occupancies of the single-particle states contributing to the ground state wave function of the initial nucleus.

1.3 Reaction theory

One of the key aspects of using these reactions with fast radioactive secondary beams is precisely the fact that, due to their high-energy, a semi classical description of the reaction process can be used. At these energies, the interaction time is sufficiently short and the relative motion of the nucleons inside the nucleus can be neglected. Then, the reaction can be described in terms of single nucleon-nucleon collisions simplifying the mechanism. This is known as "*sudden*" or "*adiabatic*" approximation [18]. Moreover, at these energies a framework of straight-line trajectories known as the "*eikonal*' approximation can be applied, since the scattering process is dominated by forward angles [19]. Under these approximations the reaction can be described using the Glauber's picture [20], a multiple high-energy scattering theory where the nucleus-nucleus collision is described in terms of multiple nucleon-nucleon collisions in the overlap region between the projectile and the target. According to this theory, the probability T(r) for the projectile nucleus to go through the target without interacting is calculated as follows:

$$T(r) = exp\left[-\bar{\sigma}\int_{\infty}^{\infty}\rho_t(r,z)\rho_p(r,z)\right] \tag{1.2}$$

where $\bar{\sigma}$ is the nucleon-nucleon cross section and $\rho_{t(p)}(r,z)$ are the projectile and target radial density distributions. Eq 1.2 represents the overlap of the target and projectile radial density distributions with r being the impact parameter and z the axis of the beam direction.

Then, the total reaction cross section σ_R can be obtained by calculating the integral of T(r) over the impact parameter,

$$\sigma_R = 2\pi\int_0^{\infty}\left[1-T(r)\right]rdr \tag{1.3}$$

It has been widely studied which are the best parametrizations of the nuclear density distributions. Karol proposed that for light nuclei (A<40) the best description is provided by gaussians [21],

$$\rho(r) = \frac{A}{(a\sqrt{\pi})^3} e^{-(R/a)^2} \tag{1.4}$$

where the a parameter is related to the root mean square radius R_{rms} by $a = R_{rms} \cdot (1.5)^{-1/2}$.

For heavier nuclei the density profile changes and a more elaborated parametrization is needed. Fermi I functions are found to be the best option to describe heavier nuclei.

$$\rho(r) = \rho(0)\,\{1 + exp\,[(r - R)/4.4t]\} \tag{1.5}$$

where R is the half-central-density radius and t is the surface skin thickness parameter.

It is shown in [21] that these parametrizations of the nucleon density distributions show a very good agreement with the data and this method is very useful for the calculation of total reaction cross sections. Modern calculations use directly the radial distributions obtained from HFB calculations.

In addition, this description of the nucleus-nucleus interaction can also be used to describe the production of an A-1 fragment in a collision. In this theoretical framework, the cross section for the production of a (Z_f,N_f) fragment from a (Z_p,N_p) projectile is described as follows;

$$\begin{aligned}\sigma = N(Z_p, N_p; Z_f, N_f) \int d^2b\,[1 - P_p(b)]^{Z_p - Z_f} \\ \cdot P_p(b)^{Z_f}\,[1 - P_n(b)]^{N_p - N_f}\,P_n(b)^{N_f}\end{aligned} \tag{1.6}$$

where the factor N(Z_p, N_p; Z_f, N_f) takes into account all the possible combinations to obtain Z_f protons and N_f neutrons, and P_p and P_n are the single-nucleon survival probability functions for protons and neutrons which depend strongly on the nucleon density distributions and nucleon-nucleon cross sections. For the particular case of the single-nucleon knockout, $Z_p - Z_f$=1 or $N_p - N_f$=1.

After the collision the de-excitation of the knockout remnant takes place. The excitation of the (Z_f, N_f) core is considered from the holes created in the Fermi distribution of single-particle levels. Each hole corresponds to a vacant state created during the collision time and the density of states is obtained by taking into account all the possible hole-combinations consistent with the produced fragment. Then, the de-excitation of the core should be considered to obtain the final value of the inclusive cross section.

Following these ideas, exclusive cross sections for the removal of a nucleon from a single-particle orbital populating a hole state I^π in the residue are

described as the product of the single particle cross section σ_{sp} calculated following the Glauber's theory and the spectroscopic factor C^2S [19]. Here, σ_{sp} describes the reaction mechanisms leading to the removal of a nucleon and C^2S is related to the occupation at the single-particle level.

$$\sigma(I^\pi) = \sum_j C^2S(j, I^\pi)\sigma_{sp}(j, S_N + E_x(I^\pi)) \tag{1.7}$$

where $S_N + E_x(I^\pi)$ is the effective binding energy of the removed nucleon, being S_N the nucleon's separation energy and $E_x(I^\pi)$ the excitation energy of a given final state of the reaction residue. The summation over j takes into account all of the allowed angular-momentum transfers.

The single-particle cross sections σ_{sp} are given as the sum of the the stripping (str) and diffractive (diff) contributions. The first accounts for all the events in which the removed nucleon excites the target and is absorbed. The second, describes the cross section for the elastic breakup of the projectile with the target remaining in its ground state. The spectroscopic factors C^2S for a removal of a nucleon with quantum numbers (nlj) are obtained from shell model calculations [22]

A microscopic calculation based on a Monte-Carlo description of the Glauber's theory is given by intra-nuclear cascade models (INC) [23]. Here, the collision is described as successive relativistic binary nucleon-nucleon collisions separated in time and space. The particles travel along straight lines with their evolution followed as time evolves until they collide with another nucleon or they reach the surface, where they eventually escape the nucleus. At the end of the intranuclear cascade, an excited remnant is left, and an external de-excitation model should be coupled in order to obtain the final value of the cross section.

Using the Glauber's theoretical framework, single-nucleon knockout reactions have been widely used to obtain spectroscopic information from short-lived species using radioactive ion beams. Combining the information implicit in the momentum distribution of the A-1 fragment and the partial cross sections from different excited states, single-particle occupancies can be inferred and expressed through the deduction of spectroscopic factors. In addition, even though the inclusive cross section do not carry explicit spectroscopic information, the implicit overall shell-model strength can be compared to model calculations. Moreover, they are a powerful tool to investigate the reaction mechanism and its different contributions.

1.4 From nucleon-removal to single particle information

The first results evidencing the sensitivity of the momentum distribution of the heavy residues produced in knockout reactions to the internal structure of the projectile nucleus were obtained studying the break-up reaction of the ^{11}Li halo-nuclei [24] at the National Superconducting Cyclotron Laboratory (NSCL). The parallel momentum distributions of the ^{9}Li fragments were measured yielding two important conclusions. By comparing the width of the distributions for high-Z and low-Z reaction targets, the independence of this measurement from the nature of the interaction was clear. In addition, the validity of this method as a direct measurement of the large spatial distribution of the wave function was confirmed through the determination of the root-mean square (rms) radius of ^{11}Li.

A systematic study of one-neutron removal cross sections for neutron-rich psd-shell nuclei performed at GANIL, investigated the nuclear structure of light nuclei through the parallel momentum distributions of boron, carbon, nitrogen, oxygen and fluorine A-1 fragments [25, 26]. This work showed how the shape and width of the momentum distributions changes drastically when crossing the N=8 and N=14 neutron shells. A similar behavior was observed at the NSCL searching for changes in nuclear structure in the sd shell through one-proton removal reactions of proton-rich phosphorus isotopes [27]. Also, at the GSI, one-nucleon removal cross sections of boron and carbon isotopes showed that these measurements provide important nuclear structure information [28]. Consequently, the sensitivity of the neutron removal reactions to changes in nuclear structure was clearly demonstrated. Indeed, important conclusions were drawn regarding the evolution of the shell structure near the drip lines investigating the one-neutron removal from a ^{12}Be projectile [29]. Strong evidence for the vanishing of the N=8 shell gap was found by observing intruder configurations from the next-higher shell in the ground-state wave function of ^{12}Be.

More evidences of changes in nuclear structure near the drip lines were obtained at the GSI facility, measurements of the ^{22}O momentum distribution after one-neutron knockout from ^{23}O lead to the confirmation of the existence of N=14 and N=16 subshell closures for Z=8 isotopes [30].

1.4.1 Weakly-deeply bound nucleons

The independent particle model (IPM) provides a picture of the nucleus where nucleons are allowed to move freely in an average potential created

by the interaction with other nucleons. In this picture, states close to the Fermi level are described to be completely filled. However results obtained in electron scattering *(e,e' p)* experiments evidenced a deviation from this simple description showing a reduction of 30% - 40% of the single particle strength of the valence protons in comparison to the predictions of the IPM [4]. Correlations between nucleons leading to a redistribution of the single-particle strength above the Fermi level was claimed to be a possible reason for this deviation.

In modern nuclear shell model calculations, long-range correlations between nucleons are taken into account. This result in a better description of the reduction of the physical occupancies of states near to the Fermi surface with the single-particle strength being fragmented to higher-energy states. In order to have an indicator of the validity of the predicted occupancies by the shell-model, the reduction factor R_S is defined as the ratio between the experimental an theoretical single-nucleon knockout cross sections calculated under the eikonal approximation with an associated spectroscopic factor calculated with shell model calculations.

$$R_s = \frac{\sigma_{exp}}{\sigma_{th}} \tag{1.8}$$

The investigation of the one-neutron removal reaction from ^{32}Ar at 65.1 MeV/A [31], an isotope with an estimated neutron separation energy of 21.99 MeV going to ^{31}Ar, whose ground state is the only bound state, showed surprising results. The comparison between the experimental value an the theoretical one gave a relatively high reduction factor $R_S = 0.24$ (3). This result indicated a very strong reduction of the spectroscopic strength compared to the one predicted by the shell model.

At the same time, measurements from the removal of a neutron in ^{22}O [25], an isotope with the same number of neutrons as ^{32}Ar but only eight protons, delivered a much lower reduction factor $R_S = 0.70$ (6). These results suggested a strong correlation of the reduction factor with the neutron-proton asymmetry of the nucleus.

This suggestion of a dependence of the ratio between experimental and theoretical inclusive one-nucleon knockout cross sections with the proton-neutron asymmetry of the nucleus was later extended to a long range of measurements [5].

Figure 1.3 shows the relation between the reduction factor of the experimental ant theoretical inclusive one-nucleon removal cross section as a function of ΔS. This parameter is an indicator of the neutron-proton asymmetry of the nucleus. It is defined as $\Delta S = S_n$ - S_p for neutron removal and $\Delta S = S_p$ - S_n for proton removal where $S_{p(n)}$ is the proton (neutron) sep-

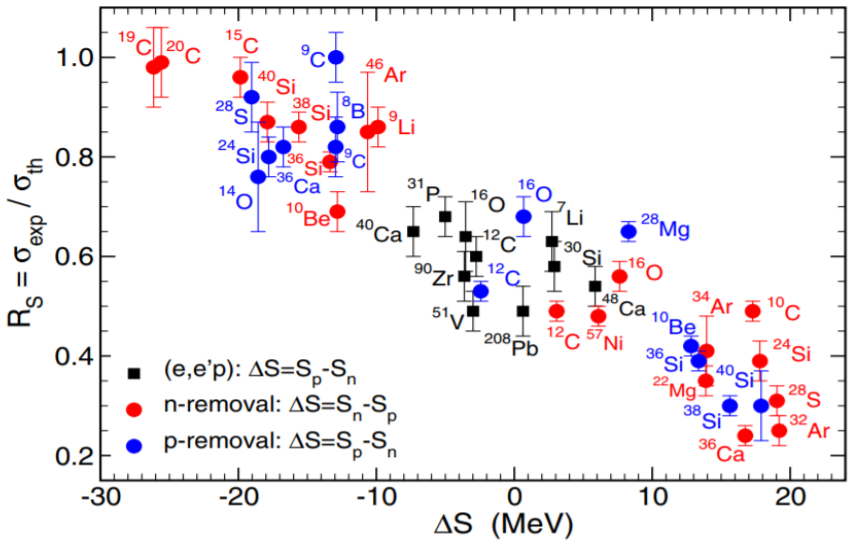

Figure 1.3: *Reduction factor R_S shown as a function of ΔS, an indicator of the symmetry energy of the neutron and proton Fermi surfaces. The red points are for neutron-removal cases and the blue points those for proton removal. The solid (black) squares, are deduced from electron-induced proton knockout data. This figure was obtained from reference [5].*

aration energy. Then, this magnitude takes negative values for the removal of weakly bound nucleons and positive values for the removal of the deeply bound ones.

The results shown in figure 1.3 suggest a strong dependence of the reduction factor on the isospin asymmetry of the nucleus. The good experimental-to-theory agreement found with the removal of weakly-bound nucleons suggest that the nucleon correlations that lead to a fragmentation of the single particle strength above the Fermi level are properly addressed in the shell model. However, this agreement begins to fade when calculating the removal of deeply bound-nucleons, here, the spectroscopic strength predicted by the shell model seems to be far from being correct and a large overestimation of the experimental result is observed. This behavior is often attributed to short-range correlations between nucleons.

However, results obtained from transfer reactions at low beam energies on oxygen, argon and helium isotopes contradict the reduction factor dependence on the neutron-proton asymmetry of the nucleus [7, 8, 9]. A rather constant quenching of the spectroscopic factors with no isospin dependence was observed. Moreover, very recent results obtained by the R^3B collaboration on quasifree *(p,2p)* reactions on oxygen isotopes at beam energies

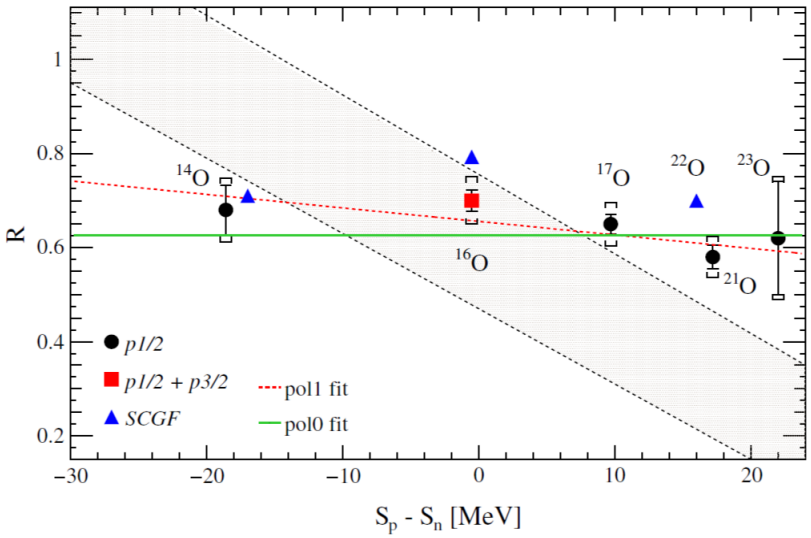

Figure 1.4: *Reduction factor R deduced from (p,2p) cross section (circles and squares) as a function of S_p - S_n compared to theoretical SFs calculated with SCGF (triangles). The shaded area indicates the trend from an analysis of intermediate-energy one-nucleon removal cross sections. This figure was obtained from reference [6].*

around 400 MeV/A [6] provided a similar result. Reduction factors were determined for proton- and neutron-rich oxygen isotopes indicating a weak or even no dependence on the proton-neutron asymmetry. In addition, the result for the stable ^{16}O is in good agreement with the data obtained from *(e,e' p)* experiments.

Although the recent results showed in figure 1.4, and the results obtained in transfer reactions seems to contradict the previously suggested dependence of the one-nucleon removal cross sections with the isospin asymmetry, they still show a quenching between the experimental and theoretical results around 0.66 [6], which means a relatively large overprediction of the experimental value. It appears that the quenching of the single-particle occupancy of states is a universal property of the many body system. The present theoretical framework overestimates the probability of producing bound states when removing a deeply-bound nucleon which might be a hint of beyond-shell-model correlations reducing the survival probability of the A-1 residue.

At the same time, J.L. Rodríguez-Sánchez *et al* [32] have shown a different strategy to approach the problem. A systematic of inclusive 1-neutron and 1-proton knockout cross sections of tin isotopes have been measured and studied in the framework of the Glauber model [33]. Here, the probability of producing an A-1 fragment was calculated using equation 1.6. Then,

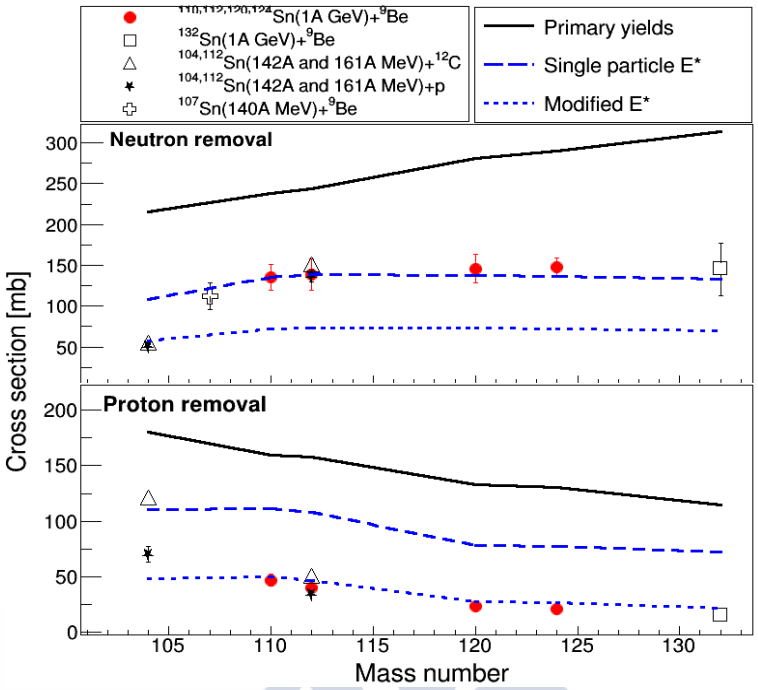

Figure 1.5: *(a) Neutron-removal (upper panel) and proton-removal (lower panel) cross sections measured for different tin isotopes covering a large range in neutron excess: Pérez Loureiro et al. (open squares) [34], Audirac et al. (open triangles and solid stars) [35], Cerizza et al. (open cross) and J.L. Rodríguez-Sánchez et al [32] (solid red dots). This set of data is compared with Glauber model calculations (lines).*

the excitation energy induced in the collision to the projectile-like fragment was calculated from particle-hole excitations and the de-excitation of the core is performed according to the Weiskopf's formalism with the survival probability of the fragment calculated through the competition between the excitation energy and the particle emission threshold. The ABLA07 code is used to de-excite the unbound remnants (fragments whose excitation energy is above the nucleon's separation energy) emitting γ rays, neutrons, light-charged particles and heavier fragments.

Figure 1.5 shows the results obtained in Ref.[32]. Here, the removal of weakly-bound nucleons is well described assuming the excitation energy calculated under the single-particle-hole picture, but it is needed to increase arbitrarily the excitation energy to describe the removal of deeply bound protons in neutron-rich isotopes. Around 50% overprediction of the cross section is observed for the removal of deeply-bound nucleons.

However, this result is not surprising, the fact that the excitation energy

induced by single-particle holes in peripheral nucleus-nucleus collision at relativistic energies is not sufficient to describe the excitation energy gained by the projectile-like fragments was already observed by *K. H. Schmidt et al* years ago [36], claiming that final-state interactions could be a possible source of additional excitation energy.

Figure 1.5 also shows data from other experiments, and this behavior seems to be a common trend. Audirac *et al.* [35] studied the removal of the weakly/deeply bound species in ^{104}Sn and ^{112}Sn at 160 MeV/A through the Intranuclear cascade model (INC) [37], finding the same result, an overprediction of the removal of deeply bound nucleons.

G. Louchart et al approached this problem with a model at the interface of the intranuclear cascade model including a simple description of the nuclear structure and the microscopic eikonal approach [38]. This new approach showed important improvements in the description of the removal of deeply-bound species. Here, the decomposition of the one-nucleon cross section into direct events, multiple scattering and evaporation components showed that the incorporation of indirect mechanisms and core excitations play an important role in the reaction mechanism.

To sum up, an overall overprediction of the single-nucleon knockout cross section similar to the one obtained in *(e,e' p)* experiments is observed in a wide variety of studies. In particular, the removal of deeply-bound nucleons seems to be a challenge point for theory. Then, either the description of the reaction itself is not properly addressed or the excitation energy of the single-particle hole picture overpredicts the probability of producing bound states of the A-1 residue. Final state interactions, nuclear excitations or short-range nucleon-nucleon correlations are the main candidates for being at the origin of this disagreement.

1.5 Short-range correlations in neutron-rich nuclei

Understanding short-range correlations between nucleons have been one of the most elusive goals for nuclear physics over the last decades. Recently, high-energy electron- and proton- scattering experiments demonstrated the existence of nucleons forming short-range correlated pairs with high relative momentum, greater than the Fermi momentum of the system [10, 39, 40]. This could be a crucial feature for the description of single-nucleon knockout reactions, considering that whenever one of the correlated nucleons is removed from the projectile in a nucleus-nucleus collisions, its partner nu-

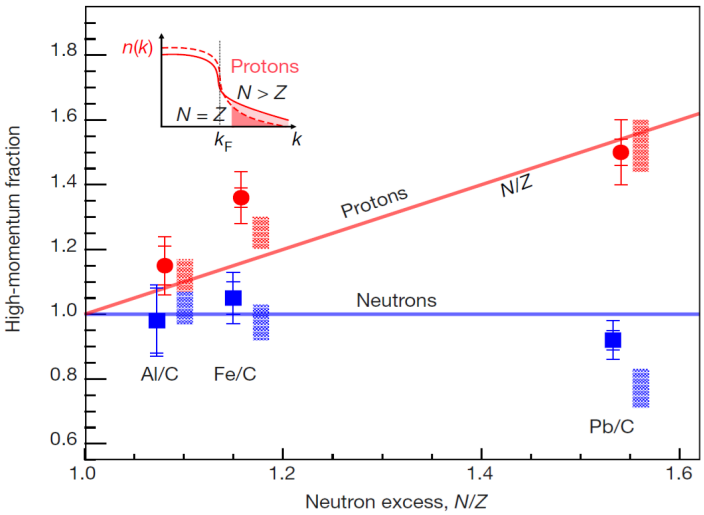

Figure 1.6: *Relative high-momentum fractions for neutrons and protons. Red circles with error bars describe the ratio of high-momentum to low-momentum proton relative to carbon. Blue squares with error bars show the same for neutron events. Red and blue rectangles show the range of predictions of the phenomenological np-dominance model. The red line and the blue line are drawn to guide the eye. The inset shows how the fraction high-momentum protons increases with the number of neutrons (shaded region). This picture is obtained from reference [12].*

cleon is automatically ejected from the knockout fragment [11]. In addition, the formation of a high-momentum tail with $k{>}k_F$ in the state occupancy distribution of nucleons inside the nucleus, could lead to a reduction of the occupancy of nuclear states close to the Fermi level of the system.

In high-energy electron-scattering experiments, electrons scatter from the nucleus transferring a single virtual photon with momentum q which is absorbed by a nucleon with initial momentum p_i. Then, the nucleon emerges with a final momentum $p_f = q + p_i$ and the initial momentum can be reconstructed from the difference between the momentum of the detected nucleon and and the momentum transferred. Within this framework, it has been shown that ∼20% of nucleons in nuclei have momentum grater than k_F [40]. In addition, the fraction of neutron-proton short-range-correlated pairs seems to dominate over the neutron-neutron and proton-proton pairs by a factor of ∼20 [41], which is known as *np*-dominance.

The changes in the relative fractions of high-momentum protons and neutrons with the neutron-proton asymmetry of the nucleus were studied in Ref. [12]. Here two important conclusions were obtained. The fraction of high-momentum neutrons to high-momentum protons is consistent with unity for

all the measured nuclei from ^{12}C to ^{208}Pb. The first is a very symmetric nuclei, with the same number of neutrons and protons, while the second one has 1.53 more neutrons than protons. As a consequence of this, for very asymmetric nuclei the relative fraction of high momentum nucleons is bigger for the minority specie than for the majority. As an example, if 20% of the 132 nucleons of ^{132}Sn form short-range correlated neutron-proton pairs, this consists in 13 protons and 13 neutrons. Then, the relative fraction of high momentum neutrons is 13/82$\sim$15% and the relative fraction of high momentum protons is 13/50$\sim$26%.

This is shown in figure 1.6 where the relative fractions of high-momentum protons and neutrons are shown relative to carbon as a function of the neutron excess (N/Z) of the nucleus. It is seen, that the fraction of high-momentum protons increases by about 50% from carbon to lead while the corresponding fraction of high-momentum neutrons seems to decrease by about 10%$\pm$5% in the same range.

These results provide strong evidences on the presence of short-correlated nucleons in nuclei. According to Ref.[11], short-range correlated nucleons will contribute to reduce the survival probability of the A-1 fragment produced in a single-nucleon knockout reaction. This effect will systematically decrease the measured cross sections in single-nucleon knockout experiments, as only the knockout of non-correlated nucleons is measured.

Even though further research is needed to understand if this phenomenom is responsible for the reduction of the spectroscopic strength witnessed in a broad range of single-nucleon knockout measurements, it seems clear that the impact of this effect scales with the neutron-proton asymmetry of the nucleus. Being more important in knockout reactions where the removed nucleon is a deeply-bound nucleon.

USC
UNIVERSIDADE
DE SANTIAGO
DE COMPOSTELA

Chapter 2

Description of the experiment

This chapter will be dedicated to the description of the experimental setup used to investigate one-nucleon removal and total reaction cross sections of medium-mass neutron rich nuclei. Because most of the investigated nuclei are not stable, the experiment was performed using inverse kinematics at relativistic energies.

When using the inverse kinematics technique, the reaction products are emitted in the forward direction and can then be separated and identified using a high-resolution magnetic spectrometer. One of the main challenges of these experiments is the high-precision needed to perform the measurements, keeping the uncertainties at a reasonable level. Due to this, high production rates and a very clean separation of the reaction products is needed. The relatively high amount of detectors needed to perform an unambiguous identification of the reaction fragments required the reaction to be performed at very high energies.

The GSI facility in Darmstadt, Germany offered the best conditions to perform the experiment. Two different reaction mechanisms, fission of ^{238}U at 950 MeV/A and fragmentation of ^{132}Xe at 1200 MeV/A, allowed the production of a wide variety of medium-mass neutron rich nuclei. A two-step reaction scheme, where the FRS was used as two independent spectrometer enabled the study of the interaction of those nuclei with a thick beryllium target, measuring the cross sections for the reactions investigated.

This chapter includes a brief description of the experimental facility and the detection setup of the experiment. In addition, the detection techniques and the identification method used to separate and identify the reaction products are explained so one can understand the full separation procedure.

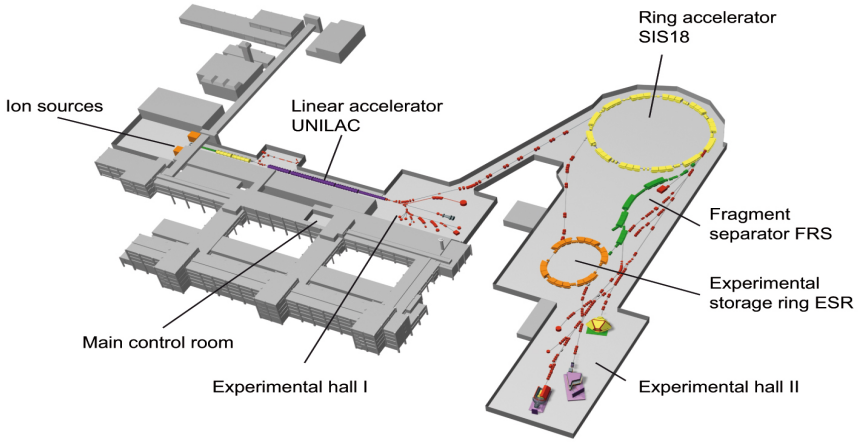

Figure 2.1: *Schematic representation of the GSI accelerator facility. The three different accelerator regions are highlighted together with the main experimental caves. The FRS is located just at the exit of the SIS18 ring accelerator.*

2.1 The GSI acceleration facility

The GSI acceleration system consists of three different stages. Starting at the first step, the ion sources produce the ions that are afterly accelerated in two consecutive accelerators, UNILAC and SIS18. Positively charged atoms are produced by stripping the electrons of the shell of the atom.The GSI is capable of producing ions of many different kinds of elements, more than any other laboratory in the world. This range from simple hydrogen atoms to uranium, the heaviest of all the stables nuclei present on Earth. At the ion source, ions are accelerated up to 0.2 percent of the speed of light.

After the ions are collected from the ion sources, they are injected into the linear accelerator, UNILAC (Universal Linear Accelerator). On a length of 120 meters, ions of all kinds are accelerated up to 20 percent of the speed of light.

From UNILAC, already accelerated ions are injected into the ring accelerator SIS18 to accelerate them up to relativistic energies. They circulate inside the ring passing the so-called acceleration structures where their high-voltage accelerate them on every circulation while the magnets keep the ions on their circular path. Once they have reached the desired speed, they are delivered to the different experimental caves.

In our experimental scheme, two different beams of ^{238}U and ^{132}Xe were accelerated up to 950 Mev/A and 1200 MeV/A respectively. For both beams,

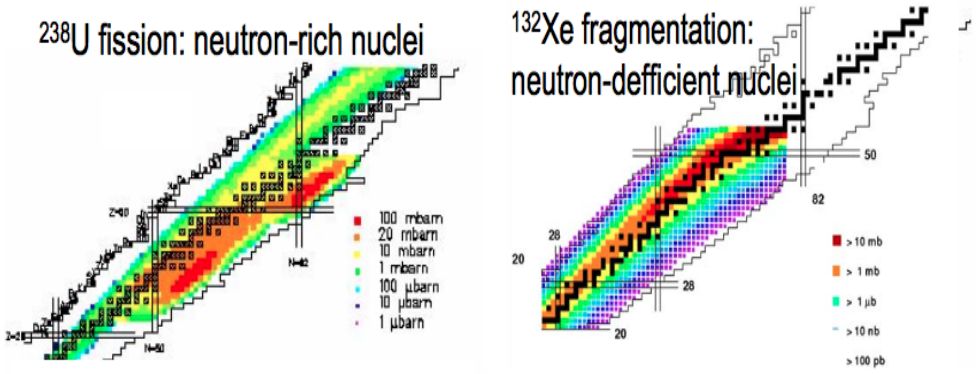

Figure 2.2: *Schematic vision of the chart of nuclides where highlighted the nuclei produced with both reaction mechanisms. The left pannel shows the production of nuclei via fission of ^{238}U and the right pannel shows the fragments produced via fragmentation reactions of ^{132}Xe.*

the GSI acceleration system is capable of sustaining rather high intensities, up to 10^9 ions per spill, as required in our experiment. After the acceleration, the beam was driven to the Fragment Separator target area to induce the reactions leading to the production of the medium-mass neutron-rich nuclei investigated in this work.

2.2 Production of medium-mass neutron-rich nuclei

One of the main objectives in this experiment was to produce long isotopic chains of medium-mass nuclei. The idea of covering a wide range in isospin was very attractive to study systematic effects in this region. For this purpose two different production mechanisms requiring the use of two different primary beams were employed. Fission of a 950 MeV/A ^{238}U primary beam enhanced the production of neutron-rich nuclei with a large production close to the magic number N=82. The fragmentation of a 1200 MeV/A ^{132}Xe magnified the production of neutron-defficient nuclei. Combining both reactions, several hundreds of medium-mass nuclei were produced from one side to the other of the chart of nuclides.

Systematic structural effects along long isotopic chains can be studied by using appropriate reaction mechanisms. In particular, we investigated the total interaction cross section and the single-nucleon knockout cross section. For this purpose, the experiment was developed employing a two-step

Target	Thickness mg/cm^2
Be	1036 ± 1
Pb	649 ± 5
Pb	1534 ± 7
Be^{Frag}	2591 ± 90

Table 2.1: *Summary of the different targets used in this experiment.*

reaction mechanism.

The idea is to use the FRS to produce and investigate secondary radioactive ion beams. For this end, the FRS is used as a two-step magnetic spectrometer. The first half of the separator is used to identify the secondary beams produced in the interaction of the high-energy stable ion beams in a first production target located at the entrance of the spectrometer. Then, the second part is used to study the fragmentation of the secondary beam as a result of the interaction with a second target located at the middle focal plane of the spectrometer. An unambiguous identification of the incoming and outgoing ions is needed, and for this purpose each stage is equipped with the needed detectors to measure magnetic rigidity, energy loss and time of flight.

Figure 2.2 shows the expected production of nuclei at the entrance of the FRS with the two reaction mechanisms used in this experiment. Furthermore, the above-mentioned primary beam energies together with the thickness and the specie of the production target, were suited so that the energy per nucleon of the secondary projectiles at the middle of the reaction target were in the range of 1 GeV/A.

The FRS was always tuned to maximize the transmission of the central trajectory. However, the magnetic settings can be configured in order to change the isotope which will follow the central path of the separator. Therefore, in order to maximize the optical transmission of the highest number of isotopes, a total of 10 different magnetic settings were used in this experiment. Settings centered in ^{113}Sn, ^{119}Sn, ^{121}Sn, ^{124}Sn and ^{126}Sn are those corresponding to the production of neutron-defficient isotopes via projectile fragmentation. On th other hand, settings centered in ^{126}Sn, ^{128}Sn, ^{130}Sn, ^{132}Sn, ^{134}Sn and ^{136}Sn correspond to the production of neutron-rich nuclei via fission of ^{238}U.

The targets and their properties used in this experiment are described in table 2.1. On one hand, the fragmentation of the ^{132}Xe primary beam is induced with a 1036 ± 1 mg/cm^2 target. On the other hand, a 649 ± 5 and

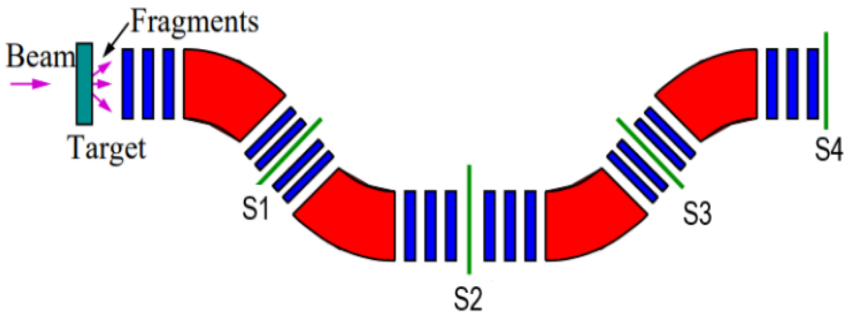

Figure 2.3: *Schematic representation of the FRS FRagment Separator.*

a 1549 ± 7 mg/cm^2 Pb targets are used to induce fission on the ^{238}U. The fragmentation of the secondary beam is measured through its interaction with a 2591 ± 7 mg/cm^2 Be target which is common to both production reaction mechanisms.

2.3 The Fragment Separator

The FRS (FRagment Separator) focuses on producing and investigating exotic nuclei. It is an achromatic magnetic forward spectrometer where heavy-ion beams with magnetic rigidities from up to 5 to 18 Tm can be analyzed. The system has four independent stages, each consistent of a 30° dipole magnet and a set of quadrupoles before and after the dipole in order to fulfill first-order focusing conditions. The quadrupole magnets in front of the dipole are adjustable to properly illuminate the field volume of the bending magnets to achive a high resolving power. The quadrupoles following the dipole magnets determine the ion-optical conditions at the four focal planes, named in figure 2.3 S1, S2, S3 and S4. The sextupoles in front and behind the dipole are used to higher order optical corrections.

Even though the FRS can be operated in three different optical modes, the achromatic standard mode was used in this experiment. Here, point-to-point images in the horizontal direction are required at all four focal planes while waists in the y direction are required only at S2 and S4. Moreover, the momentum dispersion of the first and the second dipole (D_{02} = -6.54 cm/%) is canceled by that of the third and the forth (D_{24} = 7.75 cm/%). This compensation between the dispersion of both halves of the spectrometer results in an achromatic system with a magnification of V = D_{24}/D_{02} = 1.185.

The FRS is limited by its maximum acceptance. The angular acceptance,

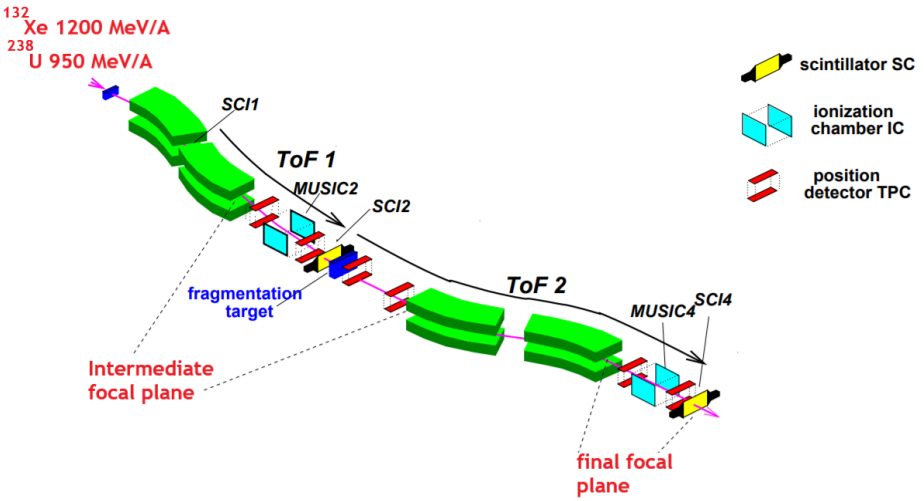

Figure 2.4: *Schematic representation of the FRS FRagment Separator.*

given by the physical transverse aperture of the magnetic elements, is limited to ±15 mrad aroung its central trajectory. In addition, the momentum acceptance given by its ion-optical properties is limited to ±1.5%. The maximum magnetic rigidity (18 Tm) is determined by the radius of the dipole magnets (∼ 11 m) and maximum magnetic field (1.6 T).

2.4 The detection system

The detection system used in this experiment to unambiguously identify the incoming and outgoing ions is described in this section. The mid-focal plane (S2) is used for the detection of the incoming secondary beam and the final focal plane (S4) is used as the detection stage for the outgoing reaction products. Each of the detection stations is equipped with time-projection chambers, multisampling ionization chambers and plastic scintillators for measuring magnetic rigidity, atomic number and time of flight of the transmitted nuclei.

Time projection chambers

Four time-projection chambers (TPCs) [42] were placed at the intermediate focal plane to track the transmitted nuclei by measuring their x and y position. Two of them are located before the reaction target in order to measure the magnetic rigidity of the incoming secondary beam, and the other two are located after the target, to track the trajectories of the outgoing

reaction products. Furthermore, two additional TPCs are placed at the final focal plane to measure the magnetic rigidity of the fragments reaching the final stage of the spectrometer.

The TPCs used in this experiment consist of a drift space filled with gas inside a uniform electric field terminated by four proportional counters. When a particle passes through the detector, it creates electron-ion pairs along its track. Electrons drift towards the anodes because of the uniform electric field. The electron drift-time is used for the measurement of the y-coordinate. Then, as the electrons are drifting towards the anode, they create an avalanche reaction producing a negative signal which is directly induced in the delay line. After that, the collected signal spreads to both ends of the delay line. The coordinate in the x-direction is determined by the time difference between the arrival of the signal at the left and at the right end of the delay line [42].

The gas used was argon and windows were made of kapton foils. In addition, two delay lines were used to obtain two independent measurements of the x position. Each one was connected to a pair of anodes as can be seen in figure. The position resolution provided with this detectors was better than 0.5 mm.

Plastic scintillators

Three plastic scintillators SC1, SC2 and SC3 with thicknesses of 5, 3.5 and 5 mm respectively located respectively in S1, S2 and S4 are used to measure the time-of-flight of the transmitted isotopes. Each plastic scintillator was coupled to a pair of photomultiplier tubes (PMTs) providing two independent time signals. SC1 and SC2 are used to measure the time-of-flight of the secondary beam and SC2 and SC4 are used to obtain the time-of-flight of the reaction products arriving at the final focal plane S4. In addition, they provide a secondary measurement of the vertical and horizontal positions of the isotopes in their respective locations.

Ionization chambers

Two multisampling ionization chambers (MUSIC) are used to measure the atomic number of the transmitted nuclei. The first one is located before the fragmentation target at S2 and the second one is placed at the final focal plane S4. Whenever a fragment crosses the detector, the applied uniform electric field makes the electrons produced in the gas ionization to drift towards the anodes. The ion loses energy proportionally to the square of its charge and the inverse of its velocity.

Each of the multisampling ionization chambers used in this experiment is equipped with eight active anodes, both are filled with tetrafluoromethane (CF_4) and are 400 mm long. The windows were made of aluminium-coated mylar foils and float glass

Multiwire chambers

Multiwire chambers (MWPC) [43] are proportional chambers used for tracking. Usually, they consist of a grid of uniformly spaced thin anode wires, sanwiched between two cathode planes. The chamber is filled with gas so particles crossing the detector create ion pairs that are drifted towards the anodes due to the presence of a uniform electric field. By decoding in wich of the wires the signal is originated, one can obtain the position of the particle. The spacial resolution of the detector is determined by the anode wire spacing [43].

In our experiment, a set of MWPCs were placed along the beam line and were used mainly for calibration purposes. The calibration is performed adjusting the position of a ^{132}Xe calibration beam at 1200 MeV/ to that of the central trajectory of the spectrometer. In this way, one can determine the rigidity that corresponds to the central trajectory. The beam energy was specifically selected to obtain a magnetic rigidity similar to that of the fission residues.

2.5 The trigger system

Two different triggers were used in this experiment in order to determine the cross sections investigated in this work. This double-trigger system was needed to correctly measure the number of particles for all the produced isotopes impinging in the secondary reaction target located at the intermediate focal plane.

A first trigger named Trigger #1 is given by the scintillator (SC2) placed at the mid-focal plane and correspond to ions that arrived to this scintilliator but did not arrived to the final focal plane. Due to the physical limits of the spectrometer and the magnetic configurations many of the produced ions in the second part of the FRS are lost due to transmission issues. Then, this trigger is needed to count all the isotopes arriving at S2 including those are lost in the second part of the separator.

The second trigger is named Trigger #3 and is given by the scintillator (SC4) placed at the final focal plane. This trigger activates the data acquisition system (DAQ) for the isotopes arriving at the end of the spectrometer.

To avoid double-counting, Trigger #3 had higher priority than Trigger #1, so everytime an isotope arrives at the final focal plane is triggered by Trigger #3 and Trigger #1 is used to activate the DaQ when isotopes to not reach this point of the spectrometer.

In addition, the difference in counting rates between both triggers could be very high, being larger for Trigger #1, specially for those settings centered in the most exotic species. Because of this Trigger #1 can be downscaled in some cases, having reduction factors up to 16 for the most extreme cases.

2.6 Identification of the reaction products

A very good resolution is needed at the intermediate (S2) and final (S4) focal planes of the FRS. The Lorentz force equation describes the motion of a charged particle in the presence of an uniform magnetic field as,

$$F = qvB = \gamma m_0 \frac{v^2}{\rho} \tag{2.1}$$

where B is the magnetic field, ρ represents the radius of the ion inside the magnetic field, γ is the Lorentz factor and m_0 is the rest mass of the ion. From eq 2.1 we can obtain the relation between the mass-over-charge ratio (A/Z), the magnetic rigidity (Bρ) and the velocity of an ion (v).

$$B\rho = \frac{Au}{qe}\beta\gamma c \tag{2.2}$$

where q is the atomic charge state, u is the atomic mass unit, e is the elementary charge, c is the speed of light and $\beta = v/c$. Thus, the identification of an ion in terms of its mass-over-charge ratio can be determined measuring its magnetic rigidity, velocity and atomic charge state Q.

2.6.1 Magnetic rigidity determination

The magnetic rigidity (Bρ) is described in terms of its relative variation with respect to the magnetic rigidity of an ion following a central trajectory in the spectrometer. In the intermediate focal plane, where the identification of the incoming particles is performed, the magnetic rigidity can be determined in terms of the positions of each of the ions with respect to the central trajectory:

$$(B\rho)_{S2} = (B\rho)_c \left(1 - \frac{x_2}{D_{02}}\right), \tag{2.3}$$

where $(B\rho)_c$ is the magnetic rigidity of a central trajectory, x_2 is referred to the position of the ion in the focal plane and D_{02} is the dispersion from the entrance of the spectrometer to the intermediate focal plane.

The position x_2 is obtained from the position measured in the TPC (TPC2) placed before the fragmentation target.The focal plane do not coincide with the position of TPC2. Therefore, x_2 is obtained by propagating the position given by TPC2 to the focal plane. In order to do this, the angle between TPC1 and TPC2 is needed to perform the propagation. Caltulating the exact position of the focal plane is crucial in order to have the better resolution possible when doing the identification plots.

The identification of the outgoing particles is performed at the final focal plane. In this way, the determination of the magnetic rigidity of this fragments is described with the following expression:

$$(B\rho)_{S4} = (B\rho)_c \left(1 - \frac{x_4 - V_{24}x_2}{D_{24}}\right), \tag{2.4}$$

where x_4 is the position at the final focal plane, V_{24} is the magnification and D_{24} is the dispersion between the intermediate and the final focal planes. Again, to obtain the position of the fragment in the final focal plane, the position measured by the last TPC (TPC6) is propagated using the angle measured between the two TPCs (TPC5 and TPC6) placed at the final detection stage.

The magnitude $(B\rho)_c$ is measured using a centered calibration beam and determining the effective radii from the initial $B\rho$ and the measurement of the magnetic fields of the dipoles with the Hall probes. This calibration runs also help us to calibrate the optic parameters of the spectrometer having the following values for $D_{02} = -6.474$ cm/%, $D_{24} = 7.7966$ cm/% and $V_{24} = 1.204$.

2.6.2 Velocity determination

In addition to the magnetic rigidity, another needed magnitude to perform an unambiguous identification of the reaction products is the reduced momentum ($\beta\gamma$). This magnitude is determined measuring the time of flight (ToF) of the reaction products traveling through the spectrometer.

Two different ToF measurements were performed in this experiment. The first one $\text{ToF}^{(1)}$ correspond to the fragments traveling along the first half of the spectrometer, from S1 to S2. The second one, $\text{ToF}^{(2)}$ correspond to the fragments traveling along the second part of the spectrometer, from S2 to S4.

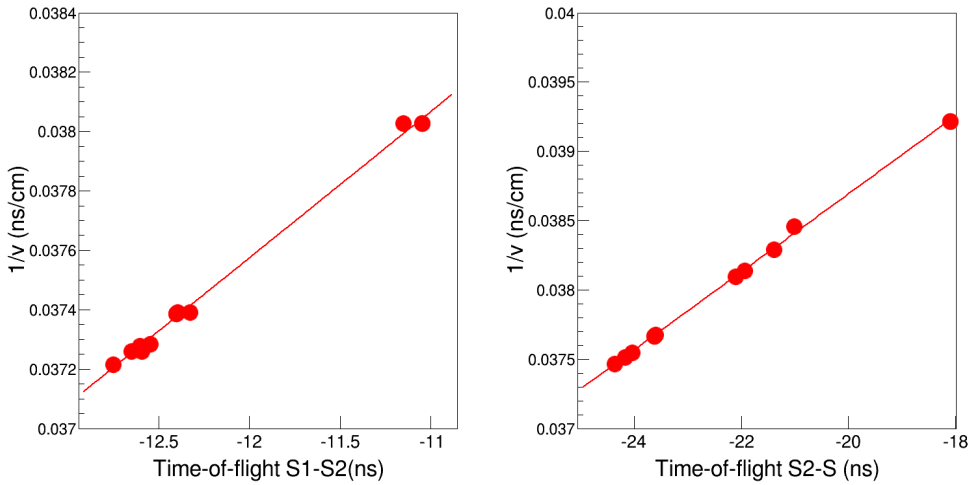

Figure 2.5: *Time of flight (TOF) vs the inverse of the velocitiy plots used for calibration. The left panel corresponds to the calibration of S1-S2 ToF and the right one to the calibration of S2-S4 ToF.*

Each plastic scintillator is coupled to two PMTs. Then, each scintillator provide two different time signals and the time of flight is obtained from the mean value of both signals.

$$ToF^{*} = \frac{1}{2}(\alpha_L \cdot ToF^{*}_{L} + \alpha_R \cdot ToF^{*}_{R}) \tag{2.5}$$

Where ToF* is the time of flight measured averaging both time signals, $\alpha_{L(R)}$ are the TAC calibration factors and ToF$^{*}_{L(R)}$ are the time signals measured in each of the PMTs coupled to the scintillator.

However, as the START signals are given by the scintillators placed at S2 and S4 for ToF$^{(1)}$ and ToF$^{(2)}$ respectively, it is needed to include a delay factor T$_0^{(i)}$ in order to ensure that the STOP signal does not arrive before the START one. Then, the real time of flight value is given by:

$$ToF^{(i)} = T^{(i)}_{STOP} - T^{(i)}_{START} = T^{i}_{0} - TOF^{*(i)} \tag{2.6}$$

The delay factor T$_0^{(i)}$ is obtained comparing the ToF$^{*}_{L(R)}$ signals of the primary beam with the inverse of the velocity (1/v) of the ^{132}Xe primary beam. In order to do this, several calibration runs were taken changing the amount of matter placed along the beam line. The values of the velocities are calculated with the AMADEUS code introducing the exact amount of matter placed in each calibration run. Then, the results are fitted to a first order polynomial as it is observed in figure 2.5.

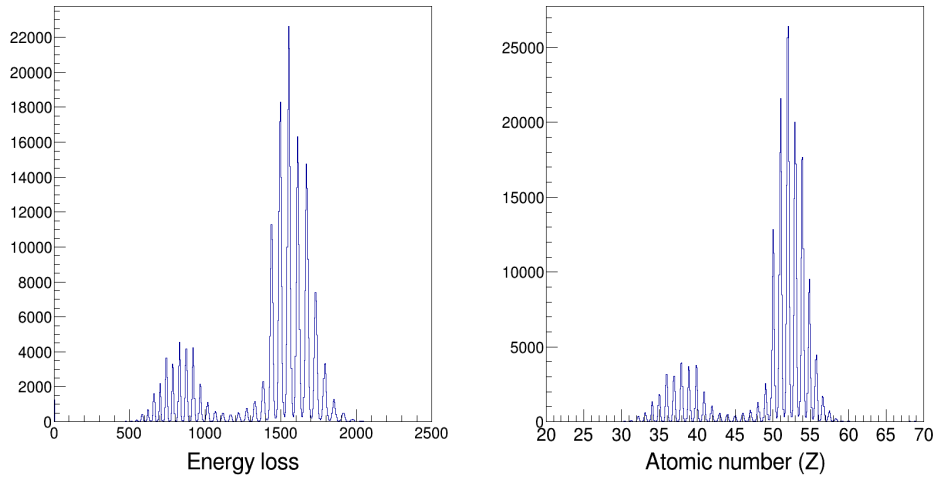

Figure 2.6: *Energy loss calibration at the intermediate focal plane for a magnetic setting of the FRS centered around ^{130}Sn. Left panel shows the measured energy-loss in the MUSIC placed at the intermediate focal plane. Right panel shows the corresponding atomic number identifcation.*

$$\frac{1}{v^{(i)}} = \frac{T_0^{(i)}}{L_0^{(i)}} - \frac{ToF^{*(i)}}{L_0^{(i)}} \tag{2.7}$$

where $T_0^{(i)}$ are the delay values and $L_0^{(i)}$ is the path length of the spectrometer.

2.6.3 Atomic number determination

As it was explained in section 2.4, two multisampling ionization chambers were used to determine the atomic number of the fragments. Here, the energy loss is proportional to the square of its atomic number (Z^2). At this stage of the facility, ions are fully stripped so one can determine Z from the average energy loss of the eight anodes of the detector.

$$Z = A + B\sqrt{\sum_{j=1}^{N} \frac{\Delta E_j}{N}} \tag{2.8}$$

where N is the number of anodes on each detector, ΔE_j is the amplitude of the signals from each anode and A and B are calibration parameters. A and B are determined from the asymmetric charge distribution of fission

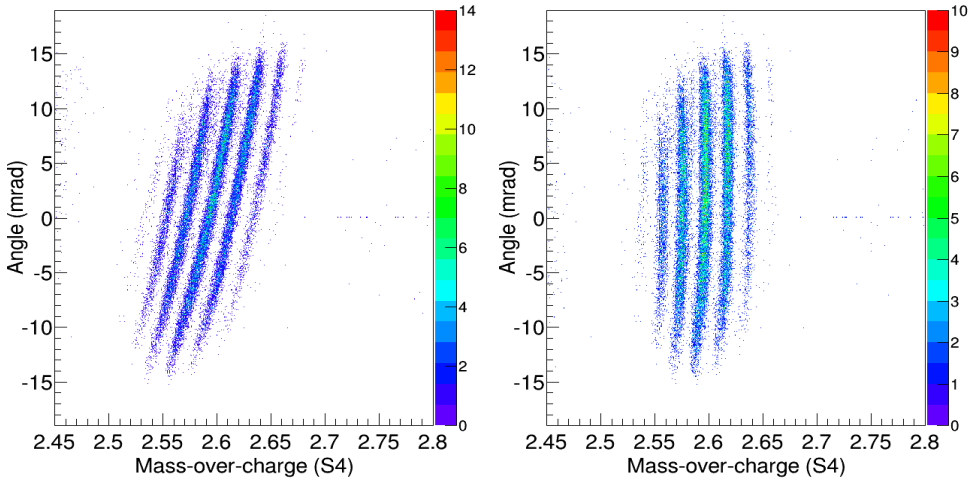

Figure 2.7: *Emitted angle vs the mass-over-charge ratio of the Z=50 fragments fragments transmitted in a magnetic setting of the FRS centered around ^{130}Sn. Left panel shows the existing correlation between both magnitudes. Right panel shows the correction performed in offline analysis.*

products, increasing the production of Te (Z=52) and Zr (Z=40). This can be observed in figure 2.6.

2.7 Mass-over-charge determination

Once the magnetic rigidity, the velocity and the time of flight of the reaction fragments is determined, one can identify each of the isotopes produced in the reaction. However, in order to achieve the best possible resolution, several corrections must be applied in offline analysis.

Angle correction

Ions traveling along the FRS experience different trajectories depending on their properties and thus, the path length for each of them is different. As a consequence, the calculated mass-over-charge ratio show a clear correlation with the horizontal angle α_x.

Left panel of figure 2.7 shows the existent correlation between the measured angle at the final focal plane and the calculated mass-over-charge ratio at S4. On the other hand, the right panel shows the mass-over-charge ratio after eliminating the correlation. Both measured angles at S2 and S4 are corrected following the same procedure. The horizontal angle of the fragments

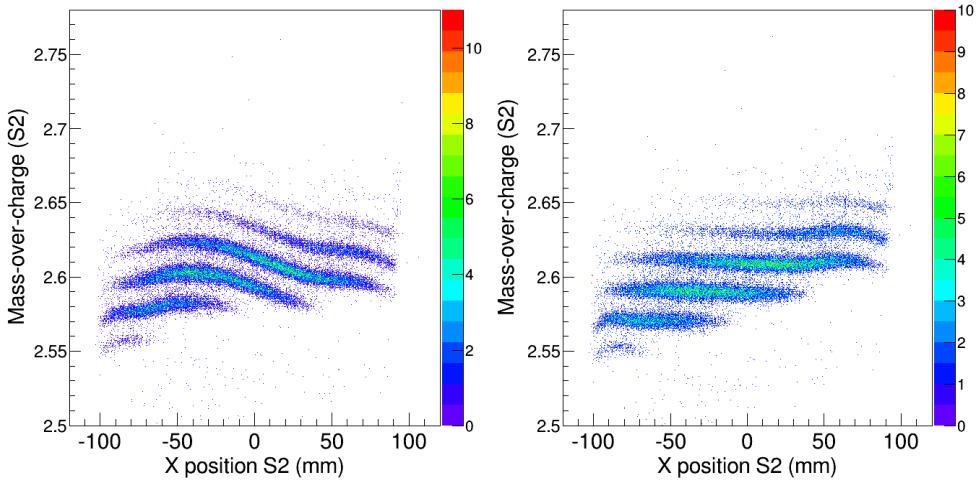

Figure 2.8: *Mass-over-charge vs horizontal position measured with the TPC2 of Z=50 isotopes transmitted in a magnetic setting of the FRS centered around ^{130}Sn. Left pannel shows the existing correlation between both magnitudes. Right pannel shows the correction performed in offline analysis.*

is calculated from the position registered in two consecutive TPCs. This can be expressed as:

$$\alpha_x = \frac{x_{tpc2} - x_{tpc1}}{d_{12}} \tag{2.9}$$

where α_x is the angle in the horizontal direction, x_{tpc} is the position measured in a certain TPC and d_{12} is the distance between two consecutive TPCs.

Position correction

A strong correlation between the position measured at S2 and the calculated mass-over-charge is observed in the left panel figure 2.8. Here, the different isotopes of Z=50 arriving at the intermediate focal plane for a magnetic setting of the FRS centered around ^{130}Sn are shown as a function of their position in the TPC2. This correlation is clear to be stronger when approaching the limits of the detectors. Nevertheless, this correlation generates a strong diffusion when determining the mass-over-charge ratio, producing that the different isotopes emitted in the reaction are all mixed.

The observed correlation is eliminated selecting one of the isotopes shown in the left panel of figure 2.8 and fitting its profile function to a high-order-polynomial function. The best result was provided by a 4^{th} order polynomial

function which is then used to correct the mass-over-charge ratio by simply dividing this magnitude by the given value of the function at each point. This is shown in the right panel of figure 2.8 .

2.7.1 Isotopic identification

Figure 2.9 shows the identification matrix of the fission residues coming from the ^{238}U + ^{9}Be at 950 MeV/A reaction arriving at the intermediate focal plane of the separator. Here, the atomic number is represented as a function of the mass-over-charge ratio. Each of the spots showed in this plot corresponds to one of the isotopes produced in the reaction.

A very good mass resolution ($\Delta M/M = 1.15{\cdot}10^{-3}$) and atomic number resolution ($\Delta Z/Z = 2.6{\cdot}10^{-3}$) is obtained at the intermediate focal plane. This resolution in both magnitudes allow us to perform a very successful separation of the isotopes, one of the key factors when measuring cross sections. At this point, the resolution achieved here allow us to reduce uncertainties when measuring the number of incoming particles of a certain isotope.

Nevertheless, the resolution at the final focal plane is even better. Here, $\Delta M/M = 7.69{\cdot}10^{-4}$ and $\Delta Z/Z = 3{\cdot}10^{-3}$. This allow us to perfectly distinguish between the different reaction products produced in the fragmentation target making easier to measure the number of outgoing particles.

In the following chapters the procedures followed to measure single-nucleon knockout reactions and total reaction cross sections. are described These measurements would not be possible without achieving a very good separation in both focal planes. Therefore, all of the corrections described in this chapter are crucial for the development of this work.

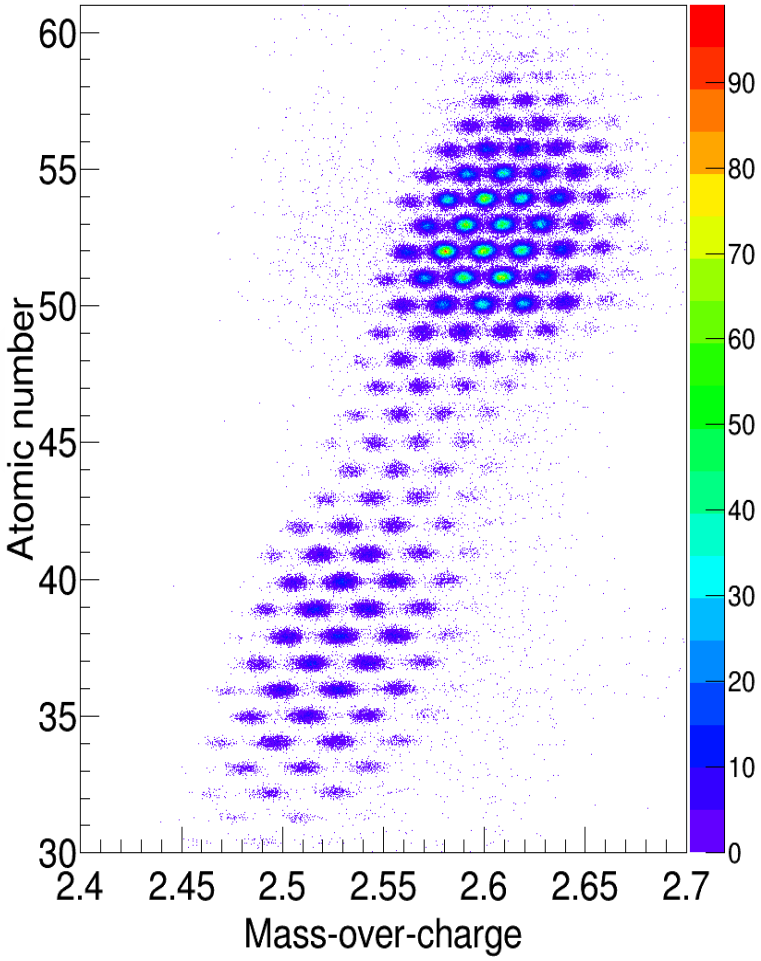

Figure 2.9: *Identification plot showing the atomic number (Z) as a function of the mass-over-charge ratio. This plot correspond to the fission residues produced in the ^{238}U + ^{9}Be at 950 MeV/A reaction transmitted to the intermediate focal plane of the FRS*

Chapter 3

Total reaction cross sections

3.1 Introduction

Total reaction cross sections (σ_R) and total interaction cross sections (σ_I) have been widely investigated for light nuclei. This magnitude (σ_R) is defined as follows:

$$\sigma_R = \sigma_I + \sigma_{inel} \tag{3.1}$$

where σ_I is defined as the total cross section for the process of nucleon (proton and/or neutron) removal and σ_{inel} contains the contributions of electromagnetic and nuclear interactions leading to the excitation of collective nuclear modes. In this experiment, all the interactions between projectile and target leading to changes in the mass number of the projectile are measured. Therefore, all the contributions to σ_R are obtained but the fraction of inelastic excitations which not result in nucleon emission.

However, calculations on σ_{inel} show that at relativistic energies (around 900 MeV/A) the difference between these two magnitudes is only of a few percent. Hence, very often is assumed $\sigma_R \sim \sigma_I$.

The strong interest in total reaction cross sections relies in the fact that they can be used to benchmark reaction models but also because its effectiveness as a tool used to determine nuclear sizes [44]. The first measurements of σ_I with exotic nuclei started at BEVALAC [45, 46] in the mid 80s. There, the first determinations of nuclear radii for light nuclei (He,Be and Li isotopes) using σ_I were performed. The discovery of the ^{11}Li neutron halo [1] and neutron-skin structures [3], were important achievements. In the late 80s, a number of experiments were run with the SPEG spectrometer at GANIL focused on measuring σ_R [47]. Since then, almost all RI-beam facilities have incorporated programs to measure σ_R and σ_I at interemdiate and high ener-

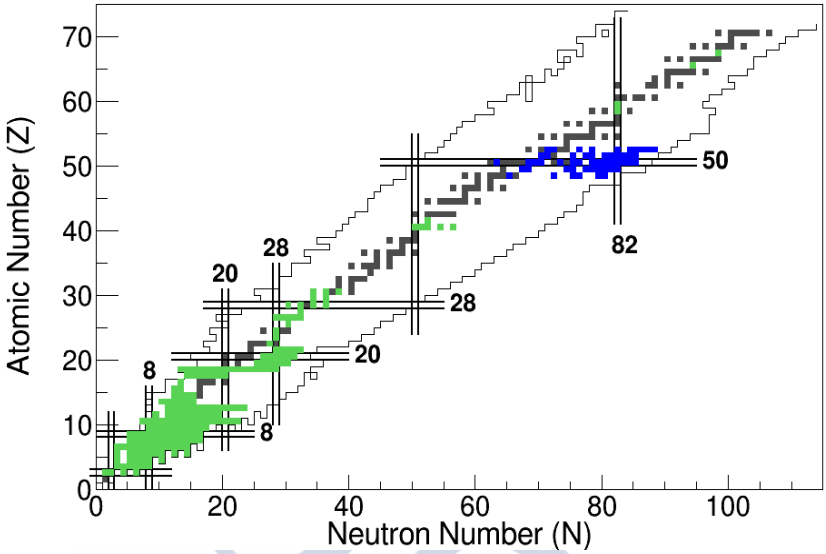

Figure 3.1: *Schematic view of the nuclear chart showing in green all the isotopes which σ_R or σ_I is measured. The blue squares represent all the isotopoes which σ_R is measured in this work.*

gies whith rather good success.

In the 90s, two important experiments were performed at GSI following the discoveries of the previous decade. Through the study of total interaction cross sections of Na isotopes [48, 49], the existence of a neutron skin in very neutron rich nuclei was confirmed. In addition a very conscientious investigation of the proton halo structure of ^{8}B was carried out [50] using the powerful FRS magnetic spectrometer.

More experiments studying the structure of ^{8}B through total interaction cross sections were performed in this decade. Almost all of the RI-beams facilities were developing their own experiments in order to explain the structure of this nuclei. Not only GSI, but GANIL [51], NSCL [52], RIKEN [53] and HIRFL [54] competed in this race to explain ^{8}B and other proton-halo candidates. The community found an agreement on the proton-halo structure of ^{8}B and the strength of σ_R and σ_I measurements was unquestionable.

With the beginning of the new millennium the conviction of the nuclear community about the exotic structures exhibited in light proton or neutron rich nuclei was complete. However, a strong effort was still being made in order to investigate and extend this knowledge all over the nuclear chart. An intensive hunt of nuclei with proton or neutron halos began, and it showed that this structure was more common than thought when discovered neutron

halos in ^{11}Be and ^{14}Be [55] or proton halos in ^{23}Al and ^{27}P [56]. It also showed that the existence of proton or neutron skins in very proton or neutron rich nuclei was also relatively common [57, 58, 59].

Figure 3.1 shows in green all the isotopes for which σ_R or σ_I is known according to our best knowledge. It can be perfectly seen that almost all the measurements were performed with light nuclei and there are almost no measurements with heavier elements. Indeed, only few measurements have been done with stable medium mass nuclei [60]. Figure 3.1 also shows in blue all the isotopes which σ_R was measured in this work. As can bee seen, we covered a large region of the chart of nuclides unexplored until today.

Along the years, two popular methods have been developed to measure total interaction cross sections, the first one is the associated γ-ray detection method [47] and the second one is the transmission method [45].

The associated γ-ray detection method is based on the assumption that every nuclear reaction is associated with a γ-ray emission. Thus, by measuring the number of γ-rays emitted normalized to the number of incident particles, one can determine the number of events which suffered an interaction with the target. However, this method is associated with high uncertainties due to the low efficiency of the γ-ray detectors. In addition, every elastic interaction of the projectile with the target is not registered, because no γ emission is associated to it.

The transmission method determines σ_R by counting the number of nuclei that survives the collision, normalized to the number of incident nuclei. However, a very clean identification of the incoming and outgoing nuclei is needed to avoid contaminants and errors in the measurement. In order to achieve this requirement, a very powerful experimental setup is needed to perform an effective separation of the reaction products.

3.2 Cross section measurement

Large isotopic chains of medium-mass neutron rich nuclei were produced in this experiment using two different reaction mechanisms, fission of ^{238}U and fragmentation of ^{132}Xe at energies around 1 GeV/A. The total reaction cross sections of the produced secondary radioactive ion beams were measured using the FRS magnetic spectrometer determining their survival probability when interacting with a 2591 mg/cm^2 Be target. For this purpose, the FRS was using as two independent magnetic spectrometer. The first part was used to identify the secondary radioactive ion beams and determine the number of incoming ions (N_2). Then, the second part is dedicated to identify the reaction products and determine the number of ions that didn't change

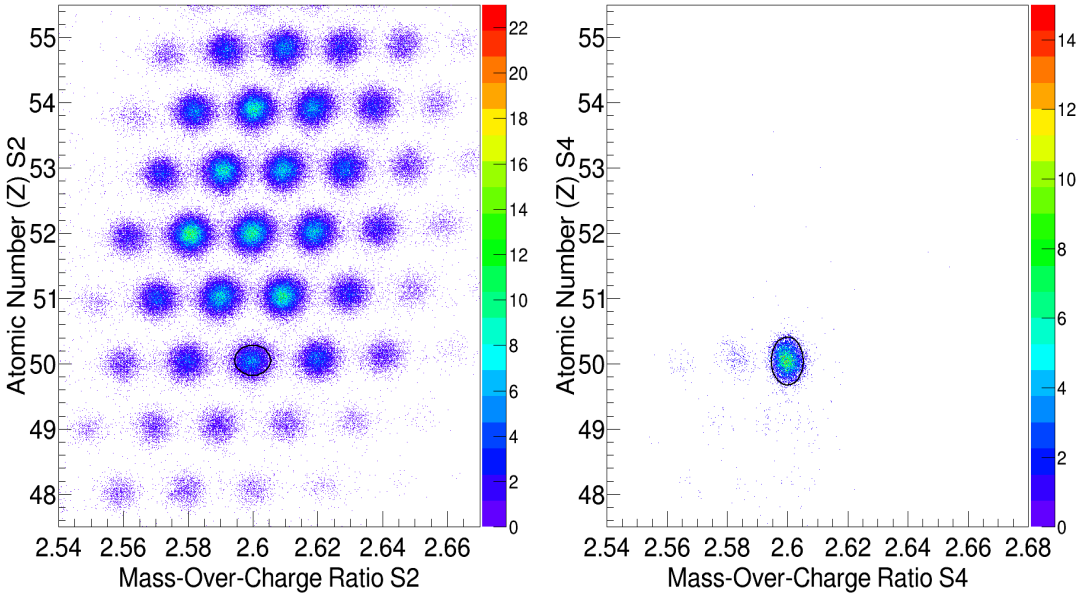

Figure 3.2: *(a) Identification matrix at the S2 focal plane.(b) Identification matrix at the final focal plan showing the fragments produced at the collision.*

their mass number after crossing the target (N_4). In addition, the survival probability of the produced secondary beams was also measured without the interaction target to account for all the secondary reactions induced by the detection equipment. The following expression will be used to determine σ_R,

$$\sigma_R = \frac{1}{N_t} ln \left(\frac{\gamma_0}{\gamma} \right) \tag{3.2}$$

where $\gamma = \frac{N_4}{N_2}$ is the ratio between the non-interacting outgoing ions (N_4) relative to that of the incoming ions (N_2). In the same way, the factor $\gamma_0 = \frac{N_4^0}{N_2^0}$ is the same ratio but for an empty-target measurement. N_t is the number of particles in the target per unit area.

The left panel of figure 3.2 shows the identification matrix of the isotopes arriving at S2, here a black ellipse is observed enclosing one of the isotopes. This contour is software-set and is used to count the number of incoming nuclei (N_2 and N_2^0). From now one, this ellipse will be called gate. The center and the semi-minus axis and semi-major axis are determined by measuring the standard deviation of the one-dimensional projection of the X (A/Q ratio) and Y (atomic number Z) axis of the identification matrix for a given isotope.

In the same way, the right panel of figure 3.2 shows the identification

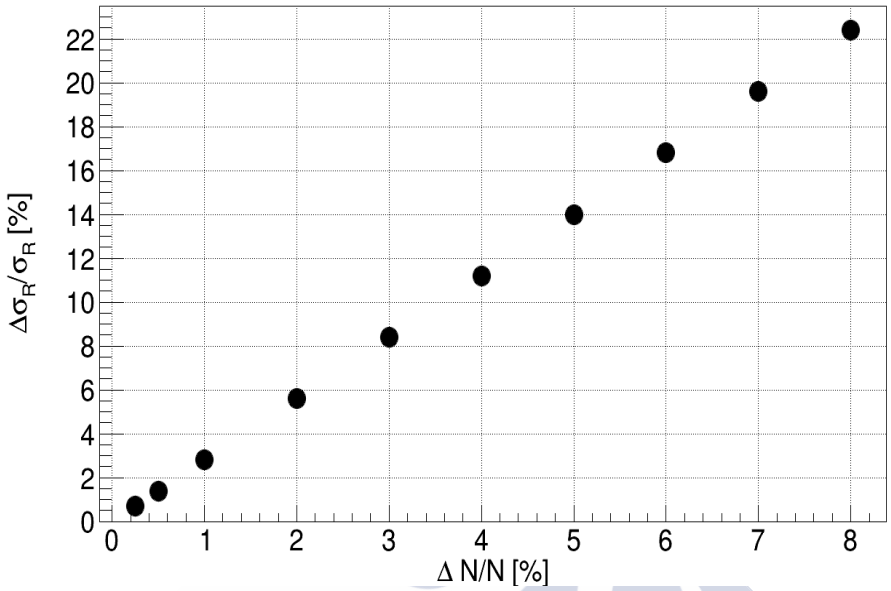

Figure 3.3: *Relative change in cross section error ($\Delta\sigma_R$) calculated with eq. 3.3 as a function of the associated error to the measured ratio $\Delta\gamma$.*

matrix of the isotopes arriving at the final focal plane conditioned to the gate placed in the identification matrix of the incoming nuclei obtained at S2. It can also be seen that another gate is set to count the number of outgoing nuclei (N_4 and N_4^0).

The total reaction cross section σ_R for a given nucleus is determined measuring the above explained ratios for more than 25 different gate sizes. Then, the average value for the cross section for all the gates showing a similar value for the measured ratios determines the final value of the total reaction cross section.

The uncertainty associated to the measurement of the total reaction cross section ($\Delta\sigma_R$) is defined as follows:

$$\Delta\sigma_R = \frac{1}{N_t}\sqrt{\left(\frac{\partial\sigma_R}{\partial\gamma_0}\right)^2 \cdot \Delta\gamma_0^2 + \left(\frac{\partial\sigma_R}{\partial\gamma}\right)^2 \cdot \Delta\gamma^2} \tag{3.3}$$

where γ_0 and γ are the measured ratios of the number of counts at S2 and S4 (N_2, N_4) with and without target and $\Delta\gamma_0$ and $\Delta\gamma$ are the associated uncertainties to these ratios. The main sources of uncertainty are the ratio fluctuations with the size of the gate, where the statistical uncertainties related to the number of counts are already included. As we perform several

variations of the size of the gate for each of the measurements, $\Delta\gamma_{(0)}$ can be evaluated by calculating the standard deviation of the ratios along all the applied gates. Then, $\Delta\sigma_R$ is calculated following eq 3.3 including all the sources of uncertainty that make γ_0 and γ to fluctuate and, therefore, to alter σ_R. In addition, the systematic error related to the applied corrections will be added quadratically when calculating the final error of the measurement.

Figure 3.3 shows the experimentally determined relative variation of σ_R ($\Delta\sigma_R/\sigma_R$) as a function of the relative changes in the measured number of counts (ΔN/N). The associated uncertainty $\Delta\sigma_R/\sigma_R$ was obtained varying the measured number of counts for the investigated ^{130}Sn nuclei in the relative percentages shows as ΔN/N in figure 3.3.

According to figure 3.3, a relative change of 1% in the measured number of counts induces a relative change in cross section of 2.8%. The required uncertainty in $\Delta N/N$ to have an error in cross section ($\Delta\sigma_R/\sigma_R$) of 1% would be 0.35%.

In the following sections we will describe de systematic corrections applied to the measurements which help to keep the ratio the most constant possible with the gate size.

3.2.1 Contamination by neighbouring nuclei

Even though the ratio N_4/N_2 should be constant with the gate size, this is not always the case. Small variations of a few percent are systematically observed for all of the investigated nuclei which in the final cross section translates into big uncertainties. Despite the identification matrix at S2 shows a very good resolution (see figure 3.2), neighbouring nuclei and charge states present in the incoming cocktail beam can overlap with our gates and alter the number of measured incoming nuclei (N_2). To evaluate this contamination, a very precise simulation was performed.

The idea is to simulate two different identification matrices. The first one contains all the nuclei in the cocktail beam except the one we are interested in. The other one contains all nuclei. All the simulated nuclei will follow mass and charge gaussian distributions for the mass and atomic number coordinates. The mean value and width of these gaussians are taken from the real identification matrices. In consequence, all the parameters used in the simulation are obtained by fitting mass-over-charge and charge experimental distributions for the given nuclei.

Figure 3.4 shows the mass-over-charge distributions of two isotopic chains (Z=50 and Z= 51) present in the incoming cocktail beam for a magnetic setting of the FRS centered in ^{130}Sn. The red solid lines represent the fit of each distribution with a function built as the sum of different gaussian

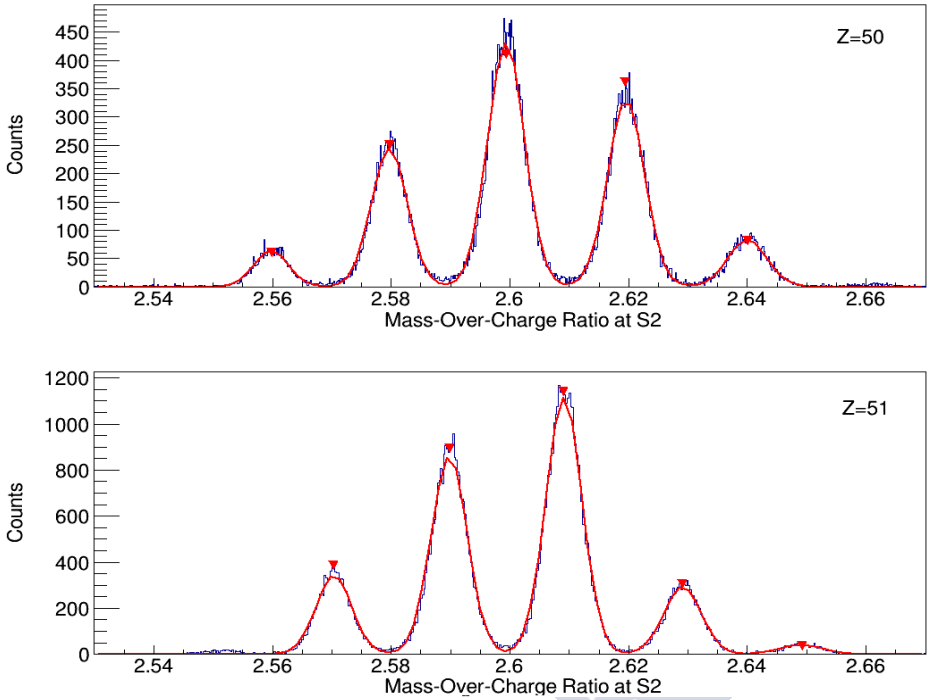

Figure 3.4: *Measured mass-over-charge ratio at the intermediate focal plane for the Z=50 (upper panel) and Z=51 (lower panel) isotopes transmitted in the magnetic setting centered in* ^{130}*Sn. The red line represent the fitting function to the measured spectrum.*

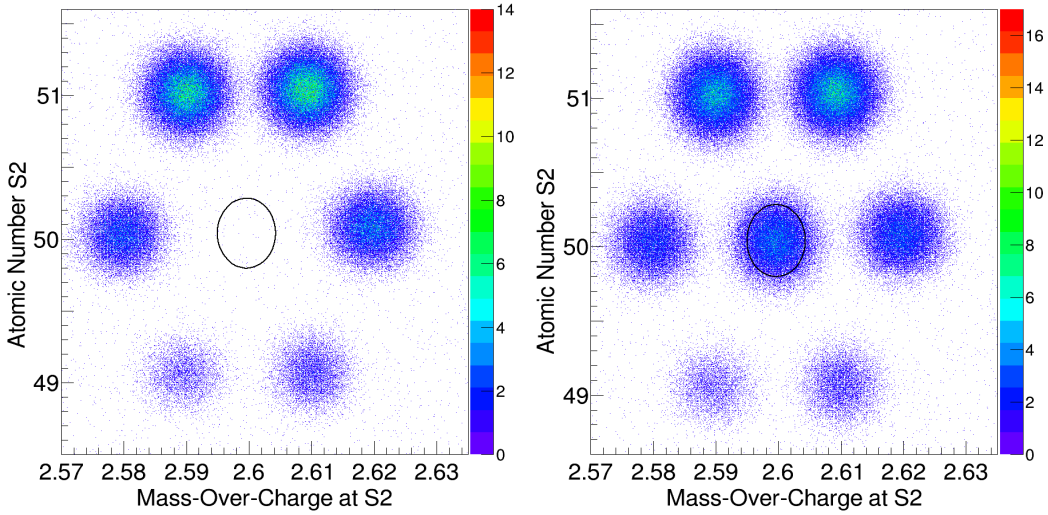

Figure 3.5: *Simulation of the identification matrix for isotopes around ^{130}Sn used to calculate the probability of having neighbours contamination. Left panel shows the simulated spectrum without ^{130}Sn and the right panel shows the simulated spectrum with ^{130}Sn. The black circles represent the software gate placed at S2 to count the number of incoming ^{130}S ions.*

functions. The parameters of each gaussian function (standard deviation and mean value) are used as inputs in the simulation.

Once all the parameters are determined, we use a Monte-Carlo technique to simulate the identification matrix of the incoming cocktail beam. The relative probabilities for the production of each nucleus are also included in the simulation. As an example, to estimate the contaminants in the software gate used to identify the ^{130}Sn, we simulate all neighbouring nuclei (^{127}In, ^{128}In, ^{129}Sn, ^{131}Sn, ^{132}Sb and ^{133}Sb). Then we randomly generate events following the corresponding mass-over-charge and atomic number gaussian distributions.

Figure 3.5 shows an example of the simulation of the identification matrix corresponding to the FRS setting centered in ^{130}Sn. The gates placed in both panels correspond to the one we use to determine the production of ^{130}Sn. The ratio between the number of simulated events falling into the gates will provide the correction factor we need to apply. The same procedure is applied to gates on the same nucleus but of different size.

Figure 3.6 shows the number of counts as a function of the gate size selected at the intermediate focal plane. The blue line represents the number of counts measured without correction and the red line the corrected number

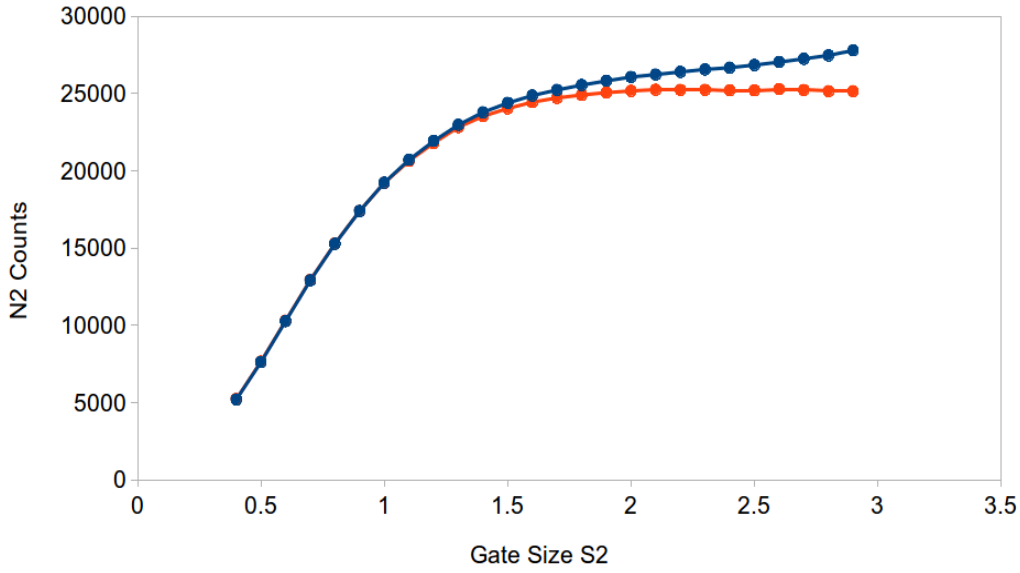

Figure 3.6: *Number of counts at the intermediate focal plane. The blue line shows the non-corrected number of counts. The red line shows the number of counts once the correction factor due to neighbours contamination is applied.*

of counts when the contaminants are subtracted. As it is clear, the correction begins to be important for the largest gates. The size of the gate is indicated as a multiplicative factor of the experimental standard deviation of the mass-over-charge and atomic number distributions, in this case, we are showing the yields produced at S2 for the ^{130}Sn and the biggest correction factor is 10%.

The uncertainty associated with this correction is related to the parameters used in the simulation which are given by the fitting functions showed in figure 3.4. The associated uncertainty to the mean value of the mass-over-charge distribution is very low, less than 0.1%, and the error associated to the standard deviation is around ∼2%. The uncertainty induced in the final value of σ_R by this correction is less than 1%.

3.2.2 Atomic charge states

Fragments traveling along the FRS can pick-up or strip-off some electrons due to interaction with matter, typically targets and detectors, leading to changes in its atomic charge. This means that some of the reaction products can be missidentified causing losses in the number of measured nuclei at the end of the FRS. We have used the AMADEUS [61] code to estimate the

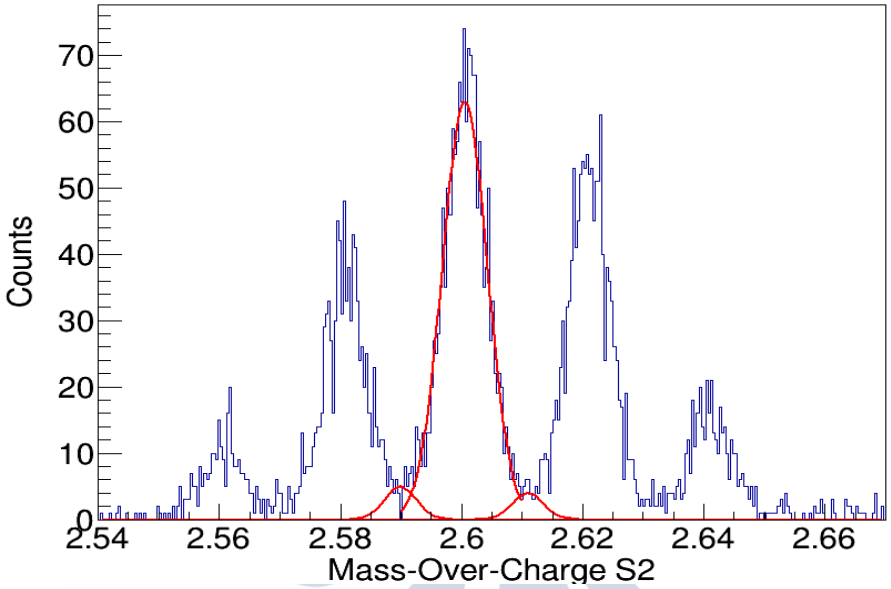

Figure 3.7: *AoQ values for the Z=50 isotopic chain, showing only trigger1 events. The gaussian distributions present ass red-solid lines represent an estimation of the charge-states contamination from the (A-3(2),Z) isotopes.*

probability of producing charge states when the fragments interact with the different layers of matter placed along the beam line (table 11 in appendix C shows all the layers of matter along the beam line used in this experiment).

In addition, those fragments that picked-up an electron in the first part of the FRS will contribute to a miss-identification in the S2 identification matrix. In particular, (A-3, Z) residues with an hydrogen-like charge state (Q=Z-1) have a similar magnetic rigidity as the fully stripped (A, Z) nuclei, then a small percentage of this will fall into our gates and will be identified as (A ,Z) events in S2. Moreover, the amount of miss-identified counts due to charge states contamination depends strongly on the size of the gate used to count the number of events. The probability of loosing the electron in the second part of the FRS is very high for this events, this will change their magnetic rigidity to the original (A-3 ,Z) nuclei and thus they will not be transmitted to final focal plane in S4.

Figure 3.7 shows the mass-over-charge ratio for trigger #1 events of the Z=50 isotopic chain transmitted to the intermediate focal plane in a magnetic setting centered in ^{130}Sn. We selected events identified as trigger #1 because these are the events that are not going to reach the final focal plane. The small gaussian distributions between the large peaks show an estimation

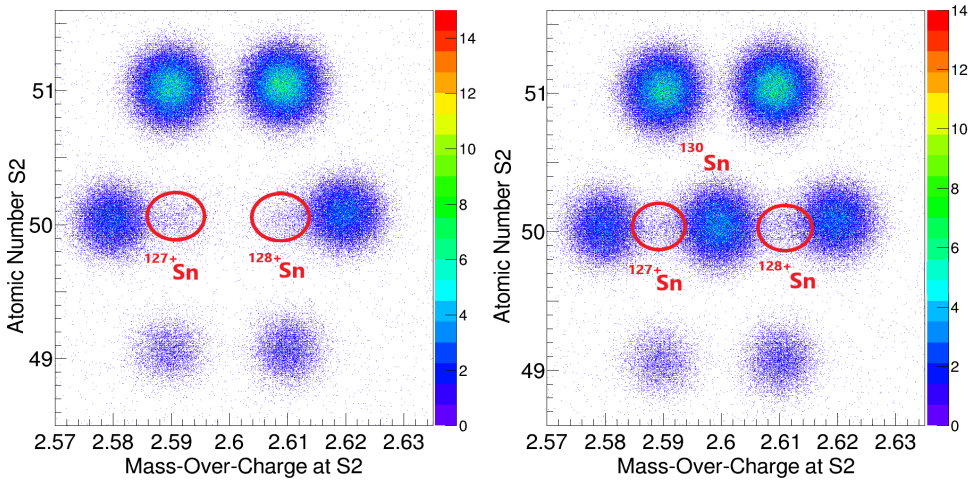

Figure 3.8: *Same simulation as in figure 3.5 but with charge states probabilities introduced.*

of the charge states of the (A-3, Z) ions which present a similar magnetic rigidity as that of the (A, Z) isotope. As they will loose their charge state in the second half of the spectrometer, they are not transmitted to the final focal plane and thus are identified as trigger #1. This effect produces an overestimation of the number of counts measured at S2.

The probability of producing charge states was calculated with the GLOBAL code [62] which is implemented in the simulation described in the previous section. In addition, as a double-check, we determine from the experimental identification matrix the amount of existing charge states. By determining the number of events under the two small gaussian distributions showed in figure 3.7 we can determine the ratio between this number and the number of (A,Z) events, estimating the existing percentage of atomic charge states with respect to the investigated nucleus. Typically, the experimentally measured atomic charge state contribution coincides rather well with the probability calculated with GLOBAL. Nevertheless, if the calculated contribution is smaller than the experimental estimation, we prioritize the experimental one.

Figure 3.8 shows the result of the simulation described in the previous section but including the probability of having atomic charge states. The red circles are drawn to highlight the contribution of the simulated charge states. The correction factor is determined in the same way as explained in the previous section, the ratio between the number of events overlapping with the gate in the left panel of figure 3.8 and the same number determined in the right panel of figure 3.8. As this overlap depends on the size of the

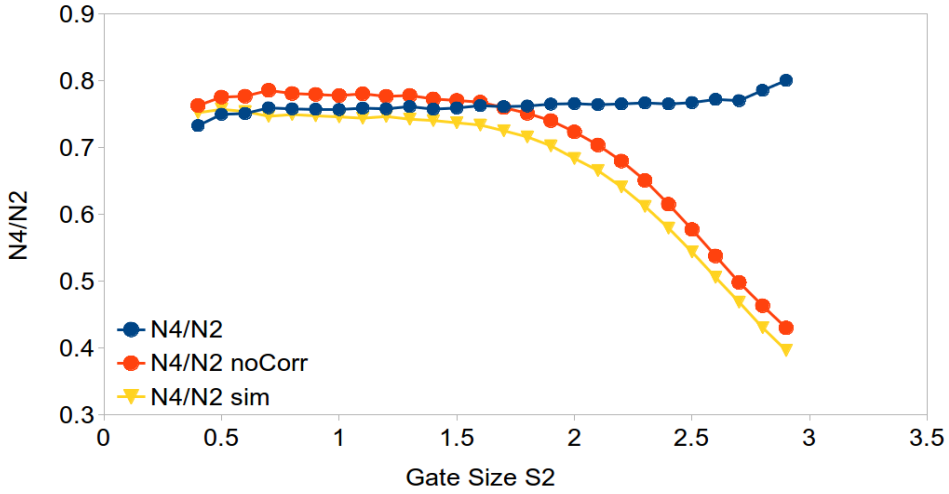

Figure 3.9: *Ratio between number of counts in S4 and S2 as a function of the size of the gate placed at S2. The experimental ratio N4/N2 obtained is represesented by the red dots. The yellow triangles are the ratio obtained with the simulation. The blue dots are the experimental corrected N4/N2 ratio.*

gate, we run the simulation over different gates with different sizes to obtain a correction factor for each gate used to measure the number of counts in S2.

Figure 3.9 show the ratio N_4/N_2 between the counts in S4 (N_4) and S2 (N_2) for ^{119}Sn as a function of the size of the gate used to count the number of incident ions. The red dots represent the measured N_4/N_2 ratio, decreasing for the bigger gates as a consequence of the contamination of neighbouring nuclei and atomic charge states. The blue dots represent the ratio N_4/N_2 corrected by the correction factors obtained from the simulation previously described. The yellow triangles represent the simulated ratio N_4/N_2.

The contribution of the charge-states contaminants is in average below 3%. The systematic error associated to this contribution is related with the percentage of charge states that we introduce in the simulation. An extensive discussion on the comparison between the predictions obtained with Global and experimental results can be found in [62]. Here, the charge states yields are generally predicted to be better than a factor of two. Due to this, the uncertainty introduced by this correction in the final value of σ_R is $\sim$1%.

3.2.3 Dead time correction

The measured yields must be corrected by the dead time of the data acquisition system (DAQ). In each event, we have information about the

number of accepted and free (total) triggers. The number of free triggers N_{free} is the number of events arriving at the plastic scintillators which trigger the data acquisition system (SC2 and SC4). The number of accepted triggers N_{acc} is the number of events that the acquisition system admits. The ratio between these two magnitudes represents the dead time correction factor for the yields.

In this experiment we have two different triggers (Trigger #1 and Trigger #3) described in section 2.5. Trigger #1 corresponds to ions that arrived at S2 but did not arrived at S4 and Trigger #3 corresponds to the ions arriving at the end of the spectrometer. Then, we have two different dead time correction factors. The number of free triggers, N^1_{free} and N^3_{free} are given by the plastic scintillators SC2 and SC4. The number of accepted triggers N^1_{acc} and N^3_{acc} are given by the DAQ system. Both correction factors can be expressed as:

$$C^1_{dead} = \frac{N^1_{free}/2^{RF}}{N^1_{acc}} \; ; \; C^3_{dead} = \frac{N^3_{free}}{N^3_{acc}} \tag{3.4}$$

where 2^{RF} is the reduction factor, which takes values between 2 and 8 for the magnetic settings studied in this work. The corrected number of particles counted at the intermediate (N_2) and final (N_4) focal planes are the following:

$$N_2 = N^1_2 \cdot 2^{RF} \cdot C^1_{dead} + N^3_2 \cdot C^3_{dead} \tag{3.5}$$

$$N_4 = N^3_4 \cdot C^3_{dead} \tag{3.6}$$

where N^1_2 and N^3_2 denotes the number of ions with Trigger #1 and Trigger #3 at the intermediate focal plane. On the other hand, at the final focal plane we only have ions with Trigger #3 N^4_3.

A table showing the dead time correction factors used in this work can be found in appendix. The uncertainty introduced by this correction is about 1%.

3.2.4 Ion-optical transmission

The FRS has a limited acceptance in momentum (±1.5%) and angle (±15 mrad). The transmission of a given nucleus is defined by these two limits and the position of the ion at the intermediate and final focal planes. In this experiment, we used two different reaction mechanisms in order to produce large isotopic chains of medium-mass nuclei, fragments produced by fragmentation or fission present different angular and position distributions so the transmission treatment is different.

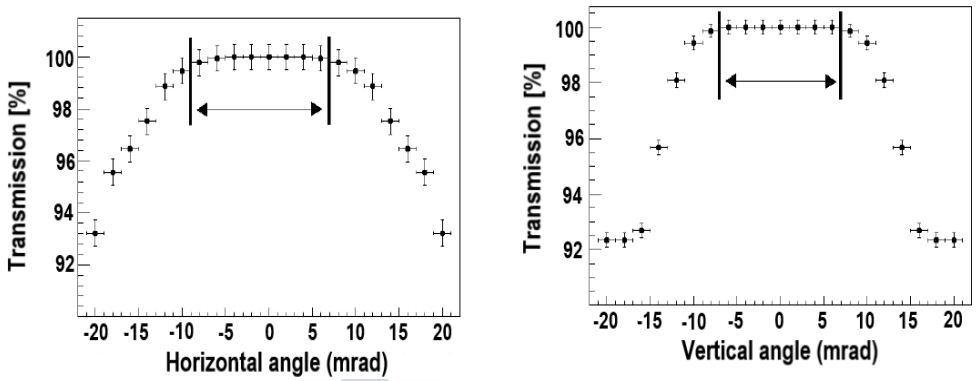

Figure 3.10: *Left pannel shows the transmission as a function of the horizontal (α_x) angle. Right panel shows the transmission as a function of the vertical angle (α_y). The black bars shows the angular range within the transmission calculated with MOCADI is 100%*

Nuclei produced by fragmentation show very narrow angular distributions always within the limits of the angular acceptance. Therefore, the angular transmission efficiency is 100% for these settings. However, those neutron-rich isotopes produced by fission of ^{238}U have a broader angular distribution with a limited transmission. In order to correct those losses and to have a more accurate counting of the number of ions arriving at the final focal plane, we used the MOCADI code [63] to study the transmission between the intermediate and the final focal planes.

We studied the angles at which the transmission between S2 and S4 was maximized by simulating the trajectories of the ions through the second part of the spectrometer. Figure 3.10 shows that those ions with angles between -8 mrad $< \alpha_x <$ +8 mrad and -8 mrad $< \alpha_y <$ +8 mrad, where α_x denotes the horizontal angle and α_y the vertical angle, experience trajectories with 100% transmission along the second part of the FRS. Due to this, we only select ions within this angular range to determine the total reaction cross sections. Using this condition we loose statistics but on the other hand we do not need any transmission correction. The associated uncertainty to this calculation was studied in Ref. [64], finding that the adopted criteria on the reduction of the angular aperture reduced the uncertainty associated to the transmission correction to a 5%.

3.2.5 Time of flight losses

Events lost because their time of flight (ToF) was not registered are taken into account. Among all the events that triggered the acquisition, there is a small percentage of events that are identified as trigger #3, meaning that those ions arrived to the scintillator placed at S4 (SC4), but their time signal was incorrectly registered. This means that the identification in S4 is not possible and therefore are effectively lost. For target-in runs this percentage is below 1% of the total number of events. However, for empty-target runs, this percentage is systematically bigger, typically about 2-3%.

As a consequence, a systematic unbalance in the relative percentage of trigger #3 events between the runs with and without target is detected and must be corrected. The magnitude of this correction is mentioned above.

3.2.6 Target thickness

The thickness of the target is directly related to the total reaction cross section through the inclusion in equation 3.2 of the number of target nuclei per unit area (N_t). This magnitude is defined as,

$$N_t = \frac{\rho_m \cdot N_{av}}{M} \tag{3.7}$$

where ρ_m is the target thickness in g/cm^2, N_{av} is the Avogadro constant and M is the beryllium molar mass in g/mol. The target thickness can be determined by measuring the difference in magnetic rigidity of an ion when traversing the target. The change in Bρ is directly related with its energy loss and, hence, one can calculate with different codes like LISE [65] or AMADEUS [61] , the thickness needed to reproduce the observed experimental variation in magnetic rigidity.

With our experimental setup, the magnetic rigitidy of the nuclei before and after the target can be obtained from the two sections of the FRS. However, in the beam line there are several layers of matter that also produce small variations to the magnetic rigidity of an ion. Therefore, in order to obtain just the variation inside the target, we use the combination of settings with and without target because there is no difference in the amount of matter placed in the beam line between these settings but the target.

The difference in $\Delta B\rho$ = $B\rho_{S2}$ - $B\rho_{S4}$ between a magnetic setting with and without the target, is precisely the variation due to the effect of the target. Using AMADEUS we can calculate the thickness of the target for such a variation in Bρ by just simulating an ion going through a layer of matter.

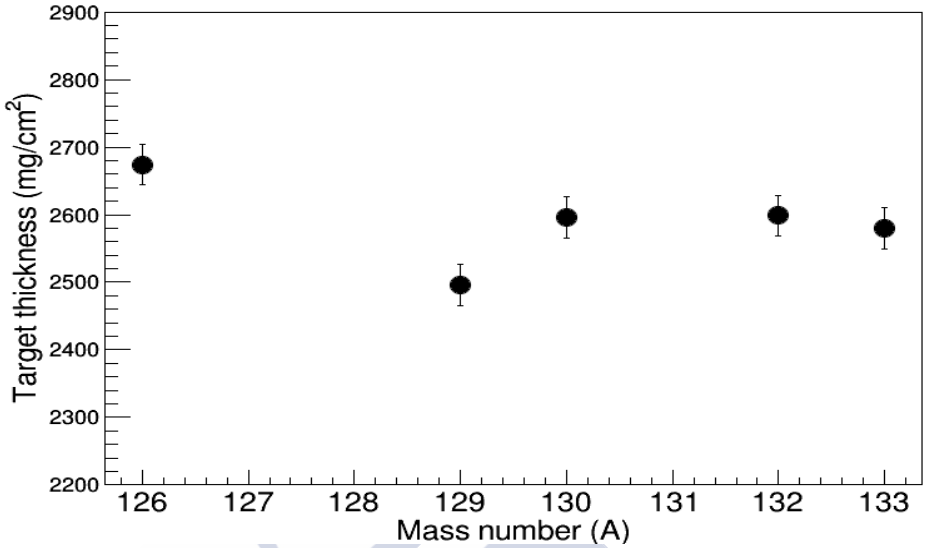

Figure 3.11: *Measured target thickness (mg/cm^2) for five different tin isotopes transmitted in four different magnetic settings of the FRS. The magnetic settings investigated were those centered in ^{126}Sn, ^{130}Sn, ^{132}Sn and ^{136}Sn.*

For this purpose, we use several ions in different magnetic settings that are fully transmitted along the spectrometer. Then, we determine for each of these ions their Bρ variations and thus, we can obtain the target thickness. Figure 3.11 shows the obtained target thickness for different ions following this procedure. Tin isotopes from four different magnetic setting of the FRS were investigated providing an average target thickness of 2589 ± 80 mg/cm^2. A good agreement is found with the results obtained by the target laboratory at GSI, where a value of 2591 ± 90 mg/cm^2 was measured.

The total reaction cross sections measured in this work were determined using the measurement obtained from the target laboratory. The associated uncertainty to the target thickness measurement of $\sim$90 mg/cm^2 is translated in an uncertainty in the total reaction cross section of 3.5%. The magnitude of this uncertainty is detailed for each measured nuclei in tables 1, 2 and 3 found in appendix A.

3.3 Results

Figure 3.12 shows the total reaction cross sections measured in this work as a function of the neutron number of the projectile. An overall of 50 measurements were obtained for 5 different elements ranging from cadmium

(Z=48) to telurum (Z=52). The measured cross sections for nuclei produced by fission of ^{238}U are represented as solid dots and the cross sections for isotopes produced by fragmentation of ^{132}Xe are represented as triangles.

Even though with our experimental setup we were able to produce elements with lower and higher atomic numbers than the ones shown in figure 3.12, it was not possible to determine total reaction cross sections for all of them. First of all, performing this measurements with the lowest possible uncertainty requires several corrections that one has to apply individually to each of the isotopes. Furthermore, the magnetic settings are tunned to maximize the transmission of a certain Z=50 isotope. This makes that as far as we move in Z from Z=50, the transmission decreases proportionally to this distance. Finally, to keep low uncertainties, high production rates are needed. Ions produced by fission present the maximum production rate for elements around Z=52 and the production of ions produced by fragmentation decreases with lower atomic numbers. The error in these measurements is below 10% for all the investigated ions. Despite of the several corrections applied to the number of counts measured at both focal planes, the instability in both ratios (N4/N2 with and without target) presented deviations of 1-3%, according to figure 3.3 this effect induces an error of 3-6% in σ_R. In addition, the uncertainty in the target thickness and transmission also induced large uncertainties in σ_R.

Tables 1, 2 and 3 found in appendix A show all the results obtained in this work and the different contributions to the total uncertainty ($\Delta\sigma_R^{Tot}$) of the measurement. Here, $\Delta\sigma_R$ is the statistical error calculated following equation 4.2 and Δ_{Sim}, Δ_{Tgt}, Δ_{Tr}, Δ_{ToF} and Δ_{Dt} are the systematic errors associated to the simulation (including neighbours and charge states), target, transmission, time of flight and dead time corrections. All of them are quadratically added in order to calculate the final uncertainty of the measurement $\Delta\sigma_R^{Tot}$.

Figure 3.13 shows the measured total reaction cross sections as a function of the neutron-number of the projectile in a single chart. Two different trends on the evolution of the total reaction cross section with the neutron number can be observed. In the case of tin isotopes, those with neutron number N$\leq$79 show a smooth increase of the cross section, according to the expected evolution with $A^{1/3}$ which is represented as a dashed line in figure 3.13. However, above N=79, a stepper increase of the total reaction cross section is observed. This effect is independent of the reaction mechanism. It can be seen in figure 3.12 that ^{128}Sn and ^{129}Sn are produced by fission and follow the common trend for less-neutron rich isotopes.

However, the deviation from the expected evolution with $A^{1/3}$ starts at different neutron numbers for the different elements. Figure 3.13 shows how the beginning of the deviation starts at N$\sim$76 for Z=48, N$\sim$77 for Z=49,

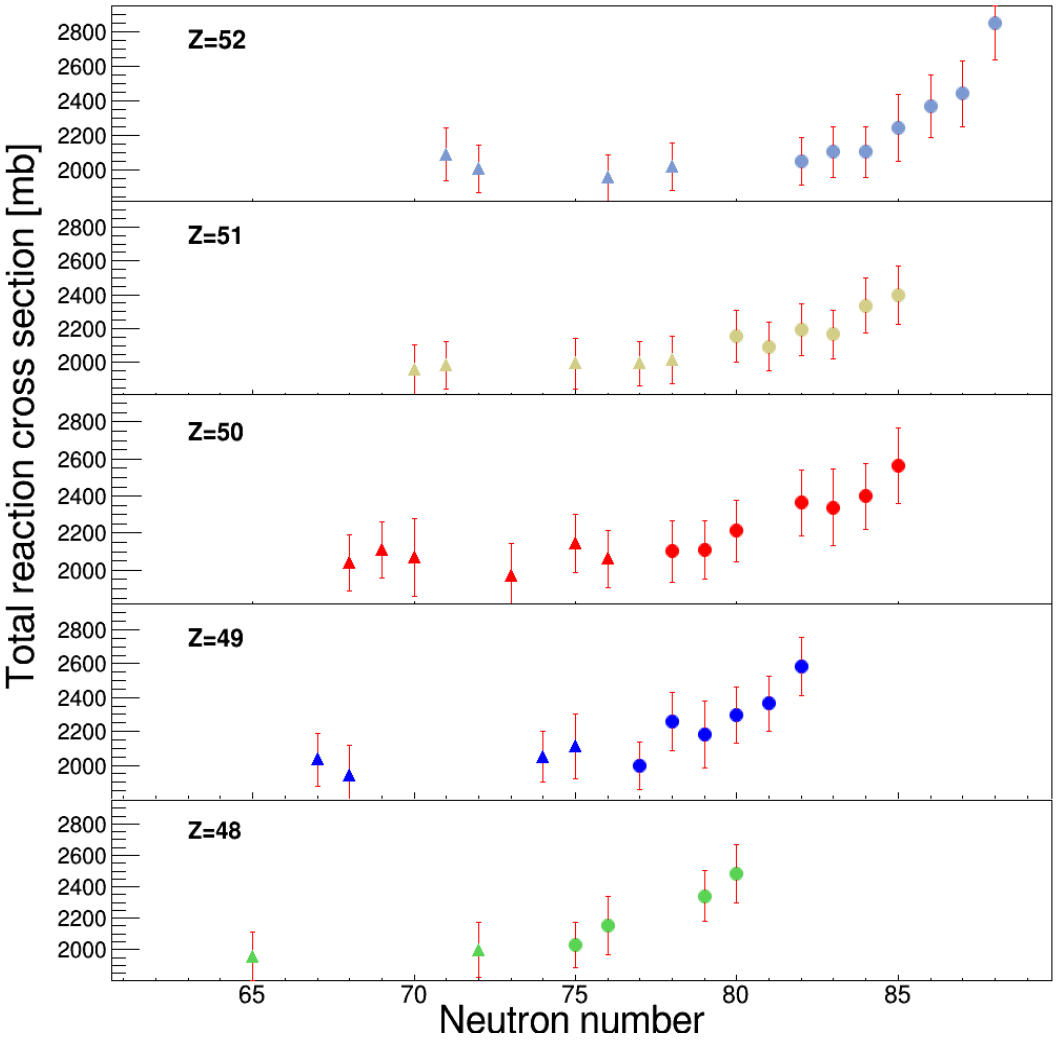

Figure 3.12: *Total reaction cross sections vs neutron number of the projectile measured in this work. Isotopes produced by fission of* ^{238}U *are represented as solid dots and isotopes produced by fragmentation of* ^{132}Xe *are represented as triangles.*

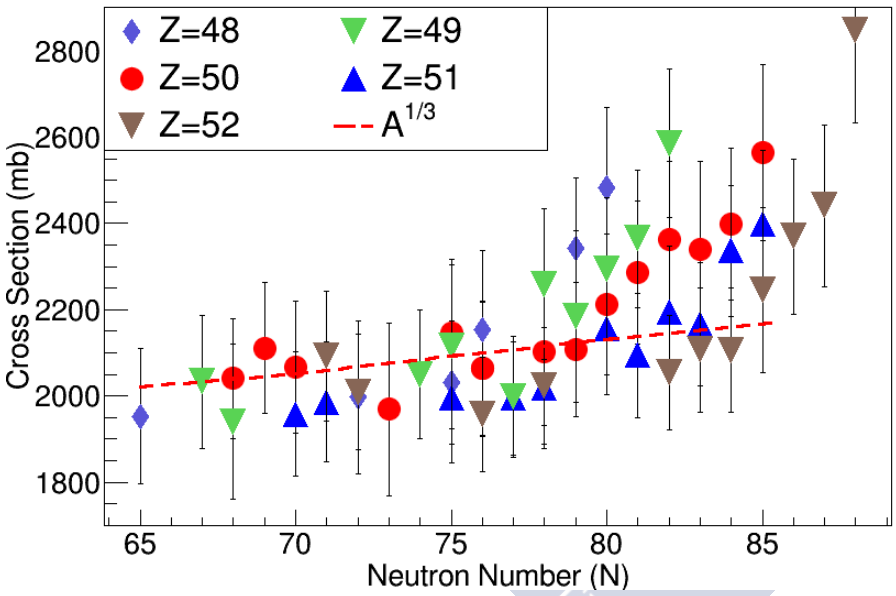

Figure 3.13: *Total reaction cross section as a function of the neutron number of the projectile. The five different isotopic chains measured in this experiment are showed in this figure. The dashed red line represents the expected evolution with $A^{1/3}$ for tin isotopes with the r_0 parameter tuned to reproduce the results.*

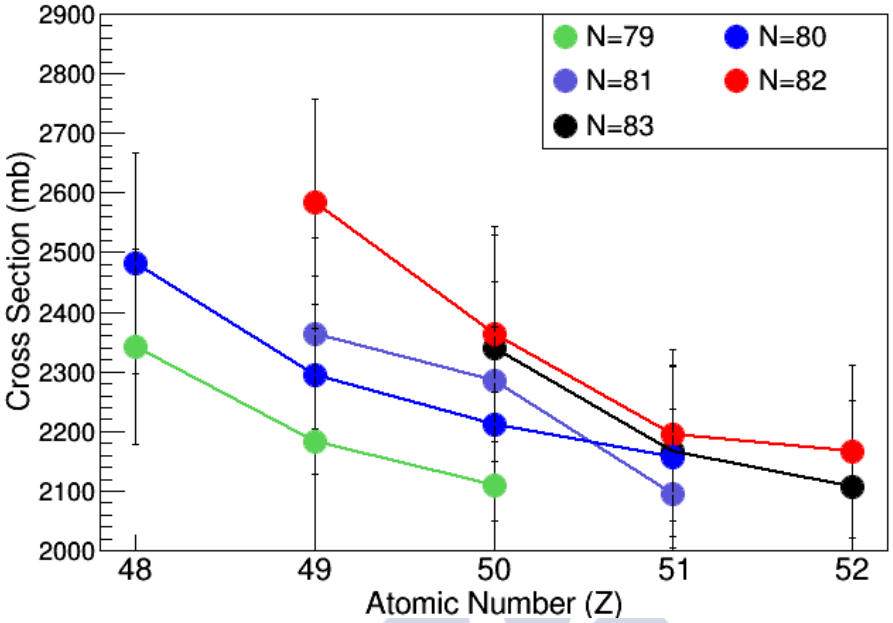

Figure 3.14: *Total reaction cross section as a function of the atomic number of the projectile. The evolution with Z of five different isotone chains is showed.*

N∼79 for Z=50, N∼81 for Z=51 and N∼83 for Z=52. This suggests that the evolution of the total reaction cross section in this region depends on the neutron-proton asymmetry of the nucleus.

Moreover, figure 3.13 shows large differences in cross section for isotones with neutron number N >78. Surprisingly, along the different measured isotonic chains in this region, those with lower atomic numbers present larger cross sections. This effect can be observed in figure3.14 where 5 isotonic chains with neutron numbers from N=79-83 are shown.

This effect shows that nuclei that are bigger in mass show smaller cross sections. For example, the total reaction cross section for ^{131}In is larger than the total reaction cross section for ^{132}Sn. This effect can be interpreted as an evidence of the growth of neutron skins in this region. The neutron skin grows with the neutron-proton asymmetry of the nucleus and is related with large neutron density distributions which increase the overall size of the nucleus. As a matter of fact, the neutron-proton asymmetry is larger for ^{131}In than for ^{132}Sn. This means that a thicker neutron skin is expected for ^{131}In which could increase the size of the nucleus.

Figure 3.15 shows the measured total reaction cross sections as a function of the neutron excess of the measured nuclei. As can be seen, our measure-

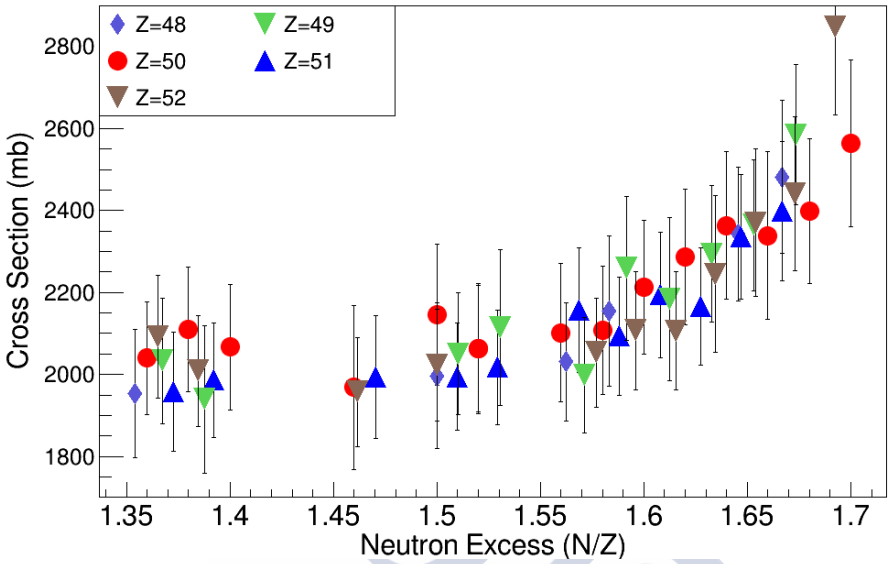

Figure 3.15: *Total reaction cross section as a function of the neutron excess of the projectile. The neutron excess is defined as (N-Z)/Z where N is the neutron number and Z is the atomic number A strong correlation is observed.*

ments cover a rather large range in neutron excess. In this case, we also observe the two evolution patterns of the cross section although the behavior seems more universal. Indeed, the change in the tendency appears for all elements for a similar value of the neutron excess.

Figure3.15 shows that the evolution of the cross section for isotopes with N/Z>1.60 increases with the neutron excess and for isotopes with N/Z<1.60 follows the expected evolution with $A^{1/3}$.

3.4 Model calculations

Glauber calculations, as the one described in section 3.1, were performed in order to understand the observed deviation of the total reaction cross section with the expected evolution with $A^{1/3}$. Equation 1.2 describes the non-interacting probability of the projectile through the target as a function of the nucleon density distributions of both projectile and target. These density functions have been studied for tin isotopes in some works [66] finding hints of the presence of a neutron skin [67, 68]. However, the available data does not go further than ^{124}Sn.

Recently *W. Horiuchi et al* [69] using HF+BCS calculations showed that

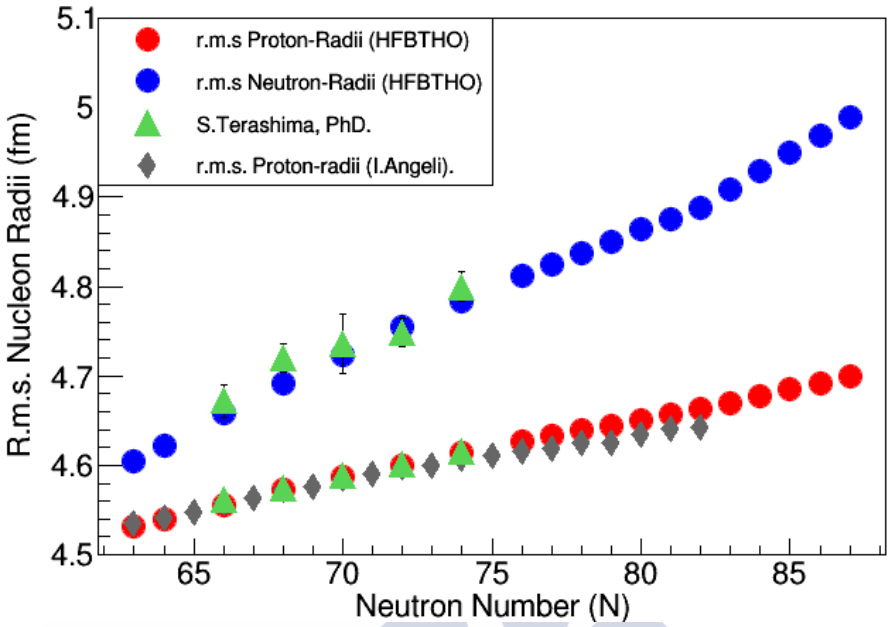

Figure 3.16: *R.M.S. Neutron and proton radii obtained with Hartree-Fock-Bogoliuvob calculations. Comparison with S. Terashima calculations are represented as green triangles.*

the difference between the r.m.s. neutron and proton radii increases as increasing the neutron number. The neutron skin thickness (S_{thick}) is precisely defined as the difference between this two magnitudes:

$$S_{thick}(N,Z) = r_n(N,Z) - r_p(N,Z) \tag{3.8}$$

Furthermore, it was also described in [70] the possibility of determining the nucleon density distributions using Hartree-Fock calculations as a way of having a more realistic description of the surface of the nucleus. Then, one can use in equation 1.2 the calculated density distribution instead of the standard parametrizations described in [21].

We took this idea in order to have the most accurate Glauber calculations and compare with them the results obtained in this work. A parametrization of the nucleon-density distributions obtained with HF calculations was included in the code based on the Glauber's theory we used to calculate total reaction cross sections [21, 71]. As a validation of our HF calculations, the r.m.s. neutron and proton radii were compared with experimental results.

Figure 3.16 shows the results obtained using Hartree-Fock-Bogoliuvob calculations with the Skyrme Sly5 interaction. Here, the r.m.s. neutron and

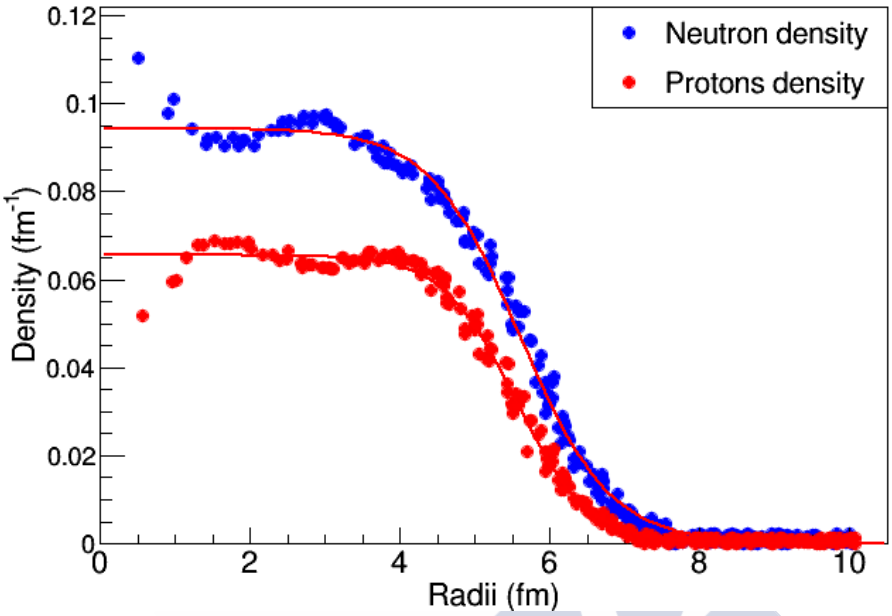

Figure 3.17: *Neutron and proton density distributions ($\rho_{n(p)}$) obtained with Hartree-Fock-Bogoliuvob calculations for ^{132}Sn. The calculated distributions are fitted to a Wood-Saxon function represented by the red lines.*

proton radii is shown as a function of the neutron number of the projectile for the Z=50 isotopic chain. A comparison between our calculations and the results obtained by *S. Terashima* in Ref.[72] is shown. Here, the largest deviation is found to be of a 0.60% for the r.m.s neutron radii of ^{118}Sn.

In addition, the r.m.s nuclear charge radii $\langle r^2 \rangle_{ch}^{1/2}$ has been measured for many ions typically by electron elastic scattering experiments. A full set of measurements can be found in [73]. We can compare our results for the r.m.s proton radii $\langle r^2 \rangle_{pp}^{1/2}$ with the r.m.s proton radii that can be obtained from the experimental measurements of r.m.s nuclear charge radii. The mean square nuclear charge radii $\langle r^2 \rangle_{ch}$ is related with the mean square proton radii $\langle r^2 \rangle_{pp}$ following the next expression,

$$\langle r^2 \rangle_{ch} = \langle r^2 \rangle_{pp} + \langle (r_{ch}^{proton})^2 \rangle + \frac{N}{Z} \cdot \langle (r_{ch}^{neutron})^2 \rangle \tag{3.9}$$

where $\langle (r_{ch}^{proton})^2 \rangle$ and $\langle (r_{ch}^{neutron})^2 \rangle$ are the mean square proton and neutron charge distributions [74, 75]. The r.m.s value for the proton charge distribution is 0.895 $\pm$ 0.018 fm and the m.s radius of the neutron itself is -0.112 $\pm$ 0.003 fm^2.

Figure 3.16 also shows a good agreement between our calculations and the results obtained subtracting the proton radii from the r.m.s nuclear charge radii measurements. The biggest difference between these calculations is 0.44% for ^{132}Sn.

It can be seen how the neutron skin (S_n) increases with the neutron number and a sudden increase in the r.m.s. neutron radii is observed when crossing the N=82 shell. This behavior was also observed in [69]. Figure 3.16 shows the comparison with other results in order to validate ours. As the result seems to be reasonable, we will introduce a parametrization of the neutron and proton density distribution obtained with the Hartree-Fock-Bogoliuvob calculations in the Glauber code to perform the calculation of T(r) with a more realistic description of the nucleus.

Figure 3.17 shows the obtained nucleon density distributions with Hartree-Fock-Bogoliuvob calculations for ^{132}Sn. To use these distributions as inputs in equation 1.2 we fitted them with a Wood-Saxon function:

$$\rho(r) = \rho_0 \{1 + exp\,[(r - R)/d]\} \tag{3.10}$$

where ρ_0, R and d are left as free parameters in the fit. The results of the fit are used in the code [21] when performing the calculation for each nucleus.

However, equation 1.2 not only depends on the nucleon radial density distributions but also on σ_{pp} and σ_{np} cross sections. The most recent parametrization of the proton-proton and neutron-to-neutron elementary cross sections is described in [76]. It is reasonable then, to use this parametrization to obtain a more realistic calculation.

We have described in section 3.1 that the difference between total σ_R and interaction σ_I cross sections is due to initial state interactions between the two reacting nuclei. These interactions are mostly governed by Coulomb and nuclear induced collective excitations. The most probable excitations are the Giant Dipole Resonance (GDR) and Giant Quadrupole Resonance (GQR). Both mechanisms lead to the evaporation of nucleons as a consequence of the excitation energy induced in the system and contribute to reduce the measured interaction probability. Glauber calculations determine the cross section for the change of proton and/or neutron number in the incident nucleus due to interaction with the target that lead to the fragmentation of the projectile and, therefore, they do not take into account the possibility of excitate collective nuclear modes. We calculated separately these contributions and added them to the final of calculated value of σ_R. In addition, Glauber calculations include in σ_R the fragmentation of the target as a result of the interaction, this contribution is not measured in this experiment so it is not

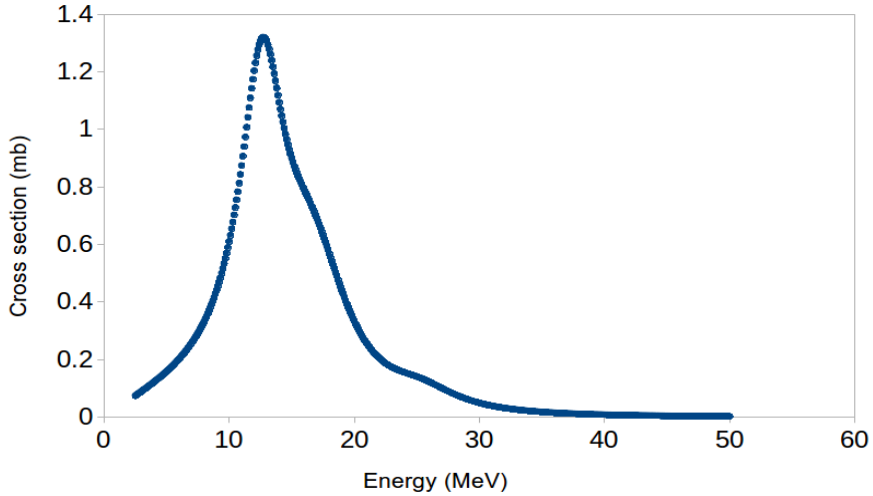

Figure 3.18: *Coulomb excitation contribution for ^{132}Sn. The cross section contribution per MeV is shown as a function of the coulomb excitation energy*

considered in the calculation.

3.4.1 Coulomb induced excitations

Heavy ion collisions at relativistic energies are expected to have large probabilities for the electromagnetic excitation of collective nuclear modes such as giant resonances (GDR) [77]. It was observed that the electromagnetic excitation above the neutron separation energy contributes to the fragmentation process in this regime [78]. Although this magnitude depends on the number of protons of the target, it is assumed to be non negligible for a Beryllium target as the one used in this work.

The majority of the experiments focused on the investigation of these excitations use targets with high atomic numbers in order to have larger cross sections [79]. As a matter of fact, no experimental data was found in literature for light targets like beryllium. This is the reason why we used model calculations based on Ref.[80] to estimate this contribution.

Figure 3.18 shows the calculated cross section as a function of the induced excitation energy for ^{132}Sn. The overall cross section contribution is found to be $\sim$12 mb. Almost the 90% of the cross section is above the neutron separation energy for ^{132}Sn ($\sim$7.4 MeV) which means that there is a contribution of $\sim$11mb of Coulomb excited events that contribute to our cross section. The calculated values for tin isotopes are shown in figure 3.19.

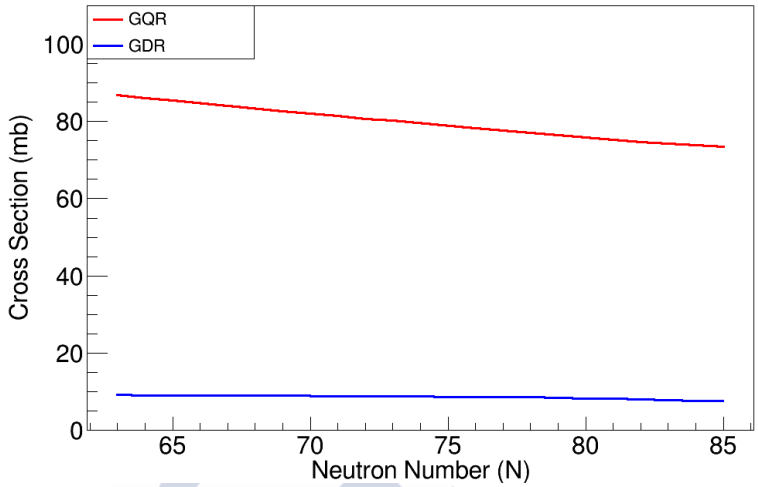

Figure 3.19: *Nuclear (GQR) and Coulomb (GDR) excitations calculated by professor Carlos A. Bertulani on tin isotopes at 1GeV/A*

3.4.2 Nuclear excitations

The excitation of the giant quadrupole resonance (GQR), a collective surface oscillation of nucleons, isovector or isoscalar depending if protons and neutrons are oscillating opposite or in phase to each other was observed with considerable cross section in [77]. A ∼100 mb nuclear cross section contribution was measured in this work for ^{136}Xe at 0.7 GeV/A with high uncertainties.

Calculations performed by *A. Bertulani* [81] are shown in figure 3.19. Here both the coulomb excitations (blue line) and the nuclear excitations (red line) are shown as a function of the neutron number of the Z=50 isotopes. It was found that the largest source of nuclear excitation is the giant quadrupole resonance (GQR) which would contribute with ∼ 80 mb to the total reaction cross section. In addition, very recent experimental preliminary results on ^{124}Sn and ^{128}Sn at 0.5 GeV/A from Ref.[82] measured the cross section from the giant quadrupole resonance for the one-, two- and three-neutron removal channels, finding 32, 27 and 22 mb respectively .

Both contributions increases in ∼90 mb the σ_I Glauber calculations. This is, indeed a contribution of just a ∼4% of the total value but is important to take it into account.

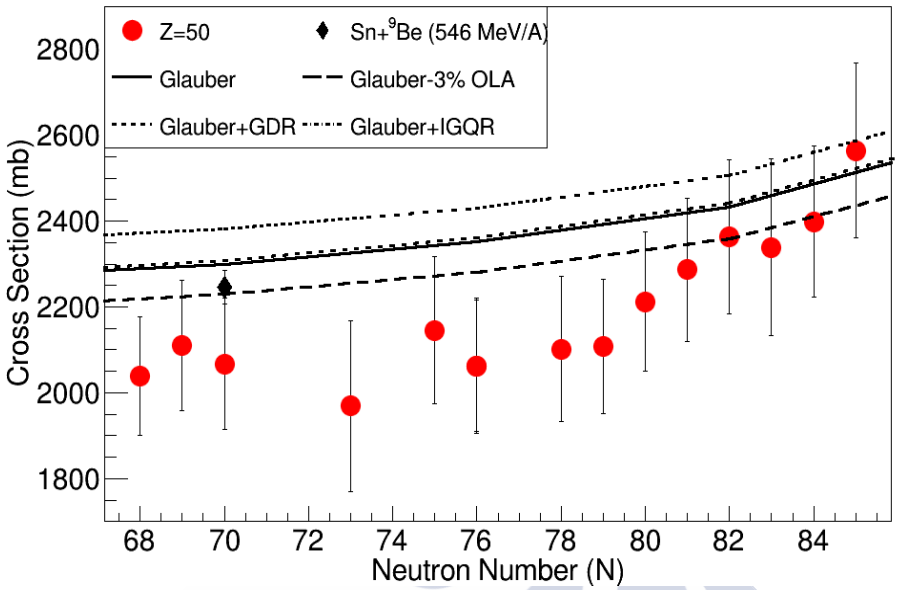

Figure 3.20: *Comparison between Glauber calculations (solid red line) and total reaction cross section measured in this work for Z=50 isotopes (red points). The dashed line represent the expected reduction in σ_R when not considering the OLA approximation [84]. The contributions of the GDR and IGQR are showed as dotted lines and dashed-dotted lines respectively. The result obtained by Renberg et al [60] with a proton beam on a tin target is showed here scaled to beryllium instead.*

3.5 Discussion

Figure 4.11 shows the comparison between Glauber calculations and the total reaction cross sections measured in this work. An average 10% overprediction is observed for isotopes below ^{130}Sn with respect to the solid red line in figure 4.11. After this point, as the measured cross section starts to grow, the deviation starts to decrease, finding a good agreement for isotopes between ^{132}Sn -^{135}Sn. However, as the calculation do not follow the observed evolution of the cross section with the neutron number, this low overprediction for very-neutron rich isotopes seems to be a consequence of this, and the overall overprediction is more likely to be a systematic effect. At this point, either the calculations fail on accurately describing the measurements, or the experimental cross sections are downscaled due to a sytematic effect on the measurement. A systematic overprediction of total reaction cross sections for energies close to 1GeV/A was already observed in Ref.[83] for O, Ne and Mg isotopes on a ^{12}C target.

According to our knowledge, only one measurement exists for ^{120}Sn at energies around 500 MeV/A [60]. Total reaction cross sections for a proton beam at 546 MeV hitting on a tin target were measured at CERN in the early seventies . Glauber's type calculations reproduce this results with a 1% deviation. Figure 4.11 shows the result obtained in this work (pink diamond) scaled to a beryllium target. The scaling was done quantifying the change in cross section when using proton or beryllium targets. A $\sim$4% deviation is observed with respect to our results.

An intense investigation looking for a systematic experimental effect causing a decrease in the measured cross section has been done. The thickness of the target has been studied scanning the changes in the measured Bρ distribution before and after the target for different isotopes. The results obtained corroborated the measurement performed by the GSI target laboratory and the associated uncertainty to this measurement was added to the error of the total reaction cross section.

A transmission problem is not considered because we selected fully transmitted nuclei along the FRS, specific magnetic settings were designed for maximize the transmission of ^{113}Sn, ^{119}Sn, ^{126}Sn, ^{126}Sn, ^{130}Sn, ^{132}Sn and ^{136}Sn, and they present very similar cross section values to their neighbours with a lower transmission. In addition, those isotopes produced by fragmentation present rather narrow position and angular distributions and the transmission is 100%.

An effect due to counting losses caused by the detection system was also investigated. However, to have an impact in the final cross section value, this effect needs to be different for measurements with and without target. As the detection system did not change during the experiment, this is also not considered. Still, this investigation lead to the discovery of an unbalancement of the relative percentage of Trigger #3 events in runs with and without target. An error in the PMT's signal readout failing in determining the time of flight for events reaching the final focal plane even though they did, lead to a missdentifying of a certain percentage of events. This percentage was found to be systematically bigger for settings without target. An underestimation of this error could mean that not all the losses are taken into account and some events are lost, reducing the cross section. However, this is highly improbable.

Glauber calculations are strongly dependent to the nucleon density distributions, depending on the parameters displayed by the fitting functions, one can find discrepancies of few % to the total value. For this reason, as better the description of the density function is, better the accuracy on the calculation, including a realistic description of these functions instead of a parametrization as it was done in this work, would provide a more accurate

calculation.

In addition, our Glauber calculations are based on what is called optical limit approximation (OLA). The Glauber model is a microscopic multiple scattering theory which calculates σ_R integrating over the impact parameter the reaction probability. This probability depend of the ground-state wave functions of target and projectile and the profile function, which encloses all the information of the elastic processes in the high-energy nuclear collision.

The optical limit approximation replaces the profile function by the NN cross sections and σ_R can be calculated from the nucleon-density distributions and nucleon-nucleon cross sections parametrizations. Even though this approximation works rather well in almost all the cases, a more accurate calculation can be performed when using the complete Glauber formalism.

Early this year, it was showed in [84] that non-approximated Glauber calculation always provide a better result than the ones obtained with the OLA approximation . An overestimation of a 3% is observed for incident energies aroung 1 GeV/A when the calculations are performed with the OLA approximation. Therefore, part of the deviation observed in our calculations with respect to the data, might be due to the application of the optical limit approximation. The expected reduction of the cross section with a complete Glauber calculation is showed as a dashed red line in figure 4.11.

The contribution of the GDR and IGQR to the total calculated reaction cross sections are showed as dotted and dashed-dotted lines in figure 4.11. The contribution of the IGQR increases a ∼4% the deviation from the experimental results. However, this contribution was not considered in Ref.[84].

Nonetheless, important conclusions have been obtained investigating the relative behavior of the different isotopic chains measured in this work. Glauber calculations represented as a solid red line in figure 4.11 shows an enhancement of the cross section after the N=82 shell closure, which is related with the increase of the neutron radius showed in figure 3.16. However, the measured cross sections show a different behavior. The enhancement of the cross sections is strongly related to the neutron-proton asymmetry of the nucleus. In fact, the measured cross section show two different trends depending on the nucleus isospin. Before N/Z≈1.6, the evolution of the cross section follows the expected evolution with $A^{1/3}$. After N/Z≈1.6, the cross section increases with the neutron excess.

The surprising systematic behavior observed in figure 3.14 is a consequence of the strong dependence of the cross section with the neutron excess. Nuclei bigger in mass but with lower neutron excess have smaller cross sections than nuclei smaller in mass but with larger isospin. This could be attributed to the presence of neutron skins in this region. These exotic struc-

tures are associated with large neutron density distributions and an increase in the nuclear size. In addition, they are strongly related to the neutron excess of the nucleus, and therefore can explain the previously commented effect.

Chapter 4

Nucleon-removal in medium-mass neutron-rich nuclei

4.1 Introduction

This chapter is dedicated to present the one-nucleon removal cross sections measured in this work. Both reaction channels, neutron- and proton-knockout were obtained for a wide variety of medium mass nuclei.

One-neutron removal cross sections were investigated for five different isotopic chains between Z = 48 - 52, the full systematic evolution of the cross section with the neutron number of the isotopes was measured, ranging from neutron-defficient to the neutron-rich side of the chart of nuclides. As an example, for the Z=50 isotopes, one-neutron knockout cross sections were obtained for nuclei between ^{113}Sn and ^{135}Sn. As a result, we measured one-neutron knockout cross sections for more than 70 medium-mass nuclei.

In addition, also one-proton knockout reactions were investigated. Even though the proton-removal channel is more restricted in transmission than the neutron one we succeded in measuring this reaction channel for 13 different isotopes with atomic numbers Z = 49, 50, 51 around the double-magic nuclei ^{132}Sn.

We also succeded in measuring both reaction channels simultaneously for the same isotopes, having crucial information on the behavior of both weakly and deeply bound nucleons. Another important feature is that we were able to measure neutron- and proton- knockout cross sections for isotopes beyond the double-magic shell-closure Z = 50, N = 82 where the only measurements found in literature were recently obtained by *V. Vaquero et al* [85].

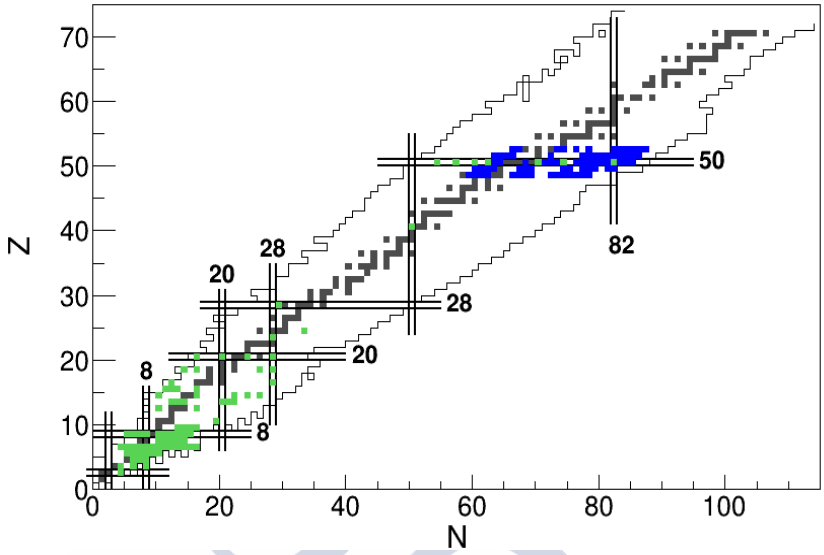

Figure 4.1: *Schematic representation of the chart of nuclides where it is highlighted in blue the isotopes for which inclusive one-nucleon knockout cross sections were measured in this work. It also shows highlighted in green, the variety of isotopes found in literature for which the same reaction channel has been measured.*

Figure 4.1 shows an schematic vision of the chart of nuclides where it is highlighted in blue the isotopes investigated in this work. In addition, it is also showed in green, the isotopes found in literature for which single-nucleon knockout cross sections have been measured until now. It is easily observed that almost all the results concerning this this reaction channel concentrates in the light-mass nuclei region. It is therefore clear that the measurements obtained in this work provide information in an almost no-investigated region of the chart of nuclides by using knockout reactions.

The results obtained in this work were interpreted using the latest version of the Liege Intranuclear Cascade Model (INCL) [37, 86]. In addition, a self-developed code was used to properly calculate the excitation energy induced in the A-1 fragment and its subsequent de-excitation. A realistic description of the structure of the isotopes is included to calculate the excitation energy induced by particle-hole excitations. The contributions of initial- and final-state interactions and the effect of nucleon-nucleon short-range correlations are taken into account.

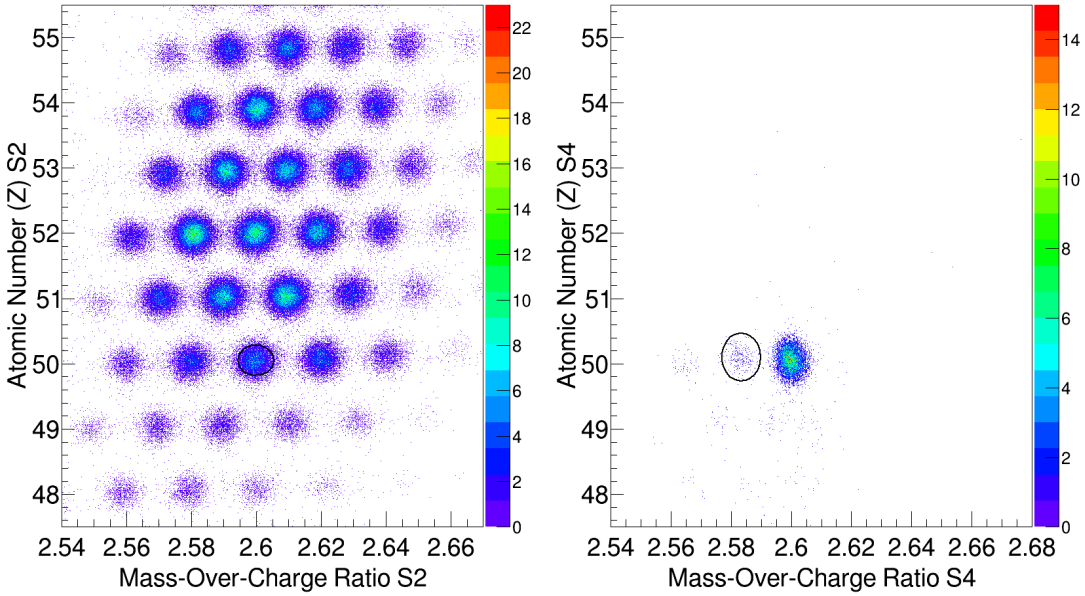

Figure 4.2: *The left panel shows the identification matrix at the intermediate focal plane for a magnetic setting centered around ^{130}Sn. The black circle represents the gate used to count the number of incoming ions. Right panel shows the identification matrix at the final focal plane conditioned to the gate placed in the left panel. The black circle represenst the gate used to count the number of one-neutron knockout fragments.*

4.2 Determination of the cross section

Two different reaction mechanisms, fragmentation of ^{132}Xe and fission of ^{238}U, were used in this experiment to produce large isotopic chains of medium-mass neutron-rich nuclei. The produced secondary radioactive ion beams and its knockout residues produced through the interaction with a thick target were studied using the FRS magnetic spectrometer. To accomplish this task, the FRS was used as a two independent fragment separators. The first part is used to identify the secondary radioactive ion beams and determine the number of incoming particles (N_p). Then, the second part is dedicated to identify and count the number of A-1 reaction products Y(A-1) induced by a 2591 mg/cm^2 ^{9}Be target placed at the intermediate focal plane. All the experimental details are described in chapter 2.

Single-nucleon knockout cross sections are determined by normalizing the number of A-1 reaction residues to the number of incoming projectiles and to the target surface density as follows;

$$\sigma(A-1) = \frac{Y(A-1)}{N_p N_t} \times F \tag{4.1}$$

where Y(A-1) is the number of counts at the final focal plane (S4) of the A-1 fragment and N_p represents the number of incoming projectiles obtained by counting at the mid-focal plane the number of (Z,A) isotopes before the target. In addition, N_t refers to the number of particles per unit area in the target material and the factor F takes into account all the corrections applied to the measured yields due to limitations of the experimental procedure, including secondary reactions, ion transmission through the spectrometer, charge states of the involved ions, and the dead time of the detectors. The left panel of figure 4.2 shows the identification matrix at the intermediate focal plane for a magnetic setting centered around ^{130}Sn. The black circle represents the gate used to count the number of incoming ions (N_p). The right panel shows the identification matrix at the final focal plane for the reaction fragments of ^{130}Sn colliding with a ^{9}Be target. The black circle represents the gate used to count the number of one-neutron knockout residues (Y(A-1)).

In the following sections we will explain those corrections due to secondary reaction. The correction associated to the dead time of the detectors was already explained in section 3.2.3 and the same factors are applied here.

4.2.1 Secondary reactions

Particles traveling along the FRS may experience reactions with the different layers of matter placed along the beam line. Reactions modifying the isotopic composition of the nucleus of interest lead to an underestimation of the measured production yields which must be corrected in order to obtain the correct value of the cross section. For both incoming and outgoing nuclei, the probability of having secondary reactions is calculated using AMADEUS [61], where interaction cross sections are calculated according to Karol's prescription with an accuracy of around 10% [21]. A correction factor was calculated for each nucleus as the inverse of their survival probability after crossing different layers of matter.

The probability of having secondary reactions in the first part of the FRS is calculated in average for the tin isotopic chain to be around ∼27%. For the second part, the calculated probability of having secondary reactions for the A-1 fragment is in average ∼24.5%. Thus, as both correction factors are applied, the overall correction will be ∼2.5%. The associated error to the total reaction cross section determination induces an error of ∼2% in the one-neutron removal cross section due to this correction. The contribution of this correction to the final value of the uncertainty of the measurement is

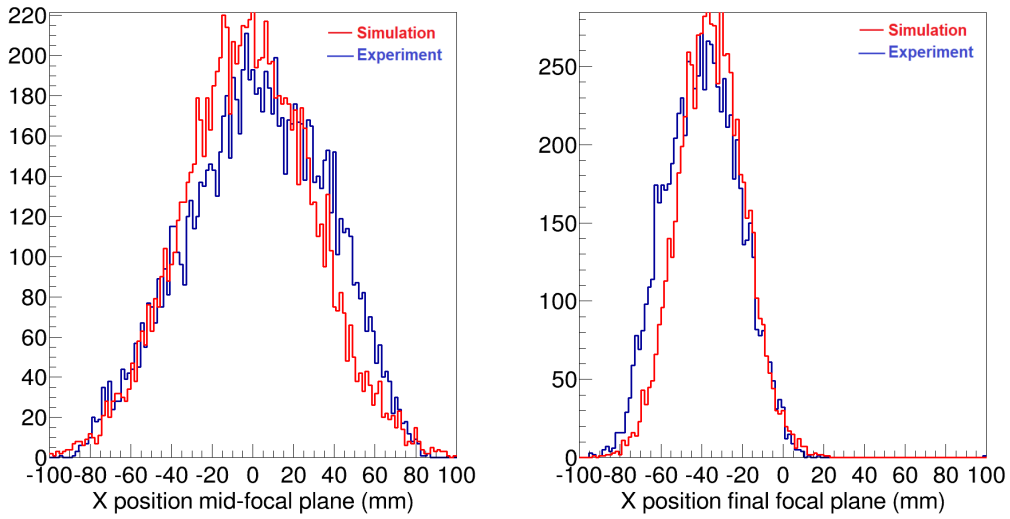

Figure 4.3: *Comparison between the experimental and simulated horizontal-position distribution for ^{130}Sn isotopes with MOCADI [63]. The left panel shows the comparison at the intermediate-focal plane and the right panel the same at the final-focal plane.*

detailed in tables 4, 5, 7, 6 8 in appendix B. A detailed description of the different layers of matter placed along the beam line is found in table 12, appendix C.

4.2.2 Transmission correction

Fragments traveling through the spectrometer follow different trajectories depending on their mass-over-charge ratio. As we measured large isotopic chains in this experiment, several magnetic settings were employed because of the limited acceptance of the FRS in momentum (±1.5%) and angle (±15 mrad). Each of the magnetic settings was centered on different tin isotopes, which means that for that particular isotope, the transmission will be optimized, but as far as we separate from this isotope, the transmission falls.

As we already mentioned in section 3.2.4, the transmission along the spectrometer for the fragments produced by fission or by fragmentation is different. Typically, fragments coming from the fragmentation of the xenon beam have narrow angular and momentum distributions so the transmission is close to 100% for isotopes following centered trajectories. However, the fission fragments coming from the uranium beam present relatively broader angular and momentum distributions, and the transmission should be calcu-

lated carefully.

For that reason, a very precise simulation for each of the investigated nuclei was performed using the MOCADI code [63]. In this work, only the transmission from the intermediate focal plane to the final focal plane is needed. As we determine the ratio between the number of counts measured at S4 and S2, transmission losses of the arriving particles at S2 will affect only the available statistics but not the cross sections.

The full calculation is divided in two simulations. A first calculation of the trajectory along the whole spectrometer is performed in order to validate the accuracy of the simulation and to benchmark the position distribution at S4. Figure 4.3 shows the experimental and simulated position distributions for the fission produced isotope ^{130}Sn. A good agreement is found between them, finding deviations of 4-5 mm at its worst. A relative deviation of the position at S4 of 4-5 mm induces a $\sim$5% change in transmission.

However, deviations from the experimental distributions at the mid focal plane will not affect the final transmission correction factor. A second calculation is performed simulating the trajectories from the secondary reaction target to S4, where the parameters (mean value and RMS radius) of the experimental angular and position (horizontal and transversal) distribution at S2 are included as inputs. Then, transmission losses are calculated and the number of ions arriving at S4 is corrected.

Table 10 found in appendix B shows the calculated transmission values from S2 to S4 for the neutron-knockout residues produced and investigated in this work. It is important to notice that as we move away in atomic number from Z=50, the transmission of the produced fragments in the reaction decreases. Typically, cadmium, indium and tin isotopes have transmission values over the 80% for all of their isotopes. On the other hand, the fragments produced with antimony experience transmission values around 60% and the telurum nuclides studied show transmission values around 40%.

Table 9 found in appendix B shows the calculated transmission values from S2 to S4 for the Z-1 fragments investigated. Special magnetic settings were needed in order to transmit the Z-1 fragments of the reactions. Only products with relatively high transmission were studied in this work. Indium and Tin isotopes show high transmission rates, all over 80%, but we can see that for Antimony isotopes the transmission values drop to 60%.

The systematic error associated with the transmission correction is the largest one. In the cases where the transmission is relatively high, almost the full position distribution is inside the physical limits of the detectors and thus, we can simulate them with high precision. However, small deviations of 2 or 3 mm from the experimental distribution induce changes in the calculated transmission of a few percent. In addition, deviations between the experi-

mental and simulated angular distributions also induce certain uncertainty in the accuracy of the transmission calculation. Therefore, the associated uncertainty to this correction is around 10%.

4.2.3 Ion charge states

Finally, fragments traveling along the FRS can pick-up or strip off some electrons due to interactions with the different layers of matter in the beam line. This effect can alter the mass-over-charge ratio of the ions and therefore lead to an underestimation of the measured yields. In our experiment, only the charge states produced between S2 and S4 affect the measurements and therefore must be corrected. The probability of producing charge states is calculated with the AMADEUS code, and then applied to the number of counts gathered at the final focal plane. This correction is found to be around 2% in average for all the isotopes investigated in this work. The associated uncertainty to this correction is ∼5% [87] .

4.3 One-neutron knockout cross sections

Figure 4.4 shows the one-neutron removal cross sections (σ_{1n}) measured in this work as a function of the neutron number of the projectile nucleus. Five different elements were investigated, Cadmium (Z=48), Indium (Z=49), Tin (Z=49), Antimony (Z=51) and Telurum (Z=52). A rather complete systematic measurement was obtained for all of them, covering a wide range in isospin.

The associated uncertainty to the measurement $\Delta\sigma_{1n}$ is calculated combining statistical and systematic errors. Statistical uncertainties are calculated as follows:

$$\Delta\sigma_{1n}^{stat} = \frac{1}{N_t}\sqrt{\left(\frac{\partial\sigma_{1n}}{\partial N_2}\right)^2 \cdot (\Delta N_2)^2 + \left(\frac{\partial\sigma_{1n}}{\partial N_4}\right)^2 \cdot (\Delta N_4)^2} \qquad (4.2)$$

Where ΔN_2 and ΔN_4 are the associated uncertainties to the number of counts at the intermediate and final focal planes. Systematic errors are those related to the different corrections applied and were described in the previous section. The results obtained in this work and their uncertainties are shown in tables 4, 5, 7, 6, 8 found in appendix B.

Figure 4.4 also shows the comparison of our results with other measurements found in literature [32, 34, 35, 88, 85] and a good agreement is found with all of them. In [32] the flat evolution of the cross section between ^{110}Sn

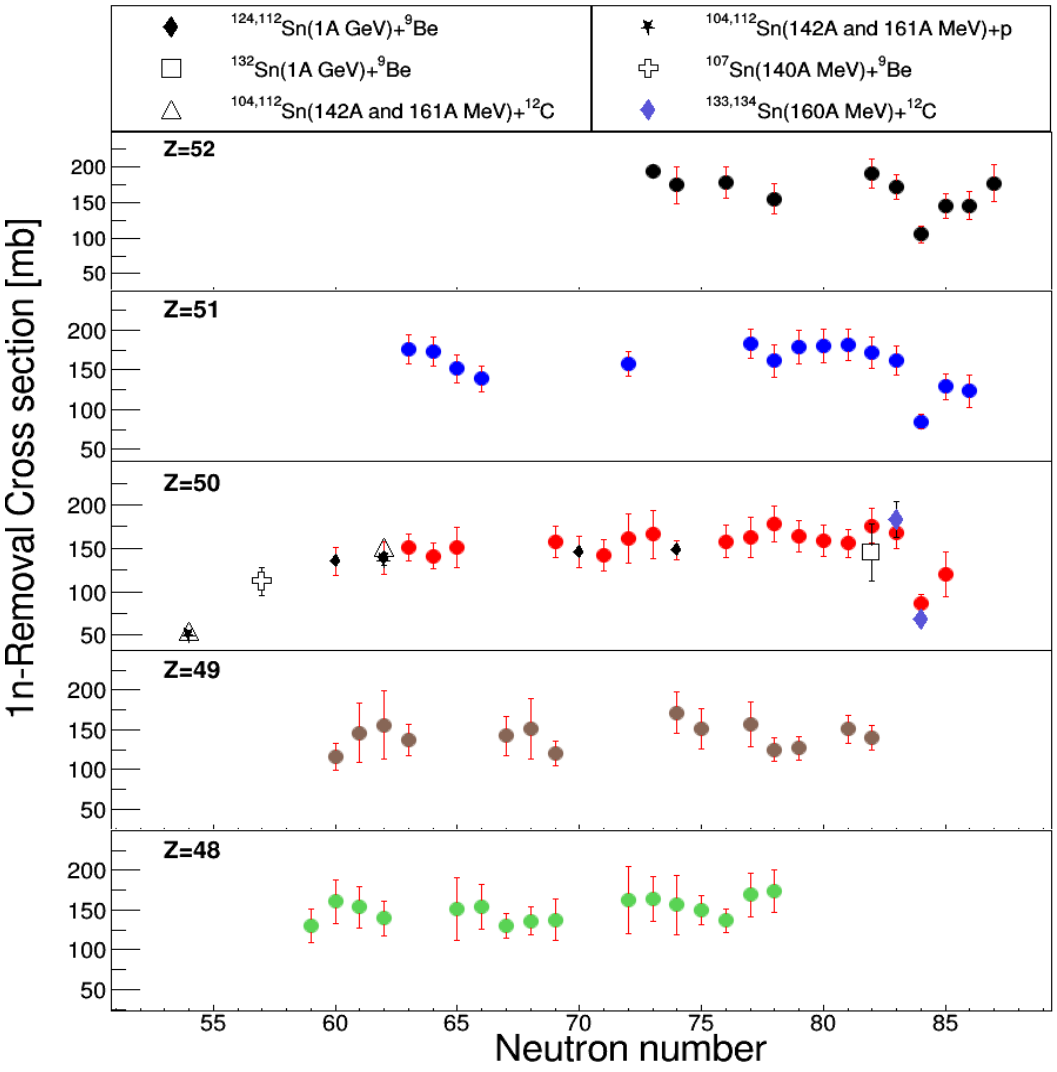

Figure 4.4: *One-neutron removal cross sections measured in this work for 5 different elements. We also show data measured by Pérez Loureiro et al. (open squares) [34], Audirac et al. (open triangles and solid stars) [35], Cerizza et al. [88] (open cross), J.L. Rodríguez-Sánchez et al [32] (solid diamonds), V. Vaquero et al. [85] and this work (solid dots).*

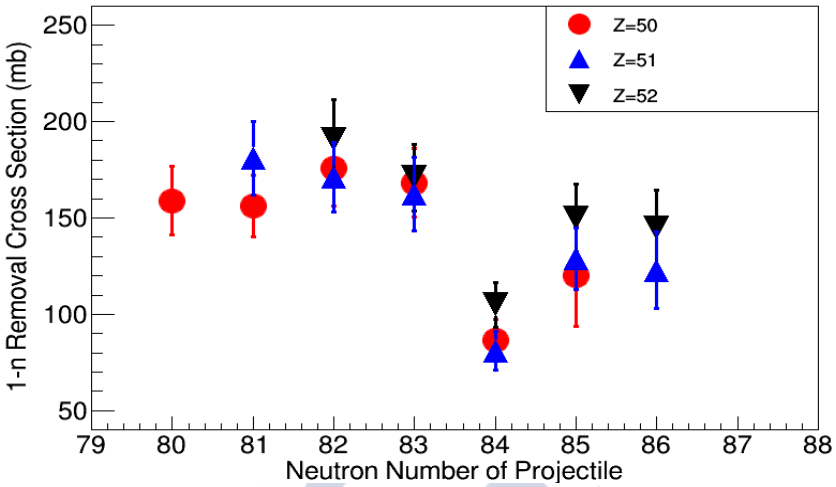

Figure 4.5: *One-neutron removal cross section as a function of the neutron number of the projectile. Tin (red dots), Antimony (blue triangles) and Telurum (black triangles) are shown. An important decrease in cross section is seen for N=84 isotones.*

and ^{132}Sn was discussed and explained through the competition between the probability of producing an A-1 fragment in the collision stage and the survival probability in the de-excitation stage.

However, the majority of the experiments were not able to measure one-nucleon knockout reactions for very neutron-rich nuclei. Only last year, *V. Vaquero et al* [85] measured one-neutron removal cross section for ^{133}Sn and ^{134}Sn at Riken. In this experiment, they reported a drop in the one-neutron removal cross section for ^{134}Sn. With our original experimental scheme we were able to measure one-neutron knockout cross sections for 10 isotopes in this region. $^{133-135}$Sn, $^{134-137}$Sb and $^{135-139}$Te. Figure 4.5 shows the one-neutron removal cross section as a function of the neutron number for isotopes around the double shell closure (Z=50,N=82). As can be seen, all the isotones present a similar overall value for the cross section with a clear drop in cross section for N=84.

To understand this behavior one should consider that the one-neutron removal cross section is governed by two main features. As the nucleon knockout is a very peripheral collision, the amount of neutrons available in the outskirts of the nucleus will influence the probability of removing one of them. After that, when the projectile has already lost one of its nucleons, the excitation energy induced by the removal process, together with its neutron separation energy, will determine the survival probability of the knockout

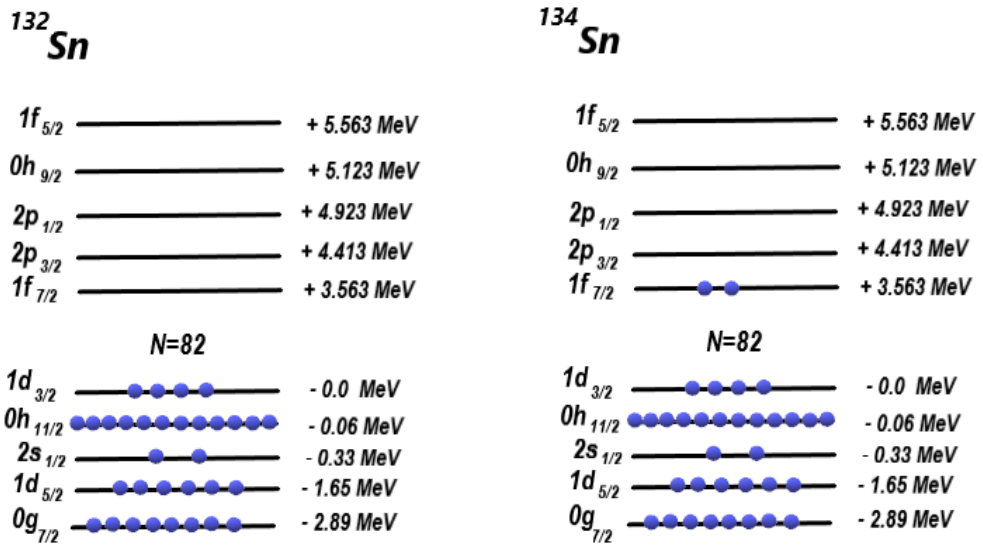

Figure 4.6: *Simple representation of the neutron structure inside two different tin isotopes. Left panel shows the level scheme for ^{132}Sn. Right panel shows the same structure for ^{134}Sn. The levels organization is taken from [89] as well as the energies. However, the energy gap is taken from the measured γ-ray transition from the $1f_{7/2}$ to the $0h_{11/2}$ orbitals observed in [85]. The energies are related to the $1d_{3/2}$ level.*

residue against neutron evaporation.

According to the particle-hole excitation picture, the excitation energy induced in the system depends heavily on the structural properties of the nucleus. Left panel of figure 4.6(a) shows a very simple representation of the sequence of single-particle orbitals of the neutrons in a N=82 nucleus, adopted from [89]. After the collision takes place, the excitation energy gained is determined by the energy difference between the orbital occupied by the removed nucleon and the Fermi level.

When one of the valence neutrons is removed, the system will not gain any excitation energy ($1d_{3/2}$ in this case of ^{132}Sn). If one of the deeper neutrons is removed in the collision, the pre-fragment will gain a sizable amount of excitation energy.

4.3.1 N $\leq$ 82 Isotopes

For isotopes with N $\leq$ 82 the probability of removing one of the neutrons located in states close to the Fermi level is relatively high. Indeed, the $0h_{11/2}$ orbital itself contains a large number of neutrons and the energy difference with the Fermi level is just of 0.06 Mev according to [89]. The probability of

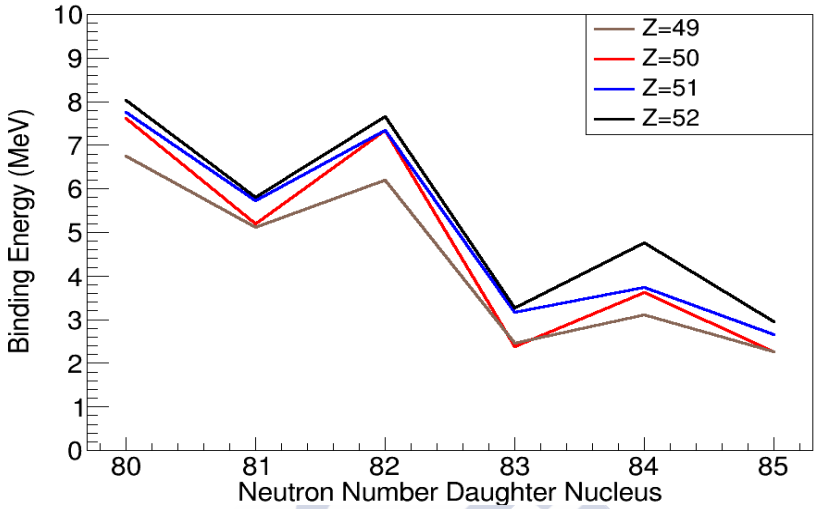

Figure 4.7: *Neutron separation energy(MeV) as a function of the neutron number. The red line corresponds to Z=50 isotopes, the blue one to Z=51 and the black one represents Z=52 nuclei.*

removing one of the $0h_{11/2}$ neutrons inducing low excitation energy is around 25% according to our calculations.

The excitation energy induced by the particle-hole picture is not sufficient to overcome the relatively high neutron separation energies of the daughter nucleus showed in 4.7. This is why the survival probability of the A-1 fragment is around 80% as only the less probable removal of deeper neutrons would overcome the high neutron-emission threshold.

This competition between excitation energy and binding energy explains the similar values for the cross section below the double shell closure for all of the isotopes measured in this work.

4.3.2 N > 82 Isotopes

The right panel of figure 4.6 shows the neutron level scheme for ^{134}Sn. Despite of only adding one (^{133}Sn) or two neutrons (^{134}Sn) with respect to the double-magic nucleus ^{132}Sn, an important structural change is produced. The Fermi level of the system is now above the N=82 shell gap, meaning than the valence neutrons, those occupying the last incomplete filled orbital, are distributed among the $1f_{7/2}$, $2p_{3/2}$, $2p_{1/2}$, $0h_{9/2}$, $1f_{5/2}$, $0i_{13/2}$ orbitals with a given probability.

As it is known, one of the implications of shell closures is the strong separation in energy between two consecutive orbitals.

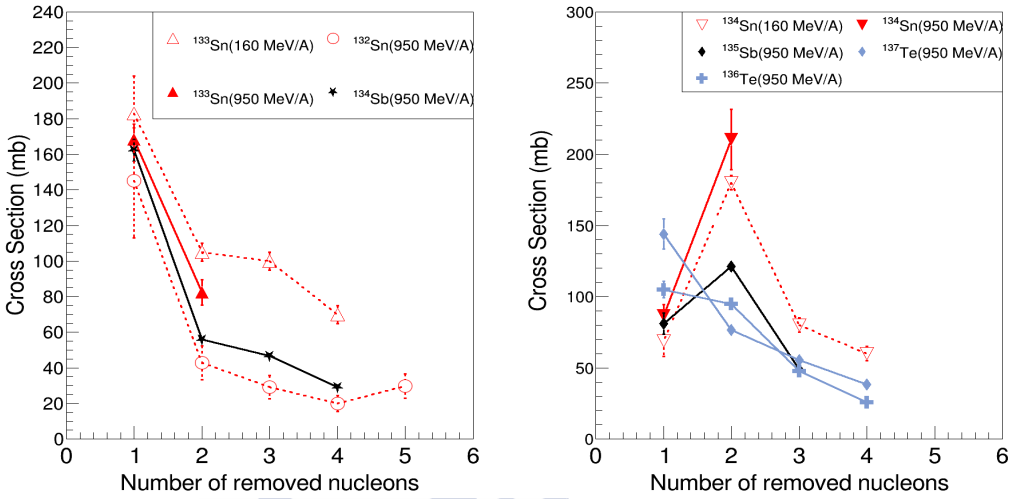

Figure 4.8: *(Color online). Multi-neutron removal cross section as a function of the removed nucleons. Left panel shows the results for isotopes with $N \leq 83$. This work; ^{133}Sn (red filled triangles) and ^{134}Sb (black stars), V. Vaquero et al [85], ^{133}Sn (empty red triangles) and D. Perez [90], ^{132}Sn (empty red circles). Right panel shows the results for isotopes wihn $N > 83$. V. Vaquero et al [85], ^{134}Sn (empty red triangles), this work; ^{134}Sn (red triangles), ^{135}Sb (black diamonds), ^{136}Te (grey crosses), ^{137}Te (grey diamonds).*

In our case, the excitation energy induced in the reaction as a consequence of removing a neutron, will increase reducing the survival probability. Following the already used example for isotopes with N $\leq$ 82, the $0h_{11/2}$ orbital is still dominant, as it contains a large number of neutrons. Now the fact of having neutrons above the N=82 shell gap produces that the induced excitation energy includes now the energy of the N=82 shell gap, which is measured to be around 3.5 MeV according to the γ-ray transition measured by *V. Vaquero et al* [85].

Furthermore, figure 4.7 shows a decrease of the binding energy in the N $>$ 82 region, meaning than the survival probability of the nucleon removal remnant reduces considerably. The witnessed drop in cross section is observed for the N=84 isotones and not for N=83 isotones, even if they have more than 82 neutrons. The key feature in this process is the structure of the daughter nucleus. In the ^{134}Sn(^{9}Be,n)^{133}Sn reaction, the daughter nucleus is a N=83 nucleus. The combination of having large induced excitation energies and low binding energies of the daughter nucleus (2.4 MeV) is translated in a low survival probability of the A-1 fragment. Meanwhile, in the ^{133}Sn(^{9}Be,n)^{132}Sn reaction, the binding energy of the daughter nucleus is

relatively large (7.4 MeV) and the excitation energy lower which makes the excitation energy to be below the particle emission threshold.

Figure 4.8 shows the measured multi-neutron removal cross section as a function of the number of removed neutrons measured in this work. The left panel of figure 4.8 depicts this magnitude for projectiles with neutron number N $\leq$ 83. Due to the the high binding energies of the A-1 daughter nucleus and the low excitation energies induced in the reaction, the survival probability of the one-neutron removal fragment is high and σ_{1n} is bigger than σ_{2n}.

However, for projectiles with N $>$ 83 (right panel of figure 4.8), the two-neutron-removal cross section is bigger than σ_{1n} as a consequence of the lower survival probability of the A-1 fragment and consequently nucleon emission in the de-excitation stage. Whenever the excitation energy is above the particle emission threshold, a second neutron is emitted and the separator will register this event as an A-2 nucleus. This, produces a huge enhancement of σ_{2n} in this region for all the investigated isotopes except for ^{137}Te, where the trend changes back to the one obtained for N $\leq$ 83 isotopes situation.

4.4 Model calculations

As we already explained in section 1.2 there are several mechanisms contributing to the one-nucleon removal cross section.

- Knock-out of a nucleon as a result of single nucleon-nucleon interaction.
- Evaporation of nucleons due to the excitation of collective nuclear modes.
- Evaporation of a secondary nucleon due to the excitation energy gained in the collision, typically induced by particle-hole excitations and final state interactions.
- Inelastic NN collisions resulting in the production of a pion and its subsequent absorption, inducing a large amount of excitation energy over the nucleon-emission threshold.

In order to evaluate the role of these contributions we decided to use an improved version of the Liege Intranuclear Cascade Model (INCL) [86] to describe this reaction mechanism. This code is based on a Monte Carlo description of the Glauber's theory, with a realistic description of the nuclear periphery through the incorporation of Hartree-Fock calculations for the nucleons radial densities[91].

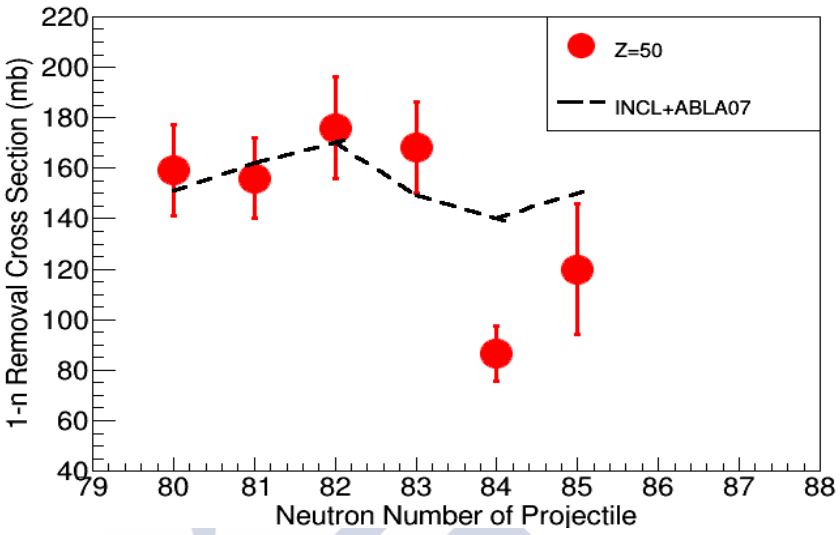

Figure 4.9: *One-neutron removal cross section for Z=50 isotopes (red points) in comparison with the results obtained INCL+ABLA07 calculations (dotted red line)*

In this approach, the nuclear collision is treated as successive relativistic binary nucleon-nucleon collisions separated in time, where the position and momentum of the nucleons are followed as time evolves. The possibility of following in time all the participant particles in the collision allow us to determine their scatter probabilities with other nucleons, evaluating the effect of final state interactions in the A-1 remnant. Furthermore, this dynamical model allow us to characterize the remnant of the collision in atomic and mass number, excitation energy, and angular momentum. In this way we can calculate the number of remnants of the collision with a certain mass and atomic number, meaning that after a normalization we can calculate what we call "***primary cross section***" which is the number of N-1 remnants produced in the collision stage. In addition, the production of pions in NN inelastic collisions and the re-absorption probability by the nucleus is reliably described by the code, and thus this effect can be evaluated.

Then, the de-excitation of the remnants is performed with codes based on the statistical evaporation model. Typically, ABLA07 [92] describes the de-excitation of the remnants via evaporation of nucleons and alpha clusters described according to the Weiskopf's formalism [93]. This approach has been bench marked in several works for describing the evaporation residues or fission fragments produced in spallation or fragmentation reactions [94, 95, 96].

Figure 4.9 shows the comparison between the one-neutron removal cross

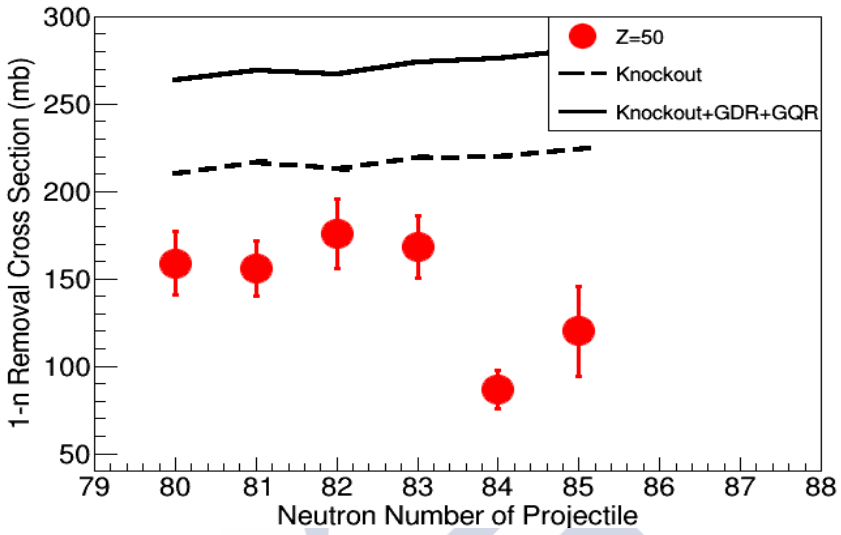

Figure 4.10: *One-neutron removal cross section for Z=50 isotopes (red points). Primaries cross section produced in de collision stage with Intranuclear Liege Cascade Model (dashed black line). Final production of A-1 fragments combining the production as a result of one target-projectile interaction and the excitation of collective nuclear modes (solid black line).*

sections for tin isotopes measured in this work around ^{132}Sn, with the results obtained with standard INCL plus ABLA07 calculations. Even though the overall magnitude of the cross section is reasonable well described for isotopes lighter than ^{133}Sn, an overprediction of the cross section is obtained after the double-shell closure, where a large reduction of the measured cross section is observed due to the change in nuclear structure.

The fact is that INCL does not include any information on the structural properties of the nuclei involved in the collision, which represent a clear limitation on the interpretation of the results. In order to improve the results obtained with INCL+ABLA07 we coupled the results of the INCL calculations to a de-excitation model based on particle-hole excitations with realistic single particle energies for the orbitals and binding energies. In addition, advanced calculations based on the radial distribution of the orbitals and the collision's impact parameter were developed to calculate the probability of removing nucleons from different orbitals.

4.4.1 A-1 fragment production

The A-1 production as a result of one nucleon-nucleon collision is calculated with the INCL code. However, initial state interactions due to the excitation of collective nuclear modes may contribute to the removal of a nucleon.

Sections 3.4.1 and 3.4.2 of the previous chapter described the contribution to σ_R of the electromagnetic and nuclear excitation of collective nuclear modes. The excitation energy gained in these processes is in general sufficient for the subsequent emission of a neutron, contributing then to the one-neutron removal cross section. However, if the energy is large enough to overcome the two-neutron separation energy, then two neutrons are emitted contributing to the two-neutron removal cross section instead.

Figure 3.18 of section 3.4.1 shows the electromagnetic cross section as a function of the excitation energy. Here, a 55% of the distribution is between the one-neutron and two-neutron separation energies meaning that in more than half of the cases, this process will contribute to the one-neutron removal cross section. The overall value of this contribution is found to be around $\sim$6 mb for ^{132}Sn, with small variations for the other isotopes.

In addition, figure 3.19 of section 3.4.2 shows the calculations of the GDR and IGQR contribution to σ_R. It is found that the nuclear excitation of the isoscalar giant quadrupole resonance contributes with $\sim$80 mb in average for the tin isotopes measured in this work to the total reaction cross section. Out of this contribution, only a fraction goes to the one-neutron removal cross section depending on its energy spectrum. This spectrum was measured in Ref.[17] for ^{120}Sn finding a distribution that peaks at $\sim$12 MeV. Also, a recent experiment performed at GSI by Ref.[82], showed some preliminary results on the contribution from the giant quadrupole resonance to the one-neutron removal cross section for ^{124}Sn and ^{128}Sn. They measured a contribution to the one-neutron removal channel of 33 $\pm$ 3 mb for both isotopes.

Same model used to calculate the energy distribution of the GDR showed in figure 3.18 was used to estimate the energy distribution of the IGQR and the contribution to the one-neutron removal cross section. It was found that the contribution to the one-neutron removal channel is around $\sim$60% of the total energy distribution for ^{128}Sn which means a $\sim$48 mb for this isotope. The contribution of the IGQR decreases with the neutron number, the lowest contribution is calculated for ^{135}Sn (44 mb) and the largest for ^{113}Sn (53 mb).

Despite of having a $\sim$20%, $\sim$15 mb, difference between the calculations and the preliminary results from Ref.[82], this deviation is found within the error bars of the measurement.

Figure 4.10 shows the measured one-neutron removal cross section as

a function of the neutron number for the Z=50 isotopes compared to the primary cross sections calculated with INCL (dashed black line) and the final production of A-1 fragments including initial state interactions (solid black line). As it is expected, the calculation largely overestimates the data because it does ot consider the survival probability of the remnant nuclei against possible excitations.

4.4.2 Knock-out residue de-excitation

The large overestimation of the cross section observed in figure 4.10 suggests that the one-neutron removal cross section is strongly affected by core excitations. Three different sources of excitation energy are considered to contribute to de-excitation of the remnant; particle-hole excitations, final-state interactions and inelastic NN collisions. In addition, the large reduction observed after ^{133}Sn suggests that core excitations are strongly dependent off structural effects. It is therefore needed to include in our calculations a realistic description of the neutron single-particle levels for every isotope and precise probabilistic calculation regarding the chances of removing a nucleon from a given orbital.

Particle-hole excitations

The Independent Particle Model (IPM) [97] provides a picture of the nucleus where nucleons move freely in an average potential generated by the interactions with all nucleons of the nucleus. According to this model, each nucleon is alleged to move in a determined orbital with a certain energy associated to each orbital. The energy of this orbitals around ^{132}Sn have been largely investigated over the last decade through both theoretical [89, 98] and experimental [99, 100, 101] approaches thus, plenty of information can be found in literature.

One of the main features to achieve a realistic description of the inner structure of the nucleus remains on introducing experimentally measured energy for the orbitals every time possible. A precise determination of this energy is vital through it will determine the excitation energy induced by particle-hole excitations in the nucleus after the collision. Some of the levels are not easy to reach experimentally and in this cases, theoretical values are used. In our case, the level's organization and energies are taken from Ref. [89] except for the energy of the N=82 gap, which is taken from the measurement performed by *V. Vaquero et al* [85]. An schematic representation of the level scheme and associated energies used in this work is displayed in figure 4.6.

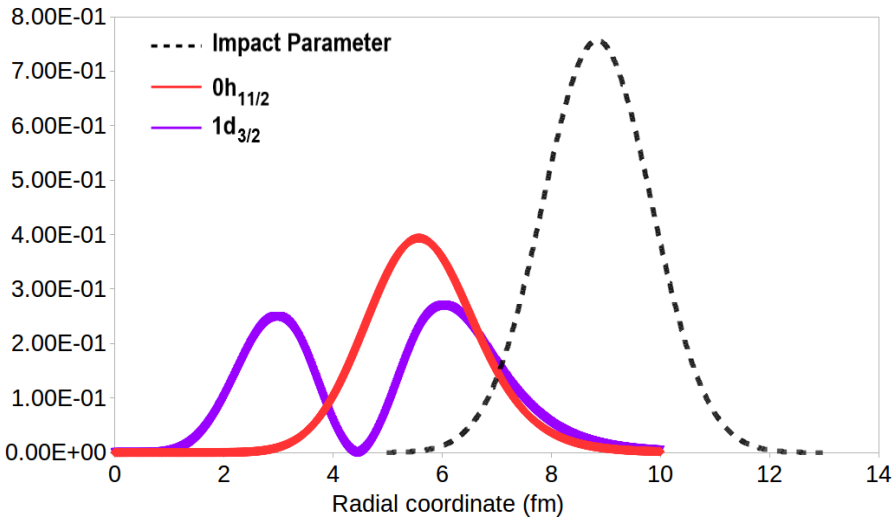

Figure 4.11: *Radial distribution of the $1d_{3/2}$ (purple line) and $0h_{11/2}$ (red line) orbitals of ^{132}Sn obtained from Hartree Fock calculations with a Skyrme Sly5 interaction [102]. The impact parameter of the collision $^{132}Sn(^{9}Be,n)^{131}Sn$ calculated with INCL is represented as a dashed black line.*

The probability of removing a nucleon from a given orbital is obtained from the overlap between the distribution of the impact parameters of the one-neutron knockout process, calculated with INCL, and the orbital's radial distribution, obtained from Hartree Fock calculations with a Skyrme Sly5 interaction [102].

Figure 4.11 shows the overlap between the radial distributions of the $1d_{3/2}$ (pruple line) and $0h_{11/2}$ (red line) orbitals for a ^{132}Sn nucleus and the impact parameter (dashed lined) of the ^{132}Sn(^{9}Be,n)^{131}Sn reaction calculated with INCL. By calculating the relative fraction of the different orbitals lying in the overlap region with the impact parameter one can obtain the probabilities of removing a nucleon from the different orbitals. For each orbital, a certain probability is assigned for each event. Then, a random generator based on the calculated probabilities selects the orbital where the removed nucleon was located.

Table 4.1 shows the removal probabilities from the different orbitals calculated with the above described model for ^{132}Sn and the associated induced excitation energies. Taking into account that the neutron emission threshold for ^{131}Sn is 5.204 MeV, the probability of producing bound one-neutron knockout residues is around 80% in this case.

For isotopes with N > 82 the fragmentation of the single-particle strength and the partial occupation of higher energy/momentum states is taken into

Orbital	Probability	Energy (MeV)
$1d_{3/2}$	14.7 %	0.00
$0h_{11/2}$	24.3 %	0.06
$2s_{1/2}$	12.1 %	0.33
$1d_{5/2}$	20.2 %	1.65
$0g_{7/2}$	6.50 %	2.89
$0g_{9/2}$	8.88 %	7.87
$1p_{1/2}$	1.91 %	8.95
$1p_{3/2}$	3.93 %	11.5
$0f_{5/2}$	1.70 %	10.3
$0f_{7/2}$	2.96 %	14.85
$1d_{3/2}$	0.45 %	18.47

Table 4.1: *Calculated probabilities and associated excitation energies obtained with particle-hole calculations for ^{132}Sn described in the text.*

account. In Ref.[85] the probability for the two valence neutrons of ^{134}Sn to occupy the $1f_{7/2}$ orbital is determined with shell model calculations [103], finding an occupation probability of 80%. Then, probabilities between 1.6% and 5.2% are calculated for the occupation of the $2p_{3/2}$, $2p_{1/2}$, $0h_{9/2}$, $1f_{5/2}$, $0i_{13/2}$ orbitals. However, the partial occupation of just 80% of the $1f_{7/2}$ orbital has a minor impact in the final value of the one-neutron removal cross section. As the, energy difference between this orbital and the higher ones is not significantly large, the induced excitation energy is very similar when the valence neutrons are in the $1f_{7/2}$ state or higher orbitals. Even though the fragmentation of the single-particle strength is included in our calculations, this effect increases the cross section just a 3%.

Final-state interactions

Nucleon rescattering, final state interactions, also contributes to core excitations. The intranuclear cascade model provides a suitable tool to calculate this contribution as it can follows the trajectory of the nucleon as time evolves an therefore, evaluate the number of collisions that suffer before leaving the nucleus. In addition, the dissipated energy in each of the collisions is also evaluated. According to INCL, a 55% of the knocked-out nucleons experience multiple collisions inside the nucleus for reactions induced by ^{132}Sn colliding with a ^{9}Be target at 950 MeV/A and producing an ^{131}Sn fragment. This number, barely changes for all the isotopes investigated in this work.

The extra excitation energy induced in a single rescattering can be sub-

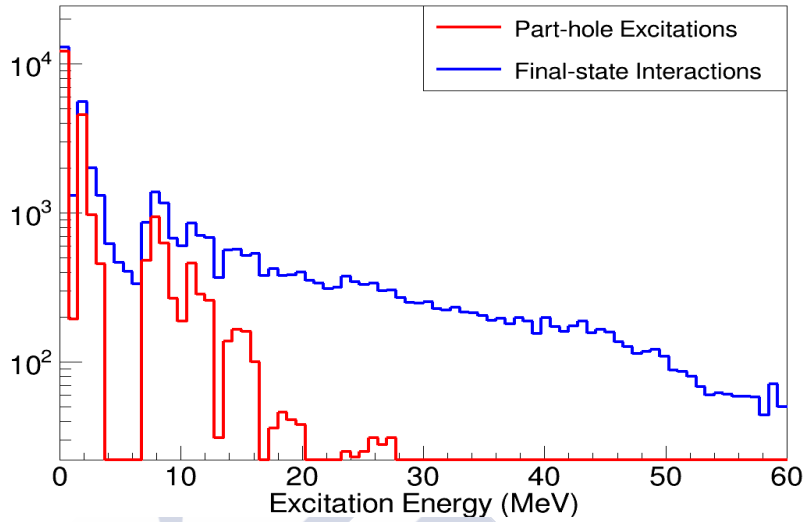

Figure 4.12: *Excitation energy spectrum of ^{131}Sn coming from a ^{132}Sn beam colliding with a ^{9}Be target at 950 MeV/A. The red line shows the excitation energy calculated according to particle-hole excitations. The blue line represents the excitation energy induced in the system when final-state interactions are considered. The y-axis is represented in logarithmic scale.*

tracted from the excitation energy spectrums of the A-1 fragment. The difference between the spectrum for the events with no final state interactions and the events with a rescattering collision is precisely the contribution coming from this magnitude. The deconvolution of both spectrums allow us to isolate the energy dissipated in a secondary rescattering alone. It is found that the contribution follows a function built as an exponential starting at 0 and a gaussian peaking at 15 MeV.

Figure 4.12 shows the result of including the extra energy due to final state interactions in the excitation energy spectrum of ^{131}Sn. The red line represents the calculated excitation energy spectrum due to particle-hole excitations, it can be seen how a rather discrete spectrum is obtained due to the inclusion of the structural properties in the model. The blue line represents the excitation energy distribution but including the effect of final state interactions. It can be seen that an overall increase in the excitation energy is induced. Indeed, our calculations show that the mean excitation energy induced in the system increases from 3.1 MeV when considering particle-hole excitations to 12.2 MeV when final-state interactions are taken into account for the neutron removal of ^{132}Sn at 950 MeV/A .

This effect is directly related to the survival probability of the A-1 frag-

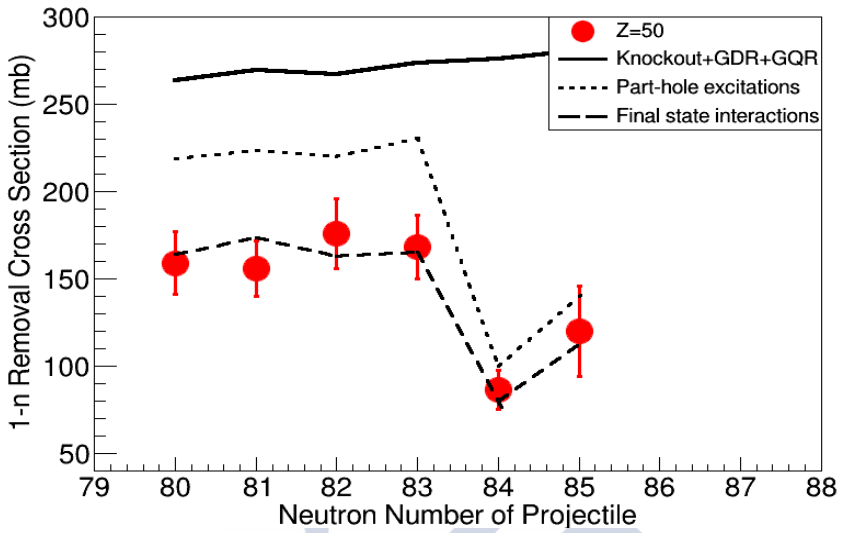

Figure 4.13: *Comparison between the calculated one-neutron removal cross sections with just the excitation energy induced by particle-hole excitations (dotted red line) and the calculation including final state interactions (red dashed line) with the measured one-neutron removal cross section for tin isotopes (red dots).*

ment. Such an increase in the overall excitation energy reduces the survival probability of the ^{131}Sn core from ∼80% to 51% which represents a 65 mb reduction of the one-neutron removal cross section in this case. Figure 4.13 shows the comparison between the predicted one-neutron removal cross sections with the excitation energy calculated just from particle-hole excitations (red dotted line) and the calculations including final states interactions (red dashed line) with the measured one-neutron removal cross sections for tin isotopes.

Inelastic NN collisions

Finally, in inelastic NN collisions where the nucleon is excited to different states such as Δ resonances, pions π are produced as a result of the subsequent decay of these resonances. Because of the large πN cross section, these pions have a non-zero probability of being re-absorbed by the nucleus inducing high excitation energies above the nucleon-emission threshold. [104, 105].

The Intranuclear Cascade Model also allows us to investigate this mechanism. Here, the one pion production at low incident energy (below ∼2 GeV) is produced in the process NN→NΔ with the subsequent de-excitation $\Delta\rightarrow\pi$N and the σ_T(NN→NNnπ) cross sections for the production of n pi-

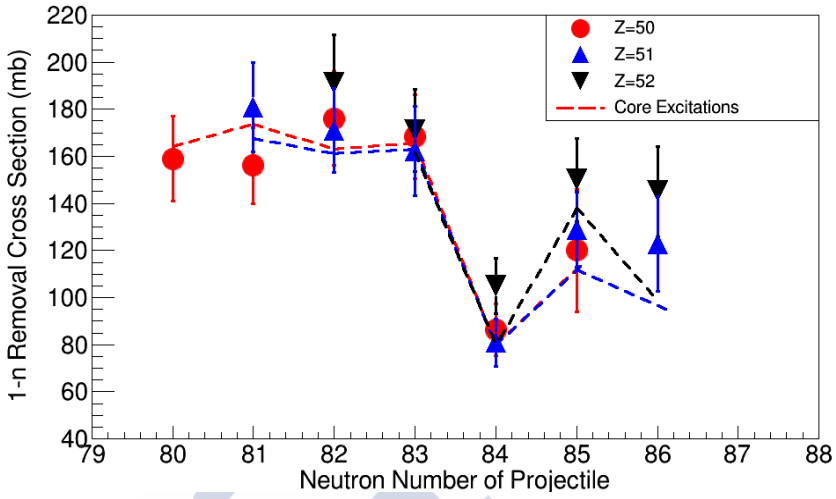

Figure 4.14: *Comparison between the measured one-neutron removal cross sections around the double-shell closure with model calculations. Tin (red dots), antimony (blue triangles) and telurum (black triangles) with neutron numbers between N= 80 and N =86 are shown. The red, blue and black lines (line colours are refered to colours chosen to represent each element) represent the model calculations based in core excitations performed in this work.*

ons are built from adjusted parametrizations to experimentally known cross sections [106, 107].

To investigate the effect of the pion production/absorption in one-nucleon knockout reactions we compared the result obtained with the standard code (pion re-absorption considered) with the calculations obtained neglecting the probability of absorbing the pion produced in inelastic processes. The result obtained suggested that the effect of NN inelastic collisions in one-nucleon knockout reactions of medium-mass nuclei with light targets at energies around 1GeV/A is found to be around 1-2% of the final one-nucleon removal cross section. As the collision occurs in the periphery of the nucleus, the pion absorption probability is very low. As an example, for ^{132}Sn the difference between both calculations is just 2.5 mb and can be neglected.

4.4.3 Discussion

Figure 4.14 shows the comparison between the measured one-neutron removal cross sections for tin, antimony and telurum in the region of the double-shell closure with the model calculations described in the previous section.

The calculated one-neutron removal cross section σ_{1n} showed in figure 4.14 takes into account the different contributions leading to this reaction channel and is calculated as follows:

$$\sigma_{1n} = \left(\sigma_{1n}^{INCL} \cdot P_{1n}^{Surv}\right) + \sigma_{1n}^{GDR} + \sigma_{1n}^{IGQR} \tag{4.3}$$

Where σ_{1n}^{INCL} is the pure one-neutron knockout cross section calculated with INCL, σ_{1n}^{GDR} and σ_{1n}^{IGQR} are the GDR and IGQR contributions and P_{1n}^{Surv} is the survival probability of the knockout-residue against nucleon emission. Those events that come from the excitation of collective nuclear modes are already de-excited and they contribute directly to the one-neutron removal channel.

Table 4.2 shows the measured and calculated one-neutron removal cross sections showed in figure 4.14. The reduction factor R_S takes into account the deviation of the theoretical prediction from the experimental value and is defined as $R_S = \sigma_{1n}^{exp}/\sigma_{1n}^{th}$. Except from ^{136}Te, ^{138}Te, ^{137}Sb and ^{136}Sb all the results show a deviation below 10%.

Isotope	σ_{1n}^{exp} (mb)	σ_{1n}^{th}(mb)	R_S	Isotope	σ_{1n}^{exp} (mb)	σ_{1n}^{th}(mb)	R_S
^{135}Sn	120(24)	112	1.07	^{135}Sb	84(7.0)	79	1.05
^{134}Sn	86(8.5)	80	1.08	^{134}Sb	162(13)	163	0.99
^{133}Sn	168(9.0)	164	1.02	^{133}Sb	171(11)	161	1.06
^{132}Sn	176(11)	162	1.08	^{132}Sb	181(11)	167	1.08
^{131}Sn	156(8.0)	173	0.90	^{138}Te	145(23)	98	1.47
^{130}Sn	159(9.0)	163	0.97	^{137}Te	144(17)	137	1.05
^{137}Sb	123(17)	96	1.28	^{136}Te	105(10)	79	1.32
^{136}Sb	128(12)	111	1.15	^{135}Te	171(23)	161	1.06

Table 4.2: *Measured and calculated cross sections showed in figure 4.14. The deviation of the theoretical value from the experimental one is evaluated through the reduction factor* $R_S = \sigma_{1n}^{exp}/\sigma_{1n}^{th}$

The different contributions to the one-neutron removal cross section of ^{132}Sn are listed in table 4.3; where first are listed the contributions to the production of the A-1 pre-evaporation core, ^{131}Sn*, with an overall contribution of 269 mb. Among the three contributions, an 80% comes from direct knockout, a 17% comes from the IGQR excitation and just a 3% from the GDR excitation. Then, the contributions to the A-2 reaction channel coming from the de-excitation of the ^{131}Sn* remnant are listed just below. The overall evaporation cross section is 109 mb, with a 40% fraction due to particle-hole excitations and the remaining 60% due to final state interactions.

Comparing figure 4.14 with figure 4.9 is clear that INCL+ABLA07 fails on describing the structural effects observed at N=84 while our improved calculations describe with high accuracy all the measured cross sections. INCL calculates the excitation energy using particle-hole combinations with an armonic oscillator model. In our calculations, the excitation energy is also calculated from particle-holes combinations but including realistic values for the energy levels and advanced calculations on the removed neutron, taking into account radial correlations between orbitals and impact parameter. The single-particle spectroscopic factors in this region are close to unity as it has been measured for ^{133}Sn in Ref.[108] and predicted for ^{132}Sn in Ref.[109]. Due to this, we assumed that all the orbitals below the gap are fully occupied due to the strong magicity of ^{132}Sn. Thus, performing a more realistic calculation of the excitation energy of the A-1 fragment, incorporating a more realistic description of the nuclear structure, allow us to conclude that the knockout process of loosely bound nucleons seems to be rather well understood, at least for this region of the chart of nuclides.

A-1 production; $^{132}\mathrm{Sn} \rightarrow {}^{131}\mathrm{Sn}^*$

σ_{1n}^{INCL} (mb)	σ_{1n}^{GDR} (mb)	σ_{1n}^{IGQR} (mb)
216	6.54	46.5

A-2 production; $^{131}\mathrm{Sn}^* \rightarrow {}^{130}\mathrm{Sn}$

σ_{2n}^{P-H} (mb)	$\sigma_{2n}^{F_FSI}$ (mb)
44	62

Table 4.3: *Different contributions to the one-neutron removal cross section of ^{132}Sn.*

4.5 One-proton knockout

One-proton removal cross sections were measured for isotopes of three different elements around the double-magic ^{132}Sn nuclei. Protons in very-neutron rich nuclei are deeply bound. In fact, the proton separation energy is around a factor of two bigger than the neutron separation energy for the same isotope.

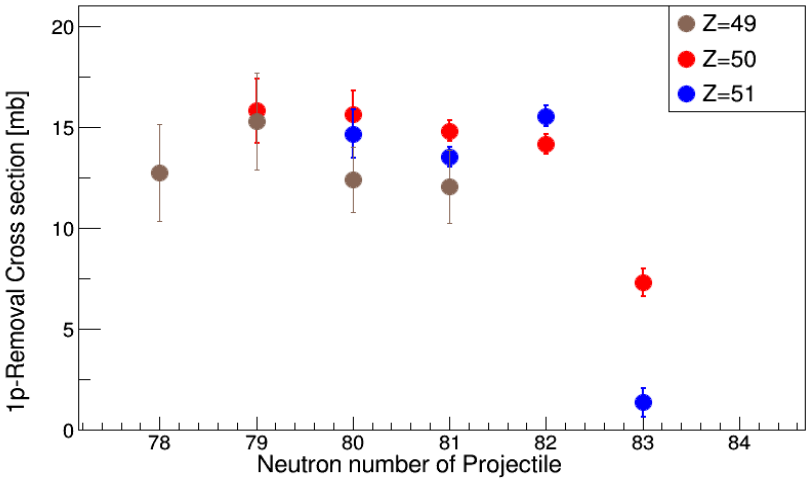

Figure 4.15: *One-proton removal cross section as a function of the neutron number of the projectile for the different elements measured in this work.*

Figure 4.15 shows the one-proton removal cross sections obtained in this work as a function of the neutron number of the projectile. It can be observed that the measured cross sections are of the order of the tens of mb, which is almost an order of magnitude smaller than the measured one-neutron removal cross sections measured (figure 4.4). This behavior can be partially explained considering the strong proton-neutron asymmetry of the measured nuclei. For example, ^{132}Sn has 1.65 more neutrons than protons which makes more probable to remove a neutron than a proton. This behavior was already studied in [32]. However, other effects such as neutron skins may be also responsible for this difference in cross sections.

However, it is clear in figure 4.15 that these cross sections still show some structural effects. When we cross the N=82 shell closure, an important decrease in cross section is observed, similar to the one observed in the one-neutron removal measurements. In this case, the decrease is observed in N=83 instead of N=84, due to the neutron separation energy of the Z-1 fragment produced in the reaction (see figure 4.7). The key point is that the effect is seen for both neutron- and proton- removal channels for the same number of neutrons of the daughter nucleus, N=83. The proton removal channel from a projectile with N=83 neutrons produces a fragment with the same number neutrons while to produce a fragment with 83 neutrons in the neutron-removal channel one needs an N=84 projectile.

Figure 4.15 shows a rather flat cross section distribution for isotopes with $N \leq 82$. As it was explained in the previous section, this can be easily

understood through the competition between excitation energy and neutron separation energy. After the shell closure, the nucleon emission threshold of the daughter nucleus decreases, favoring the nucleon emission in the de-exctiation stage and lowering the cross section. This effect is observed in figure 4.15 where two points were measured for N=83 nuclei. The red point corresponds to the ^{133}Sn(^{9}Be,p)^{132}In reaction where a 46% decrease is observed and the blue one to the ^{134}Sb(^{9}Be,p)^{133}Sn, where a 86% supression of the cross section is detected.

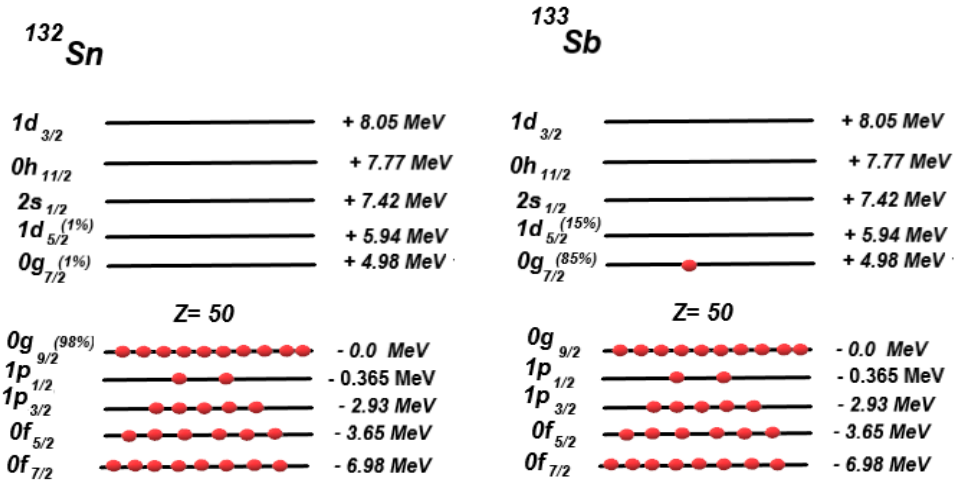

Figure 4.16: *Simple representation of the proton level scheme for ^{132}Sn and ^{133}Sb. The levels organization and the energies are taken from [99] except from the energy of the $1p_{1/2}$ which has been taken from [101]. The energies are related to the $0g_{9/2}$ level. The percentages shown for some orbitals represent the fragmentation of the single-particle strength of the valence protons to higher orbitals calculated by Angela Gargano et al.*

The difference between the tin and the antimony isotopes at N=83 is interpreted as due to the presence of the Z=50 shell closure. Figure 4.16 represents the level scheme of the protons for both elements. The levels organization and energies are taken from Ref.[99] except from the energy of the $1p_{1/2}$ which has been taken from Ref.[101].

In the case of tin isotopes, protons are removed from orbitals close to the Fermi level and the induced excitation energy is relatively low. However, for antimony isotopes, all the protons but the valence one are located below the Z=50 gap and removing any of these protons would induce a larger amount of excitation energy.

Figure 4.15 shows how the proton knockout cross section of N=83 isotones

is sensitive to both the neutron and the proton shell gaps. Surprisingly the cross sections for isotopes below N=83 do not show any sensitivity to the Z=50 shell gap, as the results for tin and antimony isotopes are relatively similar.

4.5.1 Model calculations

The same model used in section 4.3 to describe the one-neutron knockout process was used for calculating one-proton removal cross sections. Here, no contribution of initial state interactions are included. Whenever this occurs, the system emits the most energetically favored nucleon species, in this region neutrons have lower separation energies and thus it is more favored to emit a neutron than a proton. Moreover, final state interactions are very similar for the neutron and proton knockout process.

A realistic shell-model calculation was performed by professor *A. Gargano*, in order to determine the redistribution of the single-particle strength above the Fermi level. The calculations were done over a ^{88}Sr core with the valence protons occupying the four orbits $1p_{1/2}$, $0g_{9/2}$, $0g_{7/2}$ and $1d_{5/2}$ and the valence neutrons occupying the $0g_{7/2}$, $1d_{5/2}$, $1d_{3/2}$, $2s_{1/2}$ and $0h_{11/2}$ orbits. The shell-model Hamiltonian (the one- and two-body components) were microscopically derived by means of the many-body perturbation theory [110, 111].

The results of the calculation regarding the proton occupation probabilities for the different isotopes is shown in the appendix and are included in our model. The calculations showed a rather small probability (1-2%) for indium and tin isotopes to have protons in the next available level that would be above the shell gap. For antimony isotopes, an average probability of 15% for the valence proton to occupy the next level ($1d_{5/2}$) is obtained for the even-odd isotopes. The result obtained for even-even isotopes show a low probability (2%) for the valence proton to occupy the next orbit.

4.5.2 Short-range correlations in nucleon-knockout cross sections

Figure 4.17 shows the comparison between the measured one-proton removal cross sections and the calculations. Contrary to the neutron knockout, an overall overestimation of the cross section for all the isotopes is obtained, being bigger for indium and tin than for antimony isotopes. The strong even-odd effect showed by the antimony isotopes is probably due to the same effect reported in the neutron separation energies in this region (see figure 4.7) and the energy assumed for the protons single-particle levels.

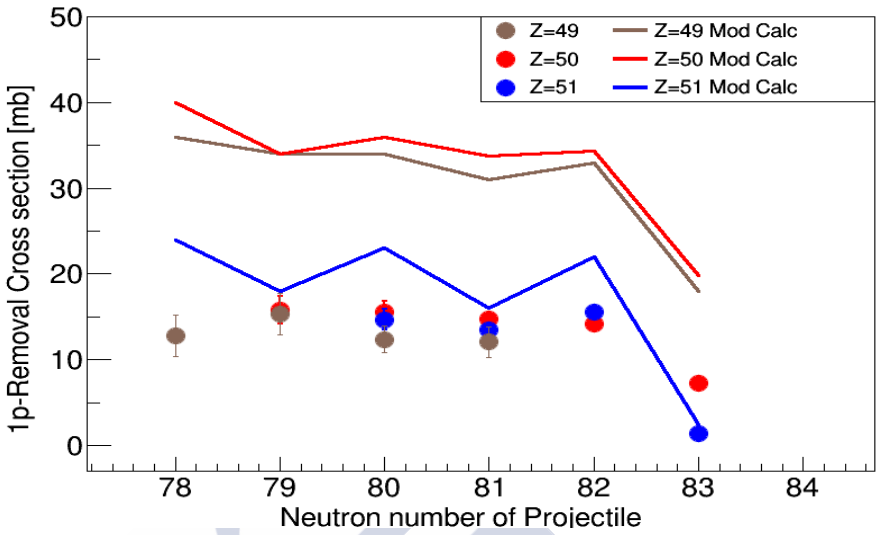

Figure 4.17: *Calculations and results for one-proton removal cross section for Z=49 (brown), Z=50 (red) and Z=51 (blue) isotopes. Filled circles are used to represent the experimental measurements and model calculations are showed as solid lines.*

Moreover, figure 4.17 shows a strong deviation between the calculations for isotopes with $Z \leq 50$ and for isotopes with $Z > 50$. It is seen how the calculations for elements with a number of protons below the Z=50 shell gap are systematically larger than those for elements with a number of protons larger than 50. This difference is not observed in our experimental results, where the one-proton removal cross sections for indium, tin and antimony are relatively similar to each other. The mean excitation energy induced by the proton knockout in Z=51 isotopes is in average 3.75 MeV larger than in Z=50 and Z=49 isotopes. In absolute terms, this means an increase of 21%.

Figure 4.18 shows the excitation energy spectrum for an A-1 residue of a ^{133}Sb(^{9}Be,p)^{132}Sn proton knockout reaction with the neutron separation energies for ^{132}Sn and ^{131}Sn indicated by the black and red lines, respectively. The observed peaks are the contribution from the different single-particle orbitals. It is seen how the ^{131}Sn neutron separation energy lies in the middle of the peak corresponding to the knockout from a $1p_{1/2}$ orbital. On the contrary, the neutron separation energy of ^{132}Sn is located after the peak. This makes that the survival probability of the ^{132}Sn knockout-fragment to be larger than one of the ^{131}Sn knockout residue.

However, the only single-particle energy level measured in this region is the $1p_{1/2}$ level with respect to the $0g_{9/2}$ orbital, with a given energy difference

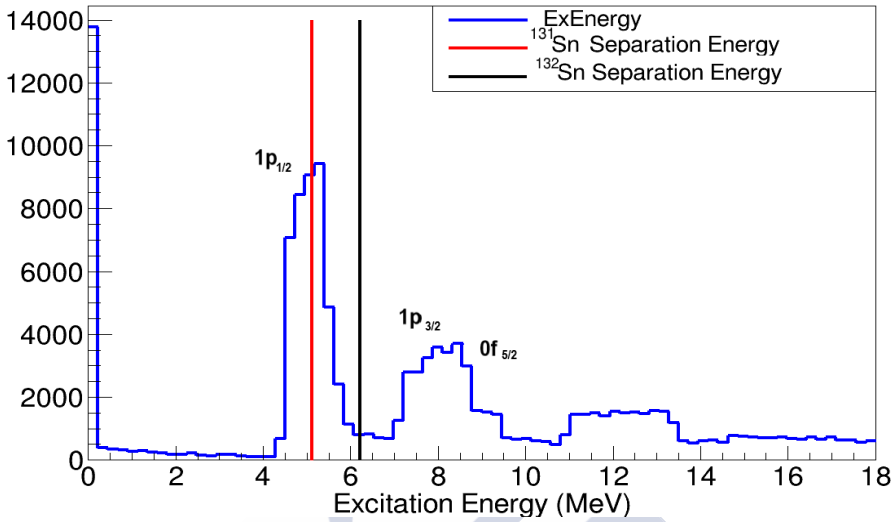

Figure 4.18: *Calculated excitation energy spectrum for the one-proton knockout residue produced in the reaction $^{133}Sb(^{9}Be,p)^{132}Sn$ proton knockout reaction. The neutron separation energies for ^{132}Sn and ^{131}Sn isotopes are shown as black and red lines, respectively. The peaks in the spectrum represent the contribution from the different orbitals.*

of 0.365 MeV [101]. The position of the $1p_{3/2}$ and $0f_{5/2}$ levels are not known as well as the energy of the Z=50 gap. With the values we assigned to these levels, the even-odd effect of the antimony isotopes is clearly overestimated. This could be a hint of an incorrect assignment of the single-particle energies to the orbitals.

Figure 4.19 is similar to figure 4.17 but the proton orbitals has been modified. The energy difference between the $0g_{7/2}$ and $0g_{9/2}$ orbitals is now taken as 3.8 MeV. The reduction of the Z=50 shell gap has already been predicted in Ref.[112]. where they calculated an energy difference of 4.2 MeV. However, an even stronger reduction up to 3.8 MeV would be possible according to Ref.[113] The position of the $1p_{1/2}$ level with respect to the $0g_{9/2}$ is still being the same 0.365 MeV. Ref.[101] concluded that the maximum energy difference between the $1p_{1/2}$ and $1p_{3/2}$ would be of 1 MeV. We assumed precisely that magnitude. The position of the $0f_{5/2}$ orbital is also not known, for this calculation we assumed a energy difference of 2.6 MeV with respect to the $1p_{3/2}$ orbital. These changes in the proton level scheme do not affect the calculated proton knockout cross sections for tin and indium isotopes. As there is no energy gap for those isotopes, the orbitals discussed here are way below the nucleon emission threshold.

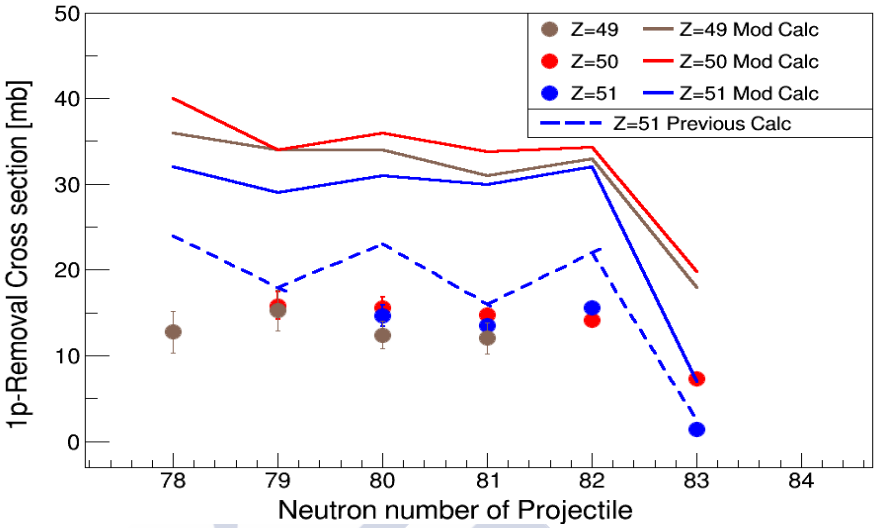

Figure 4.19: *One-proton removal cross section for Z=49 (brown), Z=50 (red) and Z=51 (blue) isotopes. Filled circles are used to represent the experimental measurements and model calculations are showed as solid lines. The blue dashed lines represent the calculation for Z=51 isotopes with the proton levels scheme taken from [99].*

Figure 4.19 shows how the proton knockout cross section for antimony isotopes is strongly dependent on the proton level scheme. It is clear that with the single-particle energies above described, the cross section difference between tin and indium and the antimony isotopes and the strong even-odd effect has now disappeared in better agreement with the measured cross sections. However, the cross sections are still overestimated by the calculus. A more precise calculation would be possible with an accurate determination of the proton single-particle energies. However, at this moment it seems that a reduction in the Z=50 shell gap, as the one proposed here, seems to be in better agreement with our calculations.

The measured and calculated one-proton removal cross sections are presented in table 4.4 and compared through the reduction factor R_S. It is seen that a strong reduction of the cross section is obtained having an average value of 0.38, 0.42 and 0.40 for indium, tin and antimony respectively. These results would be in good agreement with the results obtained in Ref.[5], obtaining a high reduction factor for the removoal of well-bound nucleons.

The overprediction of the measured proton knockout cross sections could be a hint of an additional source of excitation energy that is affecting the survival probability of the proton knockout fragment. Final state interactions

Isotope	σ_{1p}^{exp} (mb)	σ_{1p}^{th}(mb)	R_S	Isotope	σ_{1p}^{exp} (mb)	σ_{1p}^{th}(mb)	R_S
^{133}Sn	7.31(1)	20	0.36	^{128}In	15.2(2)	34	0.44
^{132}Sn	14.5(1)	34	0.42	^{127}In	12.8(3)	36	0.35
^{131}Sn	14.8(1)	33	0.44	^{134}Sb	1.35(1)	6.3	0.21
^{130}Sn	15.6(1)	35	0.44	^{133}Sb	15.5(1)	32	0.48
^{129}Sn	15.8(2)	34	0.46	^{132}Sb	13.5(1)	30	0.45
^{130}In	12.1(2)	31	0.39	^{131}Sb	14.6(1)	31	0.47
^{129}In	12.4(2)	34	0.36				

Table 4.4: *Measured and calculated cross sections showed in figure 4.20. The deviation of the theoretical value from the experimental one is evaluated through the reduction factor* $R_S = \sigma_{1n}^{exp}/\sigma_{1n}^{th}$

and NN inelastic collisions were already taken into account and satisfactorily benchmarked with the results for the neutron-removal cross sections. Therefore an additional process is required to explain this difference.

Proton-neutron pairs forming short-range correlated pairs might be a possible explanation for this effect. According to Ref.[10], short-range correlated nucleons have a large relative momentum ($k_{rel} > k_f$) and a small center of mass momentum ($k_{tot} < k_f$) where k_f is the Fermi momentum of the system. In addition, as it is described in [11], when a high-momentum nucleon is removed from the nucleus, the second nucleon of the correlated pair is effectively removed from the nucleus as the potential between both nucleons is destroyed instantaneously. Then, this mechanism contributes to reduce the survival probability of the A-1 core leaving an A-2 core barely undisturbed.

There is also strong evidence that the majority of the correlated pairs are formed by neutron-proton pairs. Recent results obtained by the CLAS collaboration and discussed in chapter 1 (see section1.5) measured that fraction of high-momentum protons to high-momentum neutrons is constant with unity for a wide range in isospin. As a consequence, in asymmetric nuclei, the relative fraction of high-momentum nucleons is bigger for the minority specie than for the majority. According to this, and following the results obtained in [12] the probability of finding high-momentum protons in very-neutron rich nuclei around ^{132}Sn is $\sim$30%. While the probability of finding a high-momentum neutron is around $\sim$15%.

This effect should be taken into account in our calculations for both the neutron-removal and the proton-removal cross sections by including the probability of finding high-momentum correlated proton-neutron pairs in the nucleus.

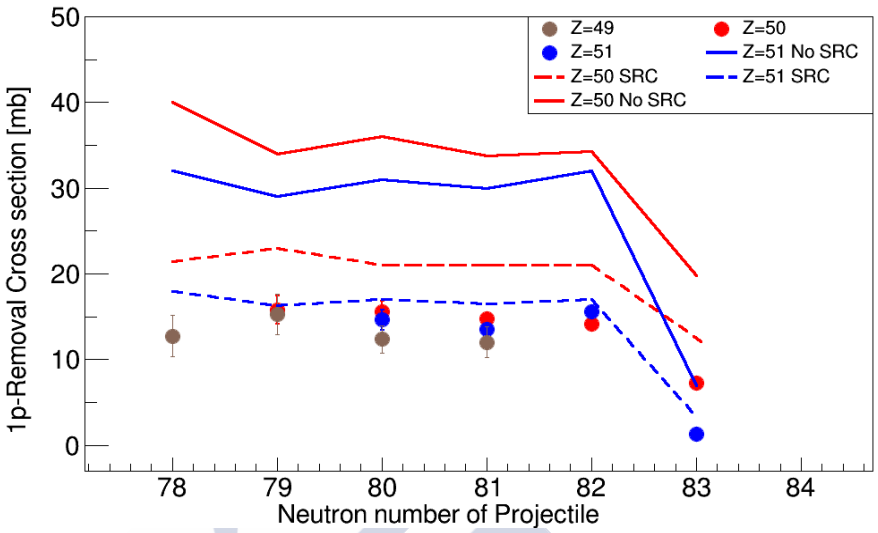

Figure 4.20: *Calculations and results for one-proton removal cross section for Z=49 (brown), Z=50 (red) and Z=51 (blue) isotopes. Filled circles are used to represent the experimental measurements. Model calculations with the probability of finding a high-momentum protons included are showed as dashed lines. Model calculations without short-range correlations are represented as solid lines.*

Figure 4.20 shows the comparison between the experimental proton knock-out cross sections and the calculations when the probability of having high-momentum protons is included. It is clearly shown that this effect reduces the deviation between the experimental and theoretical results.

The decrease in the proton-knockout cross sections due to the effect of short-range correlations might result in an increase in the cross section of the Z-1, N-1 reaction channel.

Figure 4.21 shows the the 1proton-Xneutrons removal reaction-channels of the ^{132}Sn(^{9}Be) reaction as a function of the mass number of the fragmentation fragment. The red dots are taken from Ref.[90] and show the expected enhancement of the 1p1n removal channel with respect to the 1p removal. INCL+ABLA07 calculations are represented by the solid blue line. In this case the calculated one-proton knockout channel is larger than the one-proton one-neutron removal channel. Calculations with the model used in this work provide a better description of the data. The calculation without short-range correlated protons also overpredict the one-proton removal reaction channel. Finally, the calculation including short-range correlations (solid red lines) describes rather well both reaction channels, proving that the reduction of the one-proton removal channel due to the effect of short-range correlations

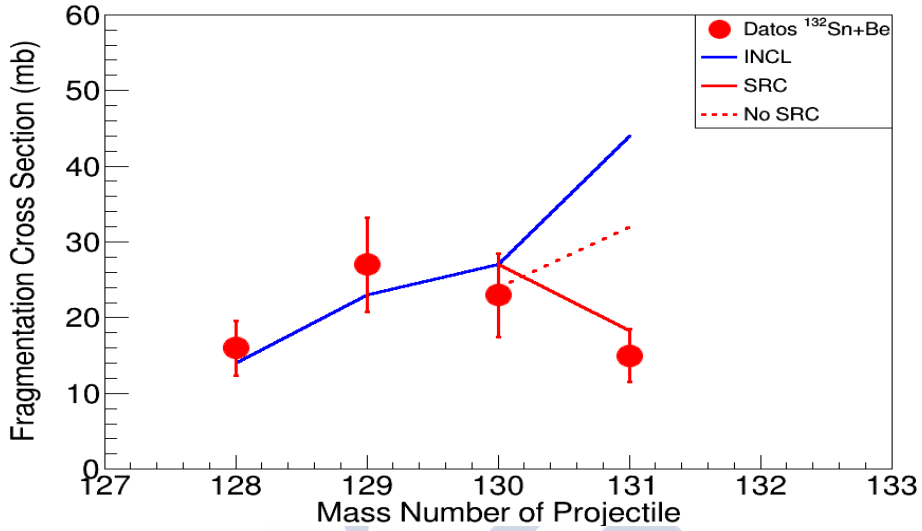

Figure 4.21: *Fragmentation of a ^{132}Sn tin isotope when colliding with a ^{9}Be target. The 1p, 1p1n, 1p2n and 1p3n fragmentation cross sections taken from Ref.[90] are shown as a function of the mass number of the fragment. INCL+ABLA07 calculations are represented as a blue line. Model calculations performed in this work are represented as red lines, the dotted red line does not include the effect of short-range correlations and the solid red lines takes into account this effect.*

induces an increase of the one-proton one-neutron removal channel.

Indeed, the effect of short-range correlations should be an universal trend. Figure 4.22 illustrates the effect of the evolution of short-range correlations with the neutron excess. The upper panel in the figure shows the measured one-neutron removal cross sections (blue dots) for the Z=50 isotopic chain and the results from Ref.[32] (black diamonds). The dashed line represents the calculation without including the effect of short-range correlations. Then, the solid blue line represents the evolution of the effect of the short-range correlations for neutrons along a large isotopic chain. As it is discussed in Ref.[12] the probability of finding high-momentum neutrons decreases with the neutron-proton asymmetry of the nucleus. Around ^{132}Sn, with an N/Z value of 1.65, around 15% of the neutrons will be in short-range correlated pairs.. Thus, the effect on the one-neutron removal cross section is not significantly important. However, the probability of finding a high-momentum neutron in the neutron-defficient region grows up to ∼20% for the ^{110}Sn.

The lower panel shows the same effect but for the proton-removal channel. Here, the probability of finding a correlated proton increases with the neutron excess, being very remarkable for the very-neutron rich region around ^{132}Sn.

Here, an estimation of a ∼30% probability of having a high momentum proton is given in Ref.[12]. Then, this probability decreases when moving to the neutron-defficient isotopes, finding a ∼20% for the ^{110}Sn. In this figure, the red dotted line represent the calculations without short-range correlations, the solid red line represent the calculations with the probability of having high-momentum protons varying with the neutron-proton asymmetry and the dotted line represent these calculations but including a fixed probability of 20% of having high-momentum protons for all the isotopes.

Its is clearly seen how the proton-removal cross sections for the most neutron-defficient isotopes (Ref.[32] (black diamonds)) are rather well described with just a 20% probability of having short-range correlations probability. However, the results on the very-neutron rich side shows that a 20% probability is not enough to described the measured cross section.

In summary, the measured one-neutron removal cross sections are rather well described by the model calculations used in this work. I has been proved that a realistic description of the nuclear structure is needed to have an accurate calculation of the removal channel. The relative contributions of initial- and final-state interactions to the measured one-neutron knockout fragment seems to be significantly important, as they provide a rather large fraction of the measured cross section.

However, same model calculations overpredict the one-proton removal channel by 60%. The role that short-range correlations play in nucleon-removal reactions has been investigated, finding that a significant reduction of the calculated cross section is obtained when including the probability of having short-range correlated nucleons inside the nucleus. Although further investigation is needed to understand the effect of short-range correlations, we provide evidence on the impact that these correlated pairs would have in this particular reaction channel.

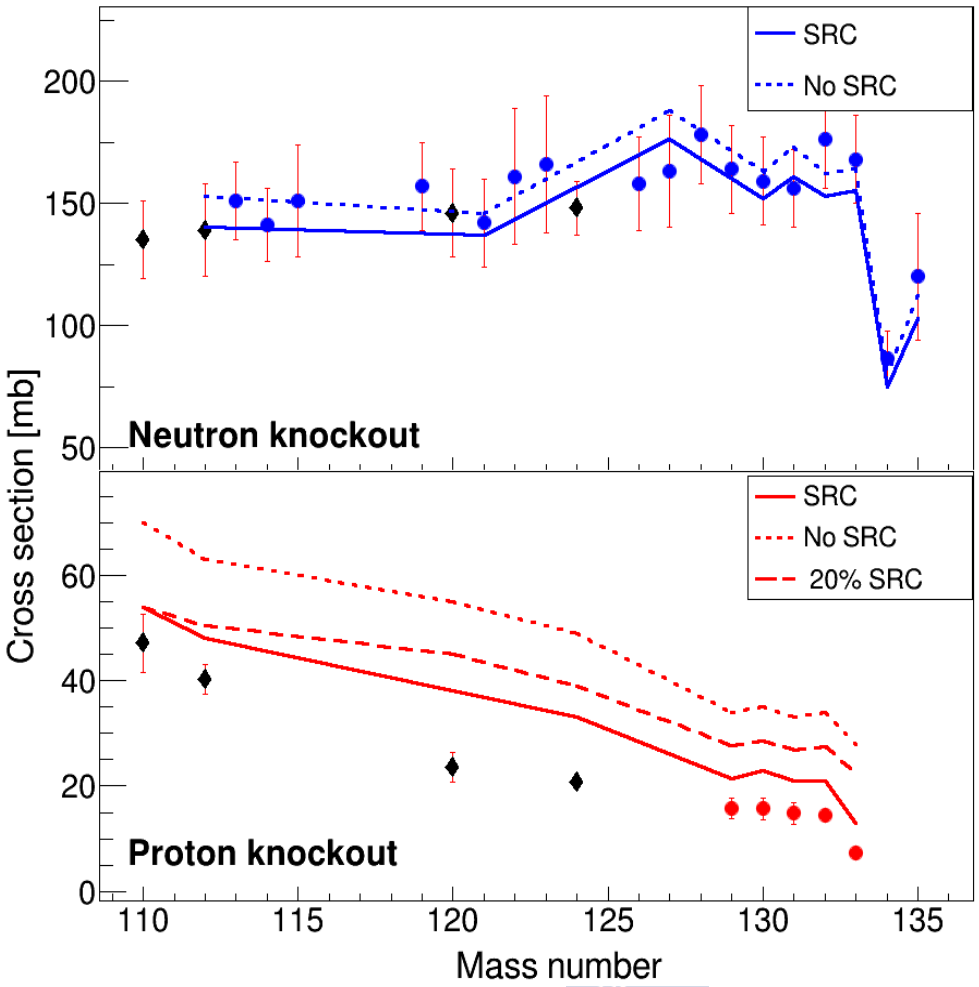

Figure 4.22: *The upper panel shows the measured one-neutron removal cross sections for tin isotopes as a function of the mass number. The dotted blue line represents the results of the model calculations described in this chapter without including the effect of SRC. The solid line represents same calculations but including the effect of SRC. The lower panel shows the measured one-proton removal cross sections for tin isotopes as a function of the mass number. The dotted line represents the results of the model calculations described in this chapter without including SRC. The solid line represent same calculations but including the probability of finding high-momentum nucleons following the observed evolution in Ref.[12]. The dashed line represents same calculation with a fixed 20% probability of finding a high-momentum proton.*

Conclusions

In this work, we have measured total reaction and single-nucleon removal cross sections for a wide variety of medium-mass neutron rich nuclei using the FRS spectrometer at the GSI facility in Darmstadt, Germany. In order to produce long isotopic chains of medium-mass nuclei, two different beams and two different reaction mechanisms were used. Fission of a 950 MeV/A ^{238}U beam enhanced the production of very neutron-rich nuclei in the region of ^{132}Sn. Then, the fragmentation of a 1200 MeV/A ^{132}Xe beam was used to produce less neutron-rich nuclei. As the reaction was performed in inverse kinematics and relativistic energies, forward focusing of the reaction fragments made it possible to analyze them using the FRS magnetic spectrometer.

In this experiment, the FRS was used as two-independent magnetic spectrometers. The first half of the FRS allowed us to identify the nuclei in the cocktail beam produced with the above described mechanisms. Then, the second part of the FRS was used to separate and identify the reaction fragments produced as a result of the interaction of the cocktail beam with a 2591 mg/cm^2 ^{9}Be target placed at the intermediate focal plane of this spectrometer. Using the two-step reaction mechanism, around 150 medium-mass nuclei were produced and investigated.

Total reaction cross sections were measured for 51 isotopes of 5 different elements (Z=48-52) and were investigated in the framework of the Glauber's theory. The calculated cross sections systematically overestimate the measured cross sections by a $\sim$10% in average. An exhaustive investigation of this deviation derived on the conclusions that the combined effect of the target thickness uncertainty ($\sim$3.5%) and the application of the optical limit approximation in Glauber-type calculations which reduces the calculated cross section by a factor $\sim$3%, could partially explain this difference, although further investigations are required.

However, important conclusions have been obtained studying the relative behavior of the different measured isotopic chains. The measured cross sections present two different trends when sorted with the neutron number.

Glauber calculations based on HFB radial distributions predict such a change in the evolution of the total reaction cross sections for nuclei with neutron number N>82. However, our measurements with tin isotopes show a smooth evolution of the cross section before N≤79, following the expected trend with $A^{1/3}$. Then, a stepper increase of the total reaction cross section is observed. This behavior is observed for the five isotopic chains investigated in this work. However, the neutron number for which the trend on the evolution of the cross section changes, depends on the atomic number. It is observed at N∼76 for Z=48, N∼77 for Z=49, N∼79 for Z=50, N∼81 for Z=51 and N∼83 for Z=52. This suggested that the evolution of the cross section for the most neutron-rich nuclei is mostly governed by the the neutron-proton asymmetry of the nucleus. In conclusion, before N/Z≈1.6 the cross sections follows the expected evolution of the cross section with $A^{1/3}$. After N/Z≈1.6 the cross section increases with the neutron excess.

Moreover, the region where a stepper increase of the cross section is observed presents large differences in cross section between isotones. As a matter of fact, it is observed that isotones with lower atomic numbers present larger cross sections. This means that the total reaction cross section for ^{131}In is larger than the cross section for ^{132}Sn even though the last one is bigger in mass. This effect could be attributed to the growth of neutron skins in this region. The neutron skin grows with the neutron-proton asymmetry of the nucleus and is related with large neutron density distributions which increase the size of the nucleus. The neutron-proton asymmetry is larger for ^{131}In than for ^{132}Sn, which means that a thicker neutron skin is expected in ^{131}In.

Single-nucleon removal cross sections were measured for more than 70 isotopes in the medium-mass neutron-rich region. The results were also investigated in the framework of the Glauber's theory with the latest version of the intranuclear cascade model. In addition, a self-developed code based on particle-hole excitations was used to calculate the excitation energy of the A-1 fragment and its subsequent de-excitation. A realistic description of the structure of the investigated nuclei was also considered. The contributions of initial- and final- state interactions and the effect of nucleon-nucleon short range correlations were taken into account.

One-neutron removal cross sections were measured for five different isotopic chains (Z=48-52). All the measured cross sections for N≤82 isotopes present rather similar values which are explained through the competition between the excitation energy gained in the nucleon removal process and the neutron separation energy of the A-1 fragment. After the N=82 shell closure, a drop in the one-neutron removal cross section is observed for the N=84 isotones. This is explained through the high-excitation energies induced by the

N=82 shell gap and the low neutron separation energies of the knockout fragment. A rather good agreement is found between the measured one neutron removal cross sections and model calculations. It has been shown that the role of initial and final state interactions play a very important role in the neutron-knockout mechanism.

One-proton removal cross sections were measured for three different isotopic chains (Z=49-51) for isotopes around ^{132}Sn. We measured one-proton removal cross sections only for 13 isotopes due to the transmission limitations of the FRS. The one-proton removal cross sections are $\sim$10 times lower than the one-neutron removal cross sections partially due to the neutron-proton asymmetry of the nucleus and neutron-skin effects.

Isotopes with neutron number N$\leq$83 show rather similar cross sections. This is explained with the same arguments exposed for the neutron removal cross sections. A drop in the cross section is observed for N=83 isotones due to the presence of the N=82 shell gap. In addition, a difference is observed between the N=83 antimony and the N=83 tin isotopes due to the presence of the Z=50 shell gap.

The same model used to describe satisfactorily the neutron-knockout mechanism overestimates the proton-knockout cross sections by a factor $\sim$2 in average. Long-range correlations between nucleons leading to a redistribution of the single-particle strength were investigated finding this effect could only explain a small fraction of the missing cross section. In fact, the probability to occupy states above the Fermil level for one of the protons of a tin isotope was less than a 2%.

The role that short-range correlations between nucleons plays in the single-nucleon knockout mechanism was then investigated. The probability of finding short-range correlated neutron-proton pairs was included in our calculations with the condition that whenever one of this nucleons is removed its correlated partner will be automatically ejected. This effect reduces the calculated cross section for the proton-knockout mechanism by around $\sim$30%. In addition, the included probability of finding high momentum nucleons varies with the neutron excess following the results obtained in Ref.[12]. This effect is needed to describe the less-neutron rich tin isotopes like ^{110}Sn.

The one-neutron removal channel is also affected by short-range correlations. However, as it is described in Ref.[12], the probability of finding high-momentum neutrons in very neutron-rich nuclei is lower than finding high-momentum protons. This effect was taken into account in our calculations but the impact on the final one-neutron removal cross sections iis in the order of 10% which is inside the uncertainty of the measurement.

In conclusion, short-range correlated nucleons seem to play an impor-

tant role in the single-nucleon knockout mechanism. Indeed, single-nucleon knockout cross sections are only sensitive to non-correlated nucleons. Even though further investigation is needed to understand if short-range correlations are responsible of the large overprediction of the removal of well-bound nucleons, it is clear than an important decrease of the calculated cross section is obtained when these correlations are taken into account.

USC
UNIVERSIDADE
DE SANTIAGO
DE COMPOSTELA

Chapter 5

Resumen en castellano

El trabajo aquí presentado se centra en las medidas de secciones eficaces de arranque de un nucleón y secciones eficaces totales de reacción de núcleos de masa intermedia ricos en neutrones. Estas medidas fueron realizadas en un experimento llevado a cabo en el centro de investigación alemán *GSI Helmholtz Centre for Heavy Ion Research*, situado en la ciudad de Darmstadt, entre Noviembre y Diciembre de 2006.

Las reacciones nucleares, estudiadas en cinemática inversa, en las que un solo nucleón del proyectil es arrancado al colisionar con un blanco, han sido extensamente utilizadas a lo largo de las últimas décadas como herramienta para obtener información sobre la estructura de núcleos alejados del valle de la estabilidad [25, 26]. Los principales observables en este tipo de reacciones nucleares son la sección eficaz, exclusiva o inclusiva, y la distribución de momento del núcleo A-1. En una reacción de este tipo, el nucleón arrancado deja un hueco en la distribución de estados ocupados del proyectil, produciendo diferentes estados excitados del fragmento A-1. Los rayos-γ asociados a la desexcitación del fragmento A-1 se utilizan para medir la sección eficaz exclusiva de los diferentes estados excitados. La suma de todas las secciones eficaces exclusivas es la sección eficaz inclusiva, una medida directa de la probabilidad de supervivencia del fragmento A-1 que proporciona información sobre los diferentes mecanismos que influyen en la reacción.

La probabilidad de supervivencia del fragmento A-1 está directamente relacionada con la energía de excitación inducida debido a excitaciones partícula-hueco y la energía de separación de neutrones o protones del fragmento producido en la reacción. Sin embargo, otros mecanismos pueden contribuir a la producción final del fragmento A-1. Por un lado, la excitación de resonancias electromagnéticas o nucleares por encima del umbral de emisión de nucleones [16, 17] contribuyen al mismo canal de reacción, aumentando la producción del fragmento A-1. Por otro lado, el nucleón arrancado puede sufrir múltiples

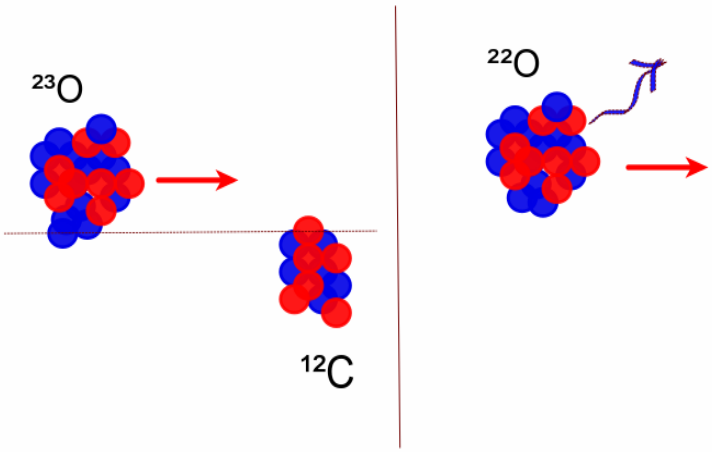

Figure 5.1: *Representació esquemática del arranque de un nucleón en la colisión de un núcleo de ^{23}O con un blanco de ^{12}C.*

colisiones con otros nucleones antes de salir del núcleo. Este efecto aumenta la energía de excitación del fragmento de reacción, disminuyendo su probabilidad de supervivencia.

A lo largo de los últimos años, diferentes experimentos enfocados a la medida de secciones eficaces de arranque de un nucleón han dado con un resultado similar. Las secciones eficaces calculadas basándose en el modelo de Glauber [20] para describir el mecanismo de reacción y en el modelo de capas para describir la ocupación de los orbitales, sobreestiman el valor medido. La desviación del valor calculado con respecto al medido se determina a partir del factor de reducción, $R_s = \sigma_{exp}/\sigma_{th}$, del que se observa una dependencia con el nivel de asimetría neutrón-protón del núcleo [5]. Sin embargo, en los resultados obtenidos en experimentos recientes mediante reacciones de transferencia de nucleones [7, 8, 9] y quasi-free scattering $(p,2p)$ [6], la dependencia del factor de reducción con la asimetría del núcleo no ha sido observada.

Reciéntemente, resultados obtenidos mediante scattering de electrones a alta energía han demostrado la existencia de pares nucleón-nucleón correlacionados dentro del núcleo [10]. Estos pares de nucleones se caracterizan por tener un momento relativo mayor que el momento de Fermi del sistema ($k_{rel} > k_f$) y un momento en su centro de masas menor ($k_{tot} < k_f$) que el momento de Fermi. En su mayoría, los pares de nucleons correlacionados están formados por parejas neutrón-protón. La existencia de estos pares correlaciondos puede tener un determinado impacto en las medidas de secciones eficaces de

arranque de un nucleón. Tal y como esta descrito en Ref.[11], siempre que uno de los nucleones que forman parte de un par correlacionado es arrancado, el otro componente del par es automáticamente expulsado del núcleo. De esta forma, este mecanismo contribuiría a disminuir la sección eficaz observada experimentalmente. Ademá, el ratio entre neutrones y protones correlacionados es constante con la unidad para todos los núcleos estudiados, independientemente del isospin [12]. Como una consecuencia directa de este efecto, el número relativo de nucleones correlacioneados es mayor para los nucleones que están en minoría dentro del núcleo y, por lo tanto el efecto que tiene sobre la sección eficaz de arranque de un nucleón depende del nivel de asimetría del núcleo.

El otro mecanismo de reacción investigado en este trabajo es la sección eficaz total de reacción, la cual engloba cualquier tipo de interacción entre proyectil y blanco. Típicamente, se define como la suma de dos contribuciones, la sección eficaz total de los procesos de arranque de neutrones y de protones y la sección eficaz de interacción debido a procesos inelásticos, como la excitación de resonancias electromagnéticas o nucleares. Debido a la naturaleza de esta medida y todos los procesos que engloba, resulta un excelente punto de referencia para comprobar la fiabilidad de los diferentes modelos de reacción. Además, proporciona una medida indirecta sobre el tamaño del núcleo y una herramienta apropiada para investigar efectos de estructura en núcleos alejados de la estabilidad.

5.1 Descripción del experimento

El experimento se realizó en las instalaciones del GSI, en Darmstadt, Alemania. Combinando la fisión de un haz primario de ^{238}U con una energía de 950 MeV/A y la fragmentación de un haz de ^{132}Xe a 1200 MeV/A se produjeron largas cadenas isotópicas de núcleos de masa intermedia. Ambas reacciones se realizaron en cinemática inversa y a energías relativistas, de esta forma los fragmentos de reacción son emitidos hacia delante en ángulos muy pequeños y pueden ser analizados usando el espectrómetro magnético FRS. En la figura 5.2 se puede ver una visión esquemática de este espectrómetro magnético y de los detectores utilizados en este experimento.

Con el objetivo de determinar las secciones eficaces de interacción y de arranque de nucleones de los núcleos producidos, el FRS fue utilizado como dos espectrómetros independientes. Para obtener el valor de una sección eficaz, tanto el número de núcleos antes como después del blanco deben ser medidos. Para ello, en la primera parte se lleva a cabo la identificacón de los núcleos producidos mediante los mecanismos descritos en el párrafo

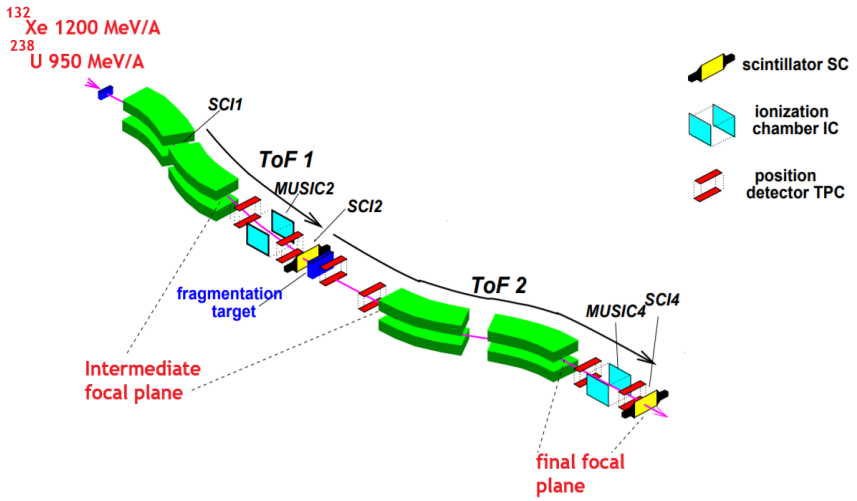

Figure 5.2: *Representació esquemática del FRS, el espectrómetro magnético utilizado en este experimento para analizar los núcleos de interés*

anterior. Luego, en el punto focal intermedio del espectrómetro se coloca un blanco secundario de berilio de 2591 mg/cm^2, para estudiar la interacción de los haces secundarios y medir las secciones eficaces investigadas en este trabajo. Por último, la segunda parte del FRS se utilizaa para identificar los fragmentos de reacción producidos debido a la interacción con el blanco.

5.2 Secciones eficaces totales de reacción

En este trabajo se midió la sección enficaz total de reacción para 51 núcleos diferentes de 5 elementos distinitos (Z=48-52) y se comparó con cálculos basados en el modelo de Glauber. Sistmáticamente, el cálculo sobrestima el valor medido de la sección eficaz en un ∼10%. El efecto combinado del error en la medida del blanco secundario de berilio (∼3.5%) y los límites del cálculo realizado, los cuales se basan en la aproximación del límite óptico del model de Glauber que sobreestima en un ∼3% el valor de la sección eficaz total calculada, pueden explicar una gran parte de esta desviación.

Sin embargo, este efecto no impide obtener conclusiones claras en cuanto a la evolución relativa de la sección eficaz total de reacción a lo largo de las distintas cadenas isotópicas investigadas en este trabajo. La figura 5.3 muestra la evolución de la sección eficaz total de reacción con el número de neutrones del proyectil. La línea laminada representa la evolución esperada de esta mangitud con la masa $A^{1/3}$.

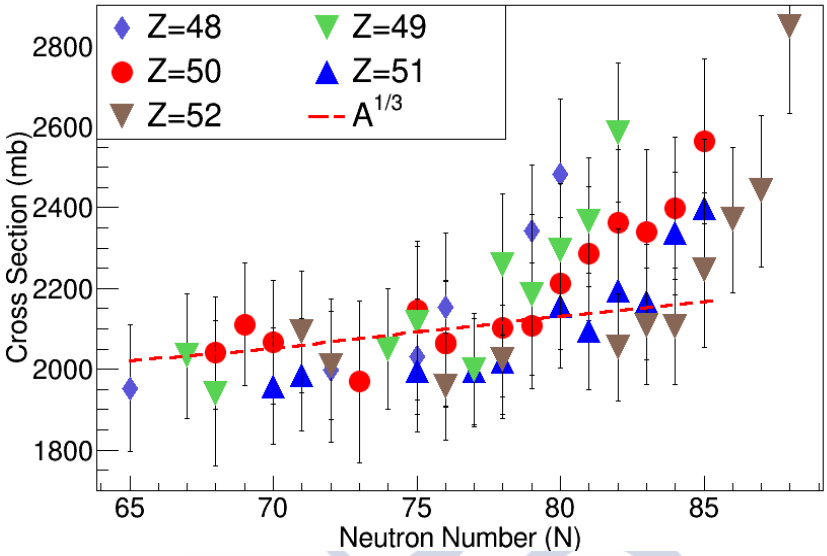

Figure 5.3: *Secciones eficaces totales de reacción medidas en este trabajo en función del número de neutrones del proyectil. La línea laminada representa la evolución esperada de la sección eficaz total de reacción con $A^{1/3}$.*

En la figura 5.3 se puede observar como la evolución de la sección eficaz con el número de neutrones del proyectil muestra dos tendencias claramente diferenciadas. Los núcleos menos ricos en neutrones siguen la evolución esperada de la sección eficaz con $A^{1/3}$. Sin embargo, los núcleos mas ricos en neutrones presentan una clara desviación de esta tendencia, con un aumento de la sección eficaz mucho más rápido. Además, de esta figura se puede sacar otra importante conclusión, el valor en número de neutrones para el cual la sección eficaz total de reacción empieza a desviarse del comportamiento esperado con $A^{1/3}$ depende del número de protones. Por ejemplo, para la cadena isotópica de estaños, a partir de N∼79 la tendencia cambia, sin embargo para el cadmio este cambio es observado en N∼76 y en los teluros para N∼83.

Además, la región en la que la evolución de la sección eficaz crece más rápidamente presenta importantes diferencias entre la sección eficaz total de reacción medida para diferentes cadenas isotónicas. Se puede observar como en una misma cadena isotónica, aquellos núcleos con un menor número atómico tienen una sección eficaz total de reacción mas alta. Por ejemplo, el ^{131}In y el ^{132}Sn tienen el mismo número de neutrones y aunque el segundo tenga un número másico más alto, tiene una sección eficaz total de reacción mas baja.

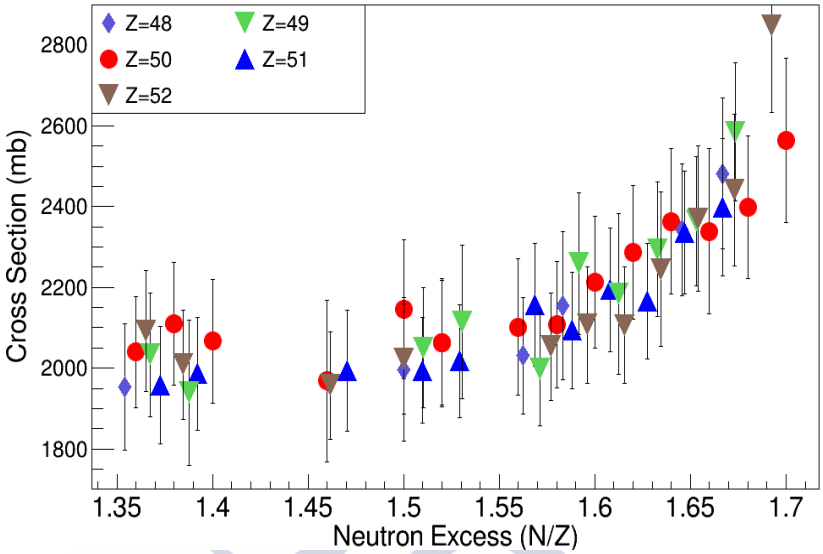

Figure 5.4: *Secciones eficaces totales de reacción medidas en este trabajo en función del exceso de neutrones del proyectil.*

Este efecto puede ser debido al desarrollo de pieles de neutrones en estos núcleos. El tamaño de la piel de neutrones depende en gran medida del exceso de neutrones de núcleo y tiene un importante efecto en el tamaño de este, ya que se manifiesta como un aumento espacial de la distribución radial de neutrones. El ^{131}In tiene un exceso de neutrones mayor que el ^{132}Sn por lo que se le asocia un tamaño mayor de la piel de neutrones que puede explicar el mayor valor de sección eficaz.

Este efecto nos lleva a concluir que la evolución isotópica de la sección eficaz total de reacción presenta dos claras tendencias que dependen del exceso de neutrones del núcleo. Aquellos núcleos medidos con un exceso de neutrones menor que N/Z$\sim$1.6, presentan una clara dependencia con la masa del núcleo, siguiendo la evolución esperada con $A^{1/3}$. Sin embargo, los núcleos con un exceso de neutrones mayor que N/Z$\sim$1.6 muestran una clara evolución con el exceso de neutrones del núcleo. La evolución de las secciones eficaces medidas con el exceso de neutrones del núcleo puede observarse en la figura 5.4.

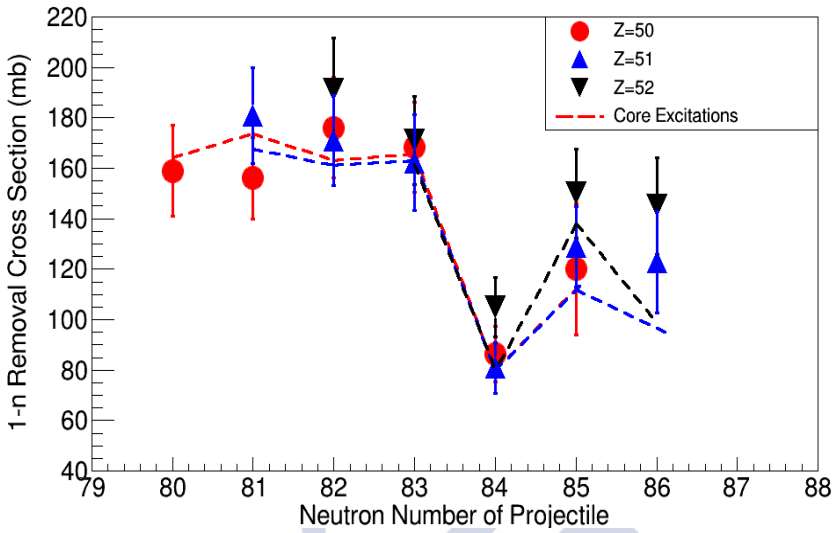

Figure 5.5: *Secciones eficaces de arraque de un neutrón para núcleos alrededor de la capa N=82 de diferentes elementos. Las líneas laminadas muestran el resultado del cálculo.*

5.3 Secciones eficaces de arranque de un nucleón

En este trabajo se midió la sección eficaz de arranque de un nucleón para más de 70 núcleos diferentes de 5 elementos distintos (Z=48-52). Los resultados se han estudiado mediante el modelo de Glauber, con la versión más reciente del modelo de cascada intranuclear. Además, la descripción de la energía de excitación del fragmento A-1 y su desexcitación se ha realizado mediante un código desarrollado durante la realización de este trabajo, basado en excitaciones partícula-hueco, en el que se incluye una descripción realista de la estuctura de los núcleos. La contribución al canal de reacción de la excitación de resonancias electromagnéticas y nucleares, así como el efecto de colisiones múltiples, colisiones inelásticas nucleón-nucleón y correlaciones de corto alcance entre nucleones, han sido tenidos en cuenta.

Las secciones eficaces de arranque de un neutrón para los núcleos con un número de neutrones menor o igual que 83 (N$\leq$83) presentan un valor similar. Este se explica mediante la competición entre la energía de excitación ganada en la colisión, y la energía de separación de neutrones del fragmento A-1. A partir de N=83, se observa una caída en el valor de la sección eficaz, común a los diferentes elementos estudiados en este trabajo. Debida a la presencia de la capa de neutrones N=82, la energía de excitación ganada

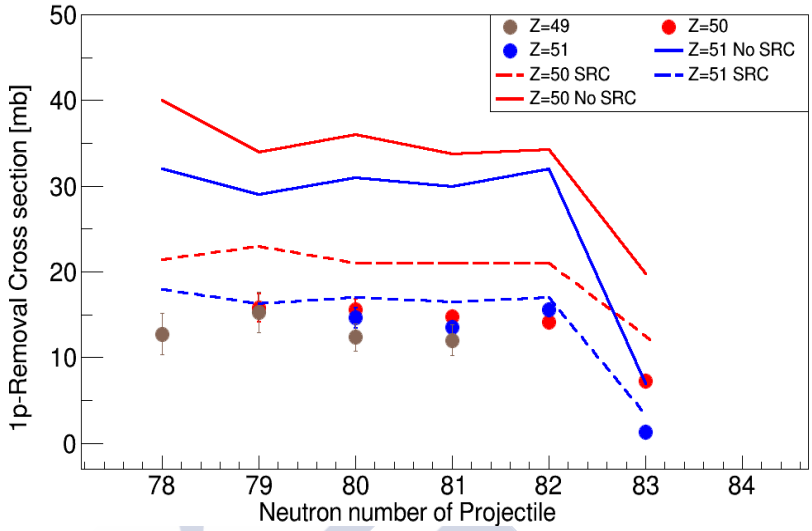

Figure 5.6: *Secciones eficaces de arraque de un protón de los núcleos investigados en este trabajo. Las líneas continuas muestran el resultado del cálculo sin la inclusió del efecto de correlaciones de corto alcance entre nucleones. Las líneas punteadas muestran la sección eficaz calculada con efectos de correlactiones de corto alcance entre nucleones.*

en el arranque de un neutrón en la colisión es mayor. Además, la energía de separación de neutrones se reduce para los núcleos con un número de neutrones mayor que 82. La combinación de ambos efectos resulta en una caida de la probabilidad de supervivencia del fragmento A-1 producido en la reacción, lo cual se traduce en una menor sección eficaz.

La figura 5.5 muestra la sección eficaz de arranque de un neutrón para núcleos de los diferentes elementos estudiados en este trabajo con un número de neutrones próximos a N=82. Se observa como la sección eficaz cae para los tres elementos en N=84. Además se puede ver como el resultado obtenido con el cálculo, representado en la figura 5.5 como una línea laminada, describe con gran precisión los valores medidos.

La sección eficaz de arranque de un protón se ha medido para 13 núcleos diferentes próximos al ^{132}Sn. El valor de las secciones eficaces de arranque de un protón es del orden de 10 veces mas pequeño que el valor obtenido para las secciones eficaces de arranque de un neutrón. Esto puede explicarse en parte dedido a la diferencia en el número de neutrones y protones y efectos derivados de la presencia de una piel de neutrones.

El comportamiento de las secciones eficaces en función del número de neutrones del proyectil es similar al de la seccion eficaz de arranque de neu-

trones. Por debajo de N=83, el valor obtenido es similar para los diferentes elementos estudiados. En N=83, se observa la caida en la sección eficaz debido a la presencia de la capa N=82. Además, los dos núcleos estudiados con N=83 (^{133}Sn y ^{134}Sb) presentan una diferencia entre ambos, teniendo una mayor sección eficaz el correspondiente al ^{133}Sn. Este efecto se debe a la presencia de la capa de protones Z=50. Sin embargo, esta diferencia no es observada para los núcleos con N<83.

La figura 5.6 muestra las secciones eficaces de arranque de un protón medidas en este trabajo. La línea continua muestra el resultado del cálculo realizado con el mismo modelo usado para describir el arranque de neutrones. Esta figura muestra como el cálculo sobreestima sistematicamente el valor de la sección eficaz de arranque de protones. La figura 5.6 también muestra el impacto que tienen en la sección eficaz las correlaciones de corto alcance entre nucleones. Este efecto reduce la sección eficaz calculada en un ∼30%, reduciendo la diferencia entre el valor calculado y el valor medido.

Los resultados obtenidos en este trabajo muestran que la sección eficaz medida de arranque de nucleones es susceptible a la presencia de correlaciones de corto alcance. De acuerdo con los resultados obtenidos en Ref.[12], la fracción relativa de neutrones y protones correlacionados dentro del núcleo depende de la asimetría de este, siendo la fracción mas alta aquella la de los nucleones que se encuentran en minoría (por ejemplo protones en núcleos ricos en neutrones). El estudio del efecto de las correlaciones tanto en la sección eficaz de arranque de neutrones como la de protones se muestra en la figura 5.7. Aquí se ve como el efecto en la sección eficaz de arranque de neutrones es menor, ya que la fracción de neutronees correlacionados apenas representa el ∼15% de nucleones. Sin embargo, el efecto en los protones, donde la fracción de protones correlacionados constituye el ∼30%, es más notable. Además, la figura 5.7 incluye un cálculo donde la fracción de protones correlacionados es independiente del isospin, manteniendo una fracción del ∼20% a lo largo de toda la cadena isotópica. Este resultado se muestra insuficiente para describir el arranque de protones en los isótopos de estaño con mayor asimetría, ilustrando que el impacto de las correlaciones de corto alcance en la sección eficaz de arranque de nucleones es dependiente del exceso de neutrones del núcleo.

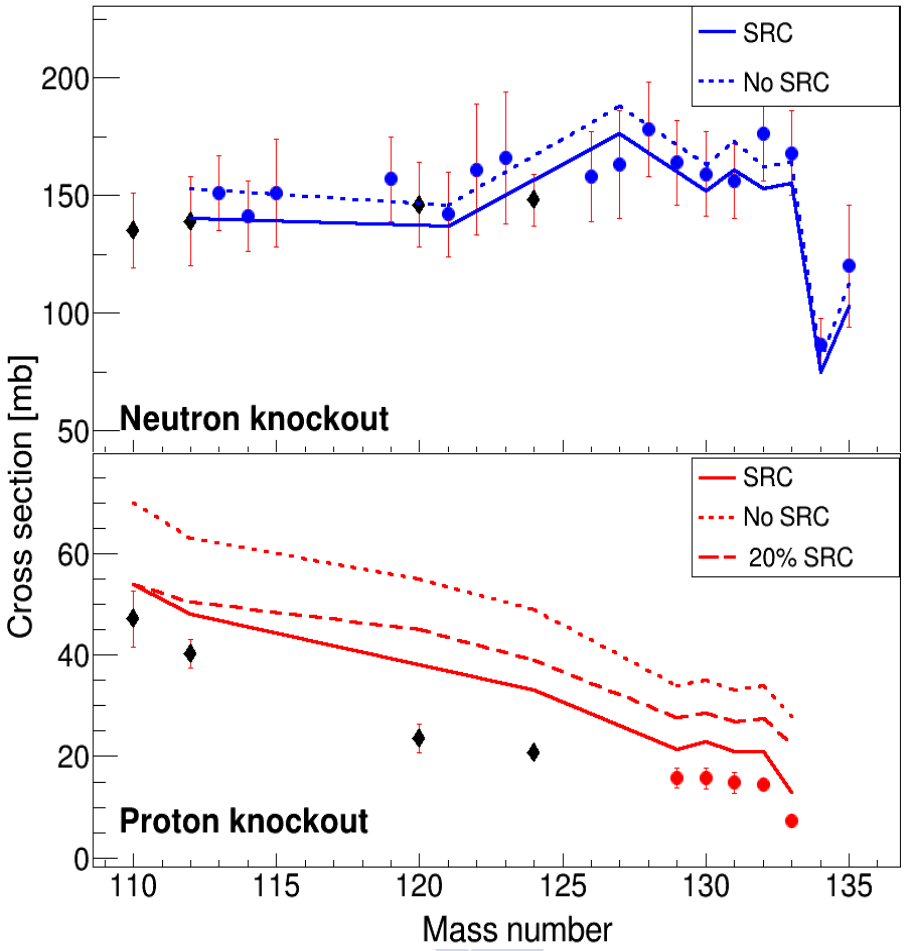

Figure 5.7: *Secciones eficaces de arraque de neutrones y protones para los núcleos de estaño investigados en este trabajo. El panel superior muestra la sección eficaz de arranque de neutrones, la línea punteada representa el cálculo sin correalaciones de corto alcance y la línea continua muestra el resultado del cálculo con correlaciones. El panel inferior muestra la sección eficaz de arranque de protones, la línea punteada muestra el resultado del cálculo sin correlaciones, la línea sólida muestra el resultado del cálculo con correlaciones y la linea laminada muestra el resultado del cálculo con una probabilidad de encontrar nucleones correlacionados independiente del isospin.*

Appendix A

Total Reaction cross sections

In this appendix we present all the total reaction cross section measured in this work with their asssociated uncertainity.

Z=48 Isotopes

Isotope	σ_R (mb)	$\Delta\sigma_R$	Δ_{Sim}	Δ_{Tgt}	Δ_{Tr}	Δ_{ToF}	Δ_{Dt}	$\Delta\sigma_R^{Tot}$
^{128}Cd	**2482**	89.47	49.64	86.87	124.1	24.82	24.82	**186.5 (7.5%)**
^{127}Cd	**2342**	55.64	46.84	81.97	117.1	23.42	23.42	**163.4 (6.9%)**
^{124}Cd	**2154**	116.1	43.08	75.39	107.7	21.54	21.54	**183.1 (8.5%)**
^{123}Cd	**2031**	55.42	40.63	71.09	101.5	20.31	20.31	**144.5 (7.1%)**
^{120}Cd	**1997**	120.3	39.94	69.89	99.85	19.97	19.97	**177.5 (8.9%)**
^{113}Cd	**1953**	92.10	39.06	68.33	97.65	19.53	22.53	**157.9 (8.1%)**

Z=49 Isotopes

Isotope	σ_R (mb)	$\Delta\sigma_R$	Δ_{Sim}	Δ_{Tgt}	Δ_{Tr}	Δ_{ToF}	Δ_{Dt}	$\Delta\sigma_R^{Tot}$
^{131}In	**2585**	30.56	51.70	90.47	129.3	25.85	25.85	**172.5 (6.7%)**
^{130}In	**2364**	40.19	47.28	82.74	118.2	23.64	23.64	**160.5 (6.8%)**
^{129}In	**2294**	70.27	45.88	80.29	114.1	22.94	22.94	**166.1 (7.2%)**
^{128}In	**2183**	139.6	43.66	76.40	109.6	21.83	21.83	**199.8 (9.1%)**
^{127}In	**2259**	92.11	45.18	79.06	112.8	22.59	22.59	**174.7 (7.7%)**
^{126}In	**1998**	49.86	39.96	69.93	99.90	19.98	19.98	**140.2 (7.1%)**
^{124}In	**2114**	130.0	42.28	73.99	105.7	21.14	21.14	**190.3 (9.0%)**
^{123}In	**2050**	65.33	41.00	71.75	102.5	20.50	20.50	**149.6 (7.3%)**
^{117}In	**1940**	128.8	38.80	67.90	97.00	19.40	19.40	**180.7 (9.3%)**
^{116}In	**2033**	77.14	40.66	71.15	101.6	20.33	20.33	**154.3 (7.5%)**

Table 1: *Measured total reaction cross sections for Z=48 and Z=49 isotopes.*

Z=50 Isotopes								
Isotope	σ_R (mb)	$\Delta\sigma_R$	Δ_{Sim}	Δ_{Tgt}	Δ_{Tr}	Δ_{ToF}	Δ_{Dt}	$\Delta\sigma_R^{Tot}$
^{135}Sn	**2564**	115.4	51.28	89.74	128.2	25.64	25.64	**204.1 (7.9%)**
^{134}Sn	**2398**	78.88	47.96	83.93	119.9	23.98	23.98	**176.3 (7.3%)**
^{133}Sn	**2342**	137.5	46.84	81.97	117.1	23.42	23.42	**205.1 (8.8%)**
^{132}Sn	**2363**	92.76	47.26	82.75	118.5	23.63	23.63	**180.5 (7.6%)**
^{131}Sn	**2286**	70.98	45.72	80.10	114.3	22.86	22.86	**166.1 (7.3%)**
^{130}Sn	**2212**	75.90	44.24	77.42	110.6	22.12	22.12	**163.7 (7.4%)**
^{129}Sn	**2109**	72.20	42.18	73.85	105.5	21.09	21.09	**156.3 (7.4%)**
^{128}Sn	**2101**	96.46	42.02	73.53	105.1	21.01	21.01	**168.3 (8.1%)**
^{126}Sn	**2062**	73.88	41.24	72.17	103.1	20.62	20.62	**154.0 (7.5%)**
^{125}Sn	**2145**	72.22	42.90	75.07	107.3	21.45	21.45	**158.4 (7.4%)**
^{123}Sn	**1968**	114.3	39.36	68.88	98.40	19.68	19.68	**172.5 (8.7%)**
^{120}Sn	**2067**	160.2	41.34	72.35	103.4	20.67	20.67	**209.1 (10%)**
^{119}Sn	**2110**	66.78	42.20	73.85	105.5	21.10	21.10	**153.5 (7.3%)**
^{118}Sn	**2039**	72.38	40.78	71.36	101.9	20.39	20.39	**152.1 (7.5%)**
^{113}Sn	**1887**	62.26	37.74	66.05	94.35	18.87	18.87	**138.6 (7.3%)**
Z=51 Isotopes								
Isotope	σ_R (mb)	$\Delta\sigma_R$	Δ_{Sim}	Δ_{Tgt}	Δ_{Tr}	Δ_{ToF}	Δ_{Dt}	$\Delta\sigma_R^{Tot}$
^{136}Sb	**2398**	66.08	47.96	83.93	119.9	23.98	23.98	**170.1 (7.1%)**
^{135}Sb	**2336**	52.13	46.72	81.76	116.8	23.36	23.36	**162.2 (6.9%)**
^{134}Sb	**2166**	20.76	43.32	75.81	108.3	21.66	21.66	**143.9 (6.6%)**
^{133}Sb	**2194**	52.44	43.88	76.79	109.7	21.94	21.94	**153.4 (6.9%)**
^{132}Sb	**2094**	43.36	41.88	73.29	104.7	20.94	20.94	**144.3 (6.9%)**
^{131}Sb	**2157**	59.65	43.14	75.49	107.8	21.12	21.12	**153.6 (7.1%)**
^{129}Sb	**2018**	46.41	40.36	70.63	100.9	20.18	20.19	**140.6 (6.9%)**
^{128}Sb	**1994**	13.19	39.88	69.79	99.80	19.94	19.94	**131.7 (6.6%)**
^{126}Sb	**1994**	74.47	39.88	69.79	99.80	19.94	19.94	**150.7 (7.5%)**
^{122}Sb	**1986**	51.91	39.72	69.51	99.31	19.86	19.86	**140.2 (7.1%)**
^{121}Sb	**1958**	67.40	39.16	68.53	97.90	19.58	19.58	**145.1 (7.4%)**

Table 2: *Measured total reaction cross sections for Z=50 and Z=51 isotopes.*

Z=52 Isotopes

Isotope	σ_R (mb)	$\Delta\sigma_R$	Δ_{Sim}	Δ_{Tgt}	Δ_{Tr}	Δ_{ToF}	Δ_{Dt}	$\Delta\sigma_R^{Tot}$
^{140}Te	**2847**	102.1	56.94	99.64	142.3	28.47	28.47	**213.2 (7.5%)**
^{139}Te	**2441**	99.81	48.82	85.43	122.1	24.41	24.41	**188.6 (7.7%)**
^{138}Te	**2370**	92.52	47.40	82.95	118.5	23.70	23.70	**180.9 (7.6%)**
^{137}Te	**2245**	123.1	44.90	78.57	112.2	22.45	22.45	**192.1 (8.5%)**
^{136}Te	**2106**	44.78	42.12	73.71	105.3	21.06	21.06	**145.2 (6.9%)**
^{135}Te	**2107**	44.43	42.14	73.74	105.3	21.07	21.07	**145.4 (6.9%)**
^{134}Te	**2053**	33.45	41.06	71.85	102.6	20.53	20.53	**138.9 (6.8%)**
^{130}Te	**2023**	36.19	40.46	70.85	101.1	20.23	20.23	**137.3 (6.8%)**
^{128}Te	**1957**	61.76	39.14	68.49	97.85	19.57	19.57	**133.7 (6.82%)**
^{124}Te	**2009**	27.86	40.18	70.31	100.4	20.09	20.09	**135.2 (6.7%)**
^{123}Te	**2092**	62.11	41.84	73.22	104.6	20.92	20.92	**150.92(7.2%)**

Table 3: *Measured total reaction cross sections for Z=52 isotopes.*

Appendix B

In this appendix we present all the one-neutron removal and one-proton removal cross section measured in this work with their asssociated uncertainity. We also present the values of the calculated transmission of each measured isotope.

Z=48 Isotopes

Isotope	σ_{1n} (mb)	$\Delta\sigma_{1n}^{stat}$	Δ_{Ch}	Δ_{Tr}	Δ_{Sr}	Δ_{Dt}	$\Delta\sigma_R^{Tot}$
^{126}Cd	**173**	20.8	1.73	17.3	1.73	1.73	**26.6 (15%)**
^{125}Cd	**168**	23.2	1.68	16.8	1.68	1.68	**27.9 (17%)**
^{124}Cd	**136**	4.20	1.36	13.6	1.36	1.36	**14.3 (10%)**
^{123}Cd	**150**	11.4	1.50	15.0	1.50	1.50	**18.7 (12%)**
^{122}Cd	**156**	34.4	1.56	15.6	1.56	1.56	**37.5 (24%)**
^{121}Cd	**163**	23.2	1.63	16.3	1.63	1.63	**28.3 (17%)**
^{120}Cd	**162**	39.1	1.62	16.2	1.62	1.62	**42.4 (26%)**
^{117}Cd	**137**	22.1	1.37	13.7	1.37	1.37	**26.0 (18%)**
^{116}Cd	**136**	11.3	1.36	13.6	1.36	1.36	**17.6 (12%)**
^{115}Cd	**130**	9.10	1.30	13.0	1.30	1.30	**15.9 (12%)**
^{114}Cd	**154**	23.9	1.54	15.4	1.54	1.54	**27.8 (18%)**
^{113}Cd	**151**	36.6	1.51	1 5.1	1.51	1.51	**39.1 (25%)**
^{110}Cd	**139**	17.0	1.39	13.9	1.39	1.39	**22.1 (15%)**
^{109}Cd	**153**	21.4	1.53	15.3	1.53	1.53	**26.1 (17%)**
^{108}Cd	**160**	23.2	1.60	16.0	1.60	1.60	**28.1 (17%)**
^{107}Cd	**130**	17.1	1.30	13.0	1.30	1.30	**21.5 (16%)**

Table 4: *Measured one-neutron removal cross sections for Z=48 isotopes.*

Z=49 Isotopes

Isotope	σ_{1n} (mb)	$\Delta\sigma_{1n}^{stat}$	Δ_{Ch}	Δ_{Tr}	Δ_{Sr}	Δ_{Dt}	$\Delta\sigma_R^{Tot}$
^{131}In	**140**	6.89	1.40	14.0	1.40	1.40	**15.8 (11%)**
^{130}In	**150**	8.14	1.50	15.0	1.50	1.50	**17.2 (11%)**
^{128}In	**126**	9.17	1.26	12.6	1.26	1.26	**15.6 (12%)**
^{127}In	**125**	7.43	1.25	12.5	1.25	1.25	**14.5 (12%)**
^{126}In	**157**	24.4	1.57	15.7	1.57	1.57	**28.8 (18%)**
^{124}In	**151**	20.2	1.51	15.1	1.51	1.51	**25.1 (16%)**
^{123}In	**171**	20.7	1.71	17.1	1.71	1.71	**26.5 (15%)**
^{118}In	**120**	10.1	1.20	12.0	1.20	1.20	**15.7 (13%)**
^{117}In	**151**	35.3	1.51	15.1	1.51	1.51	**38.3 (25%)**
^{116}In	**142**	20.1	1.42	14.2	1.42	1.42	**24.6 (17%)**
^{112}In	**137**	14.9	1.37	13.7	1.37	1.37	**19.8 (14%)**
^{111}In	**156**	42.1	1.56	15.6	1.56	1.56	**43.8 (28%)**
^{110}In	**146**	34.5	1.46	14.6	1.46	1.46	**37.1 (25%)**
^{109}In	**116**	12.4	1.16	12.4	1.16	1.16	**16.8 (14%)**

Table 5: *Measured one-neutron removal cross sections for Z=49 isotopes.*

Z=51 Isotopes

Isotope	σ_{1n} (mb)	$\Delta\sigma_{1n}^{stat}$	Δ_{Ch}	Δ_{Tr}	Δ_{Sr}	Δ_{Dt}	$\Delta\sigma_R^{Tot}$
^{137}Sb	**123**	16.4	1.23	12.3	1.23	1.23	**20.3 (16%)**
^{136}Sb	**128**	10.2	1.28	12.8	1.28	1.28	**16.2 (12%)**
^{135}Sb	**84.8**	5.27	0.84	8.48	0.84	0.84	**9.88 (11%)**
^{134}Sb	**162**	10.4	1.62	16.2	1.62	1.62	**19.2 (12%)**
^{133}Sb	**171**	6.47	1.71	17.1	1.71	1.71	**18.3 (11%)**
^{132}Sb	**181**	6.23	1.81	18.1	1.81	1.81	**19.3 (11%)**
^{131}Sb	**179**	7.73	1.79	17.9	1.70	1.70	**19.8 (11%)**
^{130}Sb	**179**	10.1	1.79	17.9	1.79	1.79	**20.7 (11%)**
^{129}Sb	**161**	14.3	1.61	16.1	1.61	1.61	**21.5 (13%)**
^{128}Sb	**183**	8.15	1.83	18.3	1.83	1.83	**20.0 (11%)**
^{123}Sb	**157**	9.93	1.57	15.7	1.57	1.57	**18.8 (12%)**
^{117}Sb	**138**	7.12	1.38	13.8	1.38	1.38	**15.6 (11%)**
^{116}Sb	**151**	5.17	1.51	15.1	1.51	1.51	**16.1 (11%)**
^{115}Sb	**173**	6.13	1.73	17.3	1.73	1.73	**18.5 (11%)**
^{114}Sb	**176**	5.10	1.76	17.6	1.76	1.76	**18.5 (11%)**

Table 6: *Measured one-neutron removal cross sections for Z=51 isotopes.*

Z=50 Isotopes

Isotope	σ_{1n} (mb)	$\Delta\sigma_{1n}^{stat}$	Δ_{Ch}	Δ_{Tr}	Δ_{Sr}	Δ_{Dt}	$\Delta\sigma_R^{Tot}$
^{135}Sn	**120**	24.0	1.20	12.0	1.20	1.20	**26.3 (22%)**
^{134}Sn	**86.5**	7.92	0.86	8.65	0.86	0.86	**11.2 (13%)**
^{133}Sn	**168**	6.54	1.68	16.8	1.68	1.68	**18.7 (11%)**
^{132}Sn	**176**	8.95	1.76	17.6	1.76	1.76	**20.0 (11%)**
^{131}Sn	**156**	5.23	1.56	15.6	1.56	1.56	**16.6 (11%)**
^{130}Sn	**159**	7.58	1.59	15.9	1.59	1.59	**18.1 (11%)**
^{129}Sn	**164**	8.42	1.64	16.4	1.64	1.64	**18.4 (11%)**
^{128}Sn	**178**	10.1	1.78	17.8	1.78	1.78	**20.6 (12%)**
^{127}Sn	**163**	16.6	1.63	16.3	1.63	1.63	**23.1 (14%)**
^{126}Sn	**158**	11.8	1.58	15.8	1.58	1.58	**19.5 (12%)**
^{123}Sn	**166**	23.2	1.66	16.6	1.66	1.66	**28.1 (17%)**
^{122}Sn	**161**	23.6	1.61	16.1	1.61	1.61	**28.2 (17%)**
^{121}Sn	**142**	11.5	1.42	14.2	1.42	1.42	**18.2 (13%)**
^{119}Sn	**157**	8.12	1.57	15.7	1.57	1.57	**18.2 (12%)**
^{115}Sn	**151**	18.2	1.51	15.1	1.51	1.51	**23.6 (15%)**
^{114}Sn	**141**	7.46	1.41	14.1	1.41	1.41	**15.9 (11%)**
^{113}Sn	**151**	5.76	1.51	15.1	1.51	1.51	**16.1 (11%)**

Table 7: *Measured one-neutron removal cross sections for Z=50 isotopes.*

Z=52 Isotopes

Isotope	σ_{1n} (mb)	$\Delta\sigma_{1n}^{stat}$	Δ_{Ch}	Δ_{Tr}	Δ_{Sr}	Δ_{Dt}	$\Delta\sigma_R^{Tot}$
^{139}Te	**177**	20.4	1.77	17.7	1.77	1.73	**26.7 (15%)**
^{138}Te	**145**	13.2	1.45	14.5	1.45	1.45	**19.6 (13%)**
^{137}Te	**144**	10.2	1.44	14.4	1.44	1.44	**17.7 (12%)**
^{136}Te	**105**	5.43	1.05	10.5	1.05	1.05	**11.7 (11%)**
^{135}Te	**171**	7.44	1.71	17.1	1.71	1.71	**17.8 (11%)**
^{134}Te	**191**	7.21	1.91	19.1	1.91	1.91	**20.6 (11%)**
^{130}Te	**155**	7.80	1.55	15.5	1.55	1.55	**17.7 (11%)**
^{128}Te	**178**	11.1	1.78	17.8	1.78	1.78	**21.5 (12%)**
^{126}Te	**174**	14.3	1.74	17.4	1.74	1.74	**22.9 (12%)**
^{125}Te	**194**	18.1	1.94	19.4	1.94	1.94	**26.7 (14%)**

Table 8: *Measured one-neutron removal cross sections for Z=52 isotopes.*

Isotope	Transmission	Isotope	Transmission	Isotope	Transmission
^{131}In	0.90	^{132}Sn	0.80	^{133}Sb	0.60
^{130}In	0.91	^{131}Sn	0.83	^{132}Sb	0.52
^{129}In	0.89	^{130}Sn	0.86	^{131}Sb	0.57
^{128}In	0.90	^{129}Sn	0.82		
^{133}Sn	080	^{134}Sb	0.60		

Table 9: *Calculated transmission for all of the Z-1 fragment produced via proton knockout in this work.*

Isotope	Transmission	Isotope	Transmission	Isotope	Transmission
^{126}Cd	0.86	^{116}In	0.99	^{135}Sb	0.67
^{125}Cd	0.93	^{112}In	0.99	^{134}Sb	0.73
^{124}Cd	0.88	^{111}In	0.99	^{133}Sb	0.74
^{123}Cd	0.87	^{110}In	0.99	^{132}Sb	0.61
^{122}Cd	0.85	^{109}In	0.90	^{131}Sb	0.66
^{121}Cd	0.88	^{135}Sn	0.78	^{130}Sb	0.60
^{120}Cd	0.99	^{134}Sn	0.82	^{129}Sb	0.90
^{117}Cd	0.99	^{133}Sn	0.93	^{128}Sb	0.75
^{116}Cd	0.99	^{132}Sn	0.88	^{123}Sb	0.80
^{115}Cd	0.99	^{131}Sn	0.87	^{117}Sb	0.95
^{114}Cd	0.99	^{130}Sn	0.82	^{116}Sb	0.90
^{110}Cd	0.99	^{129}Sn	0.86	^{115}Sb	0.80
^{109}Cd	0.99	^{128}Sn	0.82	^{114}Sb	0.95
^{108}Cd	0.99	^{127}Sn	0.80	^{139}Te	0.51
^{107}Cd	0.99	^{126}Sn	0.96	^{138}Te	0.48
^{131}In	0.95	^{123}Sn	0.95	^{137}Te	0.60
^{130}In	0.90	^{122}Sn	0.99	^{136}Te	0.48
^{128}In	0.97	^{121}Sn	0.94	^{135}Te	0.51
^{127}In	0.97	^{119}Sn	0.95	^{134}Te	0.43
^{126}In	0.95	^{115}Sn	0.97	^{130}Te	0.30
^{124}In	0.98	^{114}Sn	0.94	^{128}Te	0.40
^{123}In	0.94	^{113}Sn	0.93	^{126}Te	0.49
^{118}In	0.99	^{137}Sb	0.70	^{125}Te	0.30
^{117}In	0.99	^{136}Sb	0.65	^{119}Te	0.60

Table 10: *Calculated transmission from the intermediate to the final focal planes for all of the neutron-less fragments produced via neutron knockout in this work*

Appendix C

Layer	Mat	Thickness (mg/cm^2)	Layer	Mat	Thickness (mg/cm^2)
SIS window	Ti	4.5	MUSIC windows	Al	1.23
SEETRAM C	Ti	13.5	MUSIC windows	Si	39.76
Target	Pb	649	MUSIC windows	K	0.35
Target	Pb	1534	MUSIC gas	C	22.52
Target	Be	1036	MUSIC gas	F	142.38
Protection	Al	8.64	MUSIC mylar	C	4.35
Scintillator	C	471.9	MUSIC mylar	H	0.29
Scintillator	H	44.01	MUSIC mylar	O	2.32
Protection	AL	8.64	Air gap	N	45.98
Vac. window	Fe	78.66	Air gap	O	14.09
Air gap	N	18.21	Air gap	Ar	0.774
Air gap	O	5.58	TPC2 windows	C	2.59
Air gap	Ar	0.31	TPC2 windows	H	0.10
TPC1 windows	C	2.59	TPC2 windows	N	0.27
TPC1 windows	H	0.10	TP2C windows	O	0.78
TPC1 windows	N	0.27	Air gap	N	20.03
TPC1 windows	O	0.78	Air gap	O	6.14
TPC1 gas	Ar	18.29	Air gap	Ar	0.34
Air gap	N	15.48	Secondary target	Be	2591
Air gap	O	4.74	Air gap	N	18.21
Air gap	Ar	0.26	Air gap	O	5.58
MUSIC windows	B	4.22	Air gap	Ar	0.31
MUSIC windows	O	56.87	TPC3 windows	C	2.59
MUSIC windows	Na	2.97	TPC3 windows	H	0.19

Table 11: *Layers of matter in the beamline.*

Layer	Mat	Thickness (mg/cm^2)	Layer	Mat	Thickness (mg/cm^2)
TPC3 windows	N	0.27	Air gap	O	7.12
TPC3 windows	O	0.78	Air gap	Ar	0.39
TPC3 gas	Ar	18.29	MUSIC windows	B	4.22
Air gap	N	76.48	MUSIC windows	O	56.87
Air gap	O	23.44	MUSIC windows	Na	2.97
Air gap	Ar	1.29	MUSIC windows	Al	1.23
TPC4 windows	C	2.59	MUSIC windows	Si	39.76
TPC4 windows	H	0.19	MUSIC windows	K	0.35
TPC4 windows	N	0.27	MUSIC gas	C	22.52
TPC4 windows	O	0.78	MUSIC gas	F	142.38
TPC4 gas	Ar	18.29	MUSIC mylar	C	4.35
Air gap	N	23.22	MUSIC mylar	H	0.29
Air gap	O	7.12	MUSIC mylar	O	2.32
Air gap	Ar	0.39	Air gap	N	25.04
Scintillator	C	370.4	Air gap	O	7.68
Scintillator	H	34.54	Air gap	Ar	0.4
Air gap	N	11.38	TPC6 windows	C	2.59
Air gap	O	3.49	TPC6 windows	H	0.19
Air gap	Ar	0.19	TPC6 windows	N	0.27
Vac. window	Fe	90.0	TPC6 windows	O	0.78
Air gap	N	16.84	TPC6 gas	Ar	18.29
Air gap	O	5.16	Air gap	N	60.55
Air gap	Ar	0.28	Air gap	O	18.56
TPC5 windows	C	2.59	Air gap	O	1.02
TPC5 windows	H	0.19	Scintillator	C	370.4
TPC5 windows	N	0.27	Scintillator	H	34.54
TPC5 windows	O	0.78			
TPC5 gas	Ar	18.29			
Air gap	N	23.22			

Table 12: *Layers of matter in the beamline.*

Bibliography

[1] I. Tanihata et al,. *Phys. Lett. B*, 287:307–311, 1992.

[2] D. Bazin et al,. *Phys. Lett. B*, 74:3569–3572, 1992.

[3] I. Tanihata et al,. *Phys. Lett. B*, 289:261–266, 1992.

[4] L. Lapikas. *Nucl. Phys. A*, 553:297–308, 1993.

[5] J.A. Tostevin. *Phys. Rev. C*, 90:057602, 2014.

[6] L. Atar et al. *Phys. Rev. Lett*, 120:052501, 2018.

[7] J. Lee et al. *Phys. Rev. Lett*, 104:112701, 2010.

[8] F. Flavigny et al. *Phys. Rev. Lett*, 110:122503, 2013.

[9] B. P. Kay et al. *Phys. Rev. Lett*, 111:042502, 2013.

[10] The CLAS Collaboration . *Science*, 346, 2014.

[11] L. Frankfurt et al . *Int J. Mod. Phys. A*, 23:2991–3054, 2008.

[12] The CLAS Collaboration . *Nature*, 560, 2018.

[13] G. Jacob and Th. A. J. Maris. *Rev. Mod. Phys*, 45:6–21, 1973.

[14] T. J. M. Symons et al,. *Phys. Rev. Lett*, 42:40–43, 1979.

[15] G. D. Westfall et al,. *Phys. Rev. Lett*, 43, 1979.

[16] J. Speth and A. van der Woude. *Rep. Prog. Phys*, 44, 1981.

[17] A. Shevchenko et al. *Phys. Rev. C*, 79:044305, 2009.

[18] J. Al-Khalili and Filomena Nunes. *J. Phys G*, 29, 2003.

[19] J. A. Tostevin. *Nucl. Phys. A*, 682:320–331, 2001.

[20] R. J. Glauber and G. Matthiae. *Nucl. Phys. B*, 21:135–157, 1970.

[21] Paul J. Karol,. *Phys. Rev. C*, 11:1203–1209, 1975.

[22] B. A. Brown and B. H. Wildenthal. *Annu. Rev. Nucl. Part. Sci*, 38, 1988.

[23] J. Cugnon, C. Volant and S. Vullieir. *Nucl. Phys. A*, 620:457–509, 1997.

[24] N. A. Orr et al. *Phys. Rev. Lett*, 69:2050–2053, 1992.

[25] E. Sauvan et al. *Phys. Lett. B*, 491:1–7, 2000.

[26] E. Sauvan et al. *Phys. Rev. C*, 69:044603, 2004.

[27] A. Navin et al. *Phys. Rev. Lett*, 81:5089–5092, 1998.

[28] D. Cortina-Gil et al. *Eur. Phys. J. A*, 10, 2001.

[29] A. Navin et al,. *Phys. Rev. Lett*, 85:266–269, 2000.

[30] D. Cortina-Gil et al. *Phys. Rev. Lett*, 93:062501, 2004.

[31] A. Gade et al. *Phys. Rev. Lett*, 93:042501, 2004.

[32] J.L. Rodríguez-Sánchez et al. *Phys. Rev. C*, 96:034303, 2017.

[33] T. Brohm and K. H. Schmidt. *Nucl. Phys. A*, 569:821–832, 1994.

[34] D. Loureiro et al . *Phys. Lett. B*, 703:552–556, 2011.

[35] L. Audirac et al. *Phys. Rev. C*, 88:041602, 2013.

[36] K. H. Schmidt et al. *Phys. Lett. B*, 300:313–316, 1993.

[37] A.Boudard et al. *Phys. Rev. C*, 66:044615, 2002.

[38] C. Louchart et al. *Phys. Rev. C*, 83:011601, 2011.

[39] Or. Hen et al. *Rev. Mod. Phys*, 89, 2017.

[40] K. S. Egiyan et al. *Phys. Rev. Lett*, 96:082501, 2006.

[41] E. Piasetzky et al. *Phys. Rev. Lett*, 97(162504), 2006.

[42] V.Hlinka et al. *Nucl. Instr. Meth. A*, 419:503–510, 1998.

[43] G. Charpak and F. Sauli. *Nuclear instruments and methods*, 162:405–428, 1979.

[44] A. Ozawa et al. *Nucl. Phys. A*, 693:32–62, 2001.

[45] I. Tanihata et al. *Phys. Rev. Lett*, 55:2676–2679, 1985.

[46] I. Tanihata et al. *Phys. Lett*, 160:380–384, 1985.

[47] W. Mittig et al. *Phys. Rev. Lett*, 59:1889–1891, 1987.

[48] T.Suzuki et al. *Phys. Rev. Lett*, 75:3241–3244, 1995.

[49] T.Suzuki et al. *Nucl. Phys. A*, 630, 1998.

[50] B. Blank et al. *Nucl. Phys. A*, 624, 1997.

[51] F. Negoita et al. *Phys. Rev. C*, 54:1787–1797, 1996.

[52] R.E. Warner et al. *Nucl. Phys. A*, 635:292–304, 1998.

[53] M. Fukuda et al. *Nucl. Phys. A*, 656, 1999.

[54] H.Y. Zhang et al. *Nucl. Phys. A*, 707:303–324, 2002.

[55] R.E. Warner et al. *Phys. Rev. C*, 64:044611, 2001.

[56] H.Y. Zhang et al. *Nucl. Phys. A*, 707, 2002.

[57] A. Ozawa et al. *Nucl. Phys. A*, 709:60–72, 2002.

[58] R. Kanungo et al. *Phys. Rev. C*, 84:061304, 2011.

[59] R. Kanungo et al. *Phys. Rev. C*, 83:021302, 2011.

[60] P.U. Renberg et al. *Nucl. Phys. A*, 183:81–104, 1972.

[61] J. Benlliure et al. *NIM. A*, 2001.

[62] C. Scheidenberger et al. *Nucl. Instr. and Meth. B*, 142:441–602, 1998.

[63] N. Iwasa et al. *Nucl. Instr and Meth. B*, 126:284–289, 1997.

[64] Dusan Dragosavac. Accurate calculation of the optical transmission of high resolving spectrometer. 142, 2009.

[65] D. Bazin and B. Sherrill. *Phys. Rev. E*, 50:4017–4021, 1994.

[66] L. Ray et al. *Phys. Rev. C*, 18, 1978.

[67] A. Krasznahorkay et al. *Nucl. Phys. A*, 731:224–324, 2004.

[68] A. Krasznahorkay et al. *Phys. Rev. Let*, 82:3216–3219, 1999.

[69] W. Horiuchi et al. *Phys. Rev. C*, 93:04611, 2016.

[70] W. Horiuchi et al. *Phys. Rev. C*, 86, 2012.

[71] T. Brohm and K. -H. Schmidt. *Nucl. Phys. A*, 659:821–832, 1994.

[72] Satoru Terashima,. Systematic study of neutron density distributions of sn isotopes by proton elastic scattering. *Doctoral Dissertation*, 2009.

[73] I. Angeli and K.P. Marinova. *Atomic Data and Nuclear Data Tables*, 99, 2013.

[74] Ingo Sick. *Phys. Lett. B*, 576:62–67, 2003.

[75] S. Kopecky et al. *Phys. Rev. C*, 56:2229–2237, 1997.

[76] C. A. Bertulani and C. de Conti. *Phys. Rev. C*, 81:064603, 2010.

[77] R. Schmidt et al. *Phys. Rev. Lett*, 70:1767, 1993.

[78] J. C. Hill et al. *Phys. Lett. B*, 273:371–374, 1991.

[79] P. Adrich et al. *Phys. Lett. B*, 95:132501, 2005.

[80] K. -H. Schmidt et al. *Nucl. Phys. A*, 665, 2000.

[81] C. A. Bertulani, C. M. Campbell and T. Glasmacher. *Computer Physics Communications*, 152:317–340, 2003.

[82] Andrea Horvat (TU Darmstadt). *Private Communications.*

[83] W. Horiuchi, T. Inakura, T. Nalatsukasa and Y. Suzuki. *Phys. Rev. C*, 86:024614, 2012.

[84] T. Nagahisha and W. Horiuchi. *Phys. Rev. C*, 97:054614, 2018.

[85] V. Vaquero et al. *Phys. Rev. Lett*, 118:202502, 2017.

[86] Davide Mancusi et al. *Phys. Rev. C*, 91:034602, 2015.

[87] J. Alcrántara-Núñez. *Phys. Rev. C*, 92:024607, 2015.

[88] G. Cerizza et al. *Phys. Rev. C*, 93:021601, 2016.

[89] T. Faestermann, M. Gorska and H. Grawe. *Prog. Part and Nucl. Phys*, 69:85–130, 2013.

[90] David Perez Loureiro. Investigating the production of medium-mass neutron-rich nuclei. *Doctoral Dissertation, University of Santiago de Compostela*, 2010.

[91] J.L. Rodríguez-Sánchez et al. *Phys. Rev. C*, 96:054602, 2017.

[92] A. Kelic, M. V. Ricciardi and K. H. Schmidt. *Proceedings of Joint ICTP-IAEA Advanced Workshop on Model Codes for Spallation Reactions*, 2008.

[93] A. R. Junghans et al. *Nucl. Phys. A*, 629:635–655, 1998.

[94] M. V. Ricciardi et al. *Phys. Rev. C*, 73:014607, 2006.

[95] C. Villagrasa-Canton et al. *Phys. Rev. C*, 75:044603, 2007.

[96] J. Benlliure et al. *Phys. Rev. C*, 74:014609, 2006.

[97] A.E.S. Green, T. Sawada, and D.S. Sacon. The nuclear independent particle model. the shell and optical models. 1 1968.

[98] L.Coraggio et al. *Phys. Rev. C*, 65:051306, 2002.

[99] G.A. Leander et al. *Phys. Rev. C*, 30:416–419, 1984.

[100] B. Fogelberg et al. *Phys. Rev. C*, 70:034312, 2004.

[101] J. Taprogge et al. *Phys. Rev. Lett*, 112:132501, 2014.

[102] K. Bennaceur and J. Dobaczewski. *Comp. Phys. Com*, 96:054602, 2017.

[103] L.Coraggio, A. Covello, A. Gargano and N. Itaco. *Phys. Rev. C*, 88:041304, 2013.

[104] M. Anikina et al. *Phys. Rev. C*, 33:895–909, 1986.

[105] M. Anikina et al. *Phys. Rev. Lett*, 50:1971–1974, 1983.

[106] Th. Aoust and Joseph Cugnon. *Phys. Rev. C*, 74:064607, 2006.

[107] Sophie Pedoux and Joseph Cugnon. *Nucl. Phys. A*, 866:16–36, 2011.

[108] K. L. Jones et al. *Nature Letters*, 465:454–457, 2010.

[109] N. V. Genezdilov, E. E. Saperstein and S. V. Tolokonnikov. *Physics of Atomic Nuclei*, 78:424–34, 2015.

[110] L.Coraggio ,A. Gargano and N. Itaco. *Phys. Rev. C*, 93:064328, 2016.

[111] A. Gargano, L.Coraggio and N. Itaco. *Phys. Scr*, 92:0694003, 2017.

[112] L.Coraggio, A. Gargano and N. Itaco. *Phys. Rev. C*, 93:064328, 2015.

[113] A. Gargano. *Private communication.*